

TRIBOLOGICAL BEHAVIOUR OF TRANSPARENT CERAMICS: A REVIEW

Divyansh Mittal^a, Jan Hostaša^b, Laura Silvestroni^b, Laura Esposito^b, Rajiv Kumar^a, Sandan Kumar Sharma^{a1}

^aDepartment of Metallurgical and Materials Engineering, Punjab Engineering College (Deemed to be University), Chandigarh, India

^bInstitute of Science and Technology for Ceramics, National Research Council (CNR ISTECC), Via Granarolo 64, Faenza, Italy

Abstract

Owing to superior properties, i.e. high hardness, high wear resistance, and weight reduction of transparent ceramics (TCs) over glasses, TCs have shown promising tribological potential for applications such as face shields, explosive ordnance visors, aircraft, spacecraft, re-entry vehicles, electromagnetic windows, laser igniter windows, screens for smartphones and more. Researchers globally have been attracted to explore more about TCs, considering the tremendously increasing demand over different other transparent materials. The optical quality of TCs is mostly characterized by the in-line transmittance, and the effect of various processing parameters on transmittance has already been studied by various researchers. In this review, the current research progress regarding also tribological properties of TCs is compiled. TCs with potential in tribological applications include MgAl₂O₄, Al₂O₃, AlON, Lu₂O₃, c-BN, Y₂O₃, Si₃N₄, and SiAlON. The relevant strategies to improve the tribological properties, including microstructures and mechanical properties are comprehensively discussed. In addition, the mechanisms of material removal of different transparent ceramics are also presented. It is well observed that surface fracture comprising 3 stages is found as one of the dominant wear mechanisms during wear. This review aims to provide some meaningful guidelines for development of transparent ceramics with enhanced wear resistance, while identifying the wear mechanisms in particular wear conditions.

Keywords: transparent; ceramics; tribology; wear mechanism; microstructure

¹Corresponding author, Tel: +91-9027186120; E-mail: sandansharma07@gmail.com

1. Introduction

Transparent ceramics (TCs) have been widely used materials in various applications during the last few decades. The first step toward the development of transparent ceramic dates back to Coble's invention of translucent alumina in 1959 [1] for the production of ceramic discharge tubes. It eventually resulted in the widespread use of high-pressure sodium vapor lamps for street lighting and a variety of other applications. Consequently, translucent and transparent ceramics became a key study area for different potential applications. In the 1970s, a viability study for transparent MgAl_2O_4 manufacturing was commenced [2], and in 1978 it was used for transparent armor [3]. In 1995, Ikesue et al. [4] demonstrated the first effective laser oscillation using a ceramic material (Nd: YAG), indicating that ceramics may be utilized for laser applications [5] with an efficiency equivalent to single crystal lasers [6]. Between the 2000s and 2010s, interest in transparent ceramics increased steadily. As a result, transparent ceramics research is well established in fields such as armor, impact-resistant windows, and missile domes [7–14], scintillators [15], phosphors [16,17], optical lenses [9], 3D displays [18], laser gain media [19,20], and other optical applications [7–14].

To explore the universe, studying the light or electromagnetic radiations of all the wavelengths emitted by different objects in space is necessary [21]. Various observatories and re-entry vehicles are sent to the atmosphere to get valuable information about the space. These observatories use many transparent materials for different purposes. Window materials for such spacecraft must satisfy a set of strict requirements to bear the thermal shock, uphold cabin pressure, resist aerodynamic heating, and tolerate high-velocity impact by foreign particles. TCs exhibit an outstanding ballistic performance compared to glass and are therefore being investigated by NASA for such application [22].

From the theoretical point of view, Krell et al. [23] provided an in-depth discussion of transparent ceramics and the mechanisms allowing or limiting the transparency of polycrystalline ceramic materials and the relationship with the microstructure. In extension, Wang et al. [9] and Xiao et al. [24] gave comprehensive and detailed studies of various types of transparent ceramics, their manufacturing, and their use. Transparent ceramics have the potential to meet all these requirements and superior optical characteristics [25].

In 2016, the TC market was valued at USD 219.2 Million, and presently it is expected to reach USD 698.1 Million by 2022 (at a compound annual growth rate of 21.3% from 2017 to 2022) [26]. In 2017, Salem (Material Engineer at NASA, GRC) conveyed that transparent

ceramics such as spinel and AlON exhibit better fracture toughness and crack growth resistance characteristics than glasses like fused silica [22]. Fused silica-based transparent materials have good optical characteristics and thermal shock resistance. Fused silica-based window materials have performed well in the space shuttle orbiter and the international space station (ISS) [22], but may exhibit a catastrophic failure due to the formation of thermal gradients in the material [27]. Nevertheless, TCs provide good optical characteristics and thermal shock resistance properties in addition to slow crack growth and high hardness, which extended their use in even more severe conditions [22]. TCs additionally provide a weight reduction of the vehicle, as the total thickness of the windows can be significantly reduced. These superior properties, i.e., slow crack growth, high hardness, high fracture toughness and weight reduction, of TCs over glasses provided potential in window systems and impacted the TC market [28–30]. Many tribological applications like personnel protection, face shields, riot visor, explosive ordnance visor, armor, ground vehicles, aircraft, spacecraft, re-entry vehicles, electromagnetic windows, laser igniter windows, artillery projectiles, and more can exploit the high performance of TCs due to these tunable properties [24,31].

The transparency and tribological behavior of TCs are influenced by different factors, which are collected in **Table 1**. The transparency of the TCs depends on the scattering of light, which can scatter in correspondence of residual pores, secondary phases, impurity inclusions, and grain boundaries [32–34]. The factors which affect the wear behavior of TC are mostly grain size, grain boundaries, crystal structure, residual pores, inclusions, and surface roughness [10,24,31,35–40]. It is also revealed that a high level of hardness and fracture toughness strongly influence the wear resistance of TC as they reduce the initial scratches as well as the subsequent fracture and propagation of cracks after initiation [41,42]. High fracture toughness and hardness value promise for the long-term protection of transparent ceramics. The presence of multiple phases leads to a decrease in transparency due to scattering.

Table 1: Effect of different factors on transparency and tribological behavior

Factor	Sub-Factor	Impact
Microstructure	Crystal Structure	<ul style="list-style-type: none"> • An isotropic crystal structure is mostly required for the manufacture of TC, as in an anisotropic crystals scattering occurs at grain boundaries [43] • A cubic crystal structure is ideal the highest transparency [7,43,44] • Defects in the crystal structure, like vacancies, increase the scattering thus decreasing the transparency [32–34]
	Phase	<ul style="list-style-type: none"> • The phase of the sintered TC must provide high density to the material with increased hardness and fracture toughness for better wear resistance [44] • A single-phase material is required for high transparency. The presence of multiple phases with different refractive index causes scattering of light [45,46]. A second phase may affect both the transparency and the tribological behavior of the material [27,47]

	Grain Boundary	<ul style="list-style-type: none"> • A uniform refractive index is required for high transmittance of TC as the non-uniform refractive index will show more scattering of light [45,46] • second phases at the grain boundary will increase the scattering of light [48] • Toughening mechanism and strengthening mechanisms, such as grain bridging, may increase the fracture toughness of the TC, which will increase the wear behavior of the material [35,49–51]
	Grain Size	<ul style="list-style-type: none"> • For most TCs the grain size does not affect transparency, but the full densification is often accompanied by grain growth, while fine grain size improve the tribological characteristics of TC [39,40,52,53] • Fine-grain size increase the hardness [35,54], and may have an effect also on the fracture toughness [35,44,54] • Spark plasma sintering (SPS) can be used to control the grain growth of TC while sintering [55,56]
	Porosity	<ul style="list-style-type: none"> • Inter-grain pores located at grain boundaries are easier to remove, but intra-grain pores are not always removed, which causes low transparency of TC [54] • Porosity has a direct relation with opacity and inverse relation with transparency, as pores have a strong effect on the scattering of light due to the high difference in refractive index compared to that of ceramics [26] • Reduction in porosity and increase in density is required to increase the wear resistance of the TC [35–38]
Process	Raw material	<ul style="list-style-type: none"> • A fine size of the raw material will lead to low porosity and improved sintering [57] • Optimum powder size is required to manufacture TC, as too fine raw material may lead to low density and easy agglomeration [58,59] • Highly dispersed powder ensure high sintering ability required for enhanced wear resistance of TC • Impurities in the material will generate dissimilar phases and form light scattering centers, which will reduce the transparency of the material [24].
	Doping	<ul style="list-style-type: none"> • Doping techniques affect the mechanical and tribological behavior of the material [60] • The addition of the correct amount of doping agent may increase the wear resistance of the TC with the improved mechanical properties [61,62]. On the other hand, the presence of a dopant should not lead to the formation of a second phase, which would compromise the transparency.
	Sintering	<ul style="list-style-type: none"> • Pressureless sintering in air and inert gas will lead to high porosity; therefore, vacuum sintering or hydrogen atmosphere is required [61,62] • Pressure-assisted methods (SPS and HIP) can achieve exceptional mechanical properties with improved tribological properties [63–65] by limiting grain growth while providing efficient densification. Compared to pressureless sintering, the sintering temperatures are usually lower and times shorter, in particular for SPS [55,56] • The use of sintering additives facilitates the removal of pores, reduces the sintering temperature and often limits grain growth, which in turn increases the hardness of the TC [36].
	Surface finish	<ul style="list-style-type: none"> • The final transparency of a TC depends on the optical quality of the surface, i.e. on the surface finish of the sintered sample: the greater the roughness of sintered ceramics, the lower is its transparency [28]. The mechanical performance is also affected by the presence of scratches or defect on the surface.

The optical appearance of transparent ceramics is comparable to that of glasses [13,14,66–71]; however, TCs exhibits higher hardness, higher fracture toughness, higher resilience, and minor mass loss in scratch wear test than glasses [66,72]. The comparison of hardness and fracture toughness of TCs with glass materials is shown in **Figure 1** [66]. Improving the material's hardness and fracture toughness enhance the TC's tribological performance [41,42,66,73], particularly a high hardness and low mass loss of TCs during the scratch wear test are beneficial to wear resistance of TCs [38,65,66]

TCs are highly transparent in the visible and mid-IR ranges (0.25–5.5 μm), which suggests the utilization of TCs as windows and domes in electro-optical and infrared sensors in military

systems [74]. Promising recent transparent materials used for military systems are MgAl₂O₄ [35], Al₂O₃ [75,76], AlON [77], Lu₂O₃[78,79], c-BN [80], Y₂O₃ [81,82], SiC [27], Si₃N₄ [65,83], and SiAlON [84–86] because of their high strength, hardness, and fracture toughness. Different mechanical, thermal, and optical properties of these transparent ceramics are listed in **Table 2**. These TCs have the potential to perform as good wear-resistant materials for different tribological applications. The study of tribological behaviour of transparent ceramics, such as MgAl₂O₄ [54,66], AlON [27,59,87–89], and Si₃N₄ [36,90,91] shows that these TCs exhibit significantly improved tribological performance compared to single crystals and glasses.

Table 2: Physical properties of transparent ceramics with potential in tribological applications.[27,37,59,63,65,75,83,86,92–112]

Properties of some transparent ceramic materials	MgAl ₂ O ₄	Al ₂ O ₃	AlON	Lu ₂ O ₃	c-BN	Y ₂ O ₃	Si ₃ N ₄
Hardness [GPa]	12-18	14-27	15-20	12-15	28-46	7-10	14-34
Fracture Toughness [MPa m ^{0.5}]	1.48-3.5	1.5-3.3	1.7-3	3.9-4.3	0.48-1.2	1.1-1.5	3.2-4.1
Transverse Rupture Strength [MPa]	80-250	450-850	330-370	-	230-370	130-170	414-682
Melting Temperature [°C]	~2140	~2277	~2150	~2500	~5689	~2410	~1900
Theoretical density [g/cm ³]	3.578	3.987	3.69	9.42	3.45	5.04	3.28
Thermal Conductivity [W/mK]	10-15	12-38	9-10	10-12.5	1.2-1.4	8-12	14.5-26
Young Modulus [GPa]	250-310	390-410	320-340	52-182	560-910	165-196	260-295
Shear Modulus [GPa]	120-140	84-92	125-138	21-71	360-370	63-71	105-110
Thermal Expansion Coefficient [K ⁻¹] x10 ⁻⁶	6-8	4.5-11	5-7	7.1-8.3	4.6-4.8	3.5-5	3-4
Refractive Index	1.715	1.78	1.79	2.12	2.117	1.93	2.02
Theoretical Transmission [%] (wavelength range, μm)	49-87 (0.2-5.5)	69-84 (0.2-5)	60-81 (0.4-5.2)	63-77 (0.8-2.3)	59-69 (0.3-1.5)	70-83 (0.3-7)	38-46 (0.8-2.5)

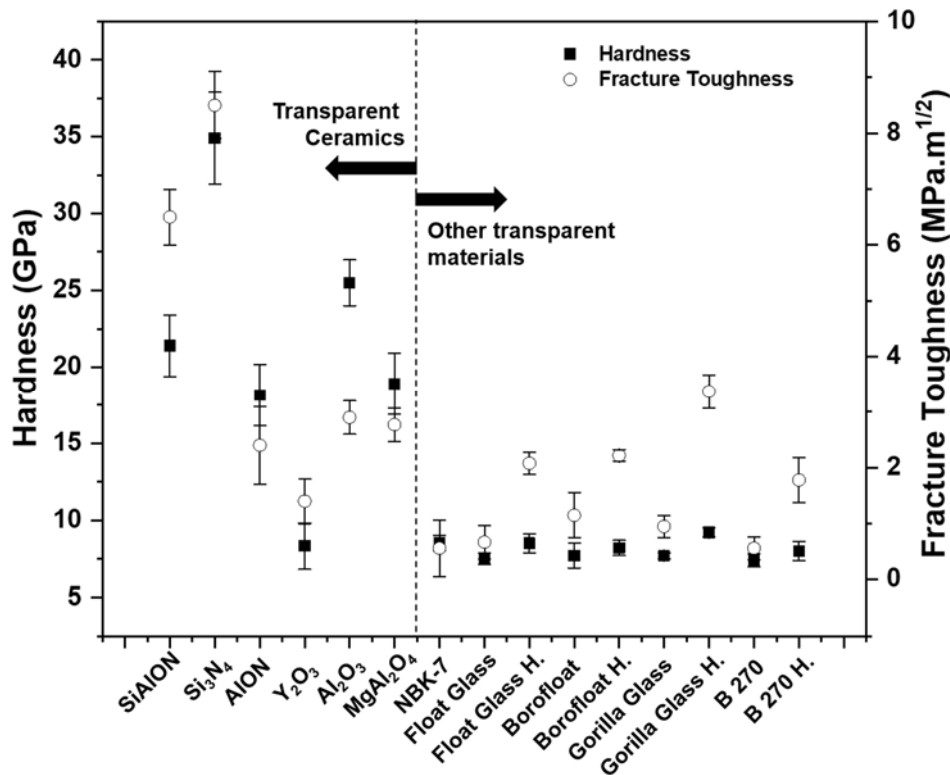


Figure 1: Hardness and fracture toughness of different transparent ceramics such as SiAlON, Si₃N₄, AlON, Y₂O₃, Al₂O₃, MgAl₂O₄, NBK-7, Float glass, Float glass hardened, Borofloat, Borofloat hardened, Gorilla glass, Gorilla glass hardened, B270, B270 Hardened [37,44,63,65,75,86,92,94,96–101,111–113].

Grain size primarily determines ceramic materials' mechanical characteristics; in general, the smaller the grain size, the stronger the ceramics. TCs have shown a prominent relationship between grain size, hardness, and fracture toughness. A bimodal distribution of the grain size is required because, on one side, larger grain size promotes transparency, whereas on the other side, fine grain size improves the tribological characteristics [39,40,52,53]. Fine-grain size increases the hardness [35,54], but the effect of grain size on fracture toughness is uncertain as the fracture toughness may increase [44], decrease [35], or remain the same [54] with a reduction in grain size. Borrero-Lopez et al. investigated the effect of three different grain sizes on the lubricated sliding wear of transparent MgAl₂O₄ ceramics [54]. Different grain sizes provide different hardness of the transparent MgAl₂O₄, resulting in different wear mechanisms (discussed in section 2.1). Moreover, TCs for windows and other tribological applications must have high-velocity impact strength along with high hardness and fracture toughness. For such uses, however, literature is still scanty.

The wavelength range of transparency of the material is defined by electron structure, while impurities may induce absorption bands. Both factors are equally relevant in the case of single crystals. Scattering effects further limit the optical quality. The scattering depends on the difference between the refractive index of the matrix (ceramics) and the scatterer, and also on the

wavelength of passing light and dimensions of the scatterers, as illustrated by Stuer et al. [45] and Pabst et al. [46]. The possible sources of light scattering are shown in **Figure 2**. In TCs, composed of randomly oriented crystalline grains, light can scatter on residual pores, secondary phases, impurity inclusions, and grain boundaries [32–34]. Therefore, the presence of these defects in TCs affects not only the tribological performance but also the transparency. To achieve the maximum theoretical transparency, TCs have to be defect-free. In general, the defect-free TCs exhibit excellent mechanical, thermal, and tribological properties as nearly-perfect materials. In the case of birefringent materials (e.g., Al_2O_3), light is further scattered at the grain boundaries of randomly oriented birefringent grains.

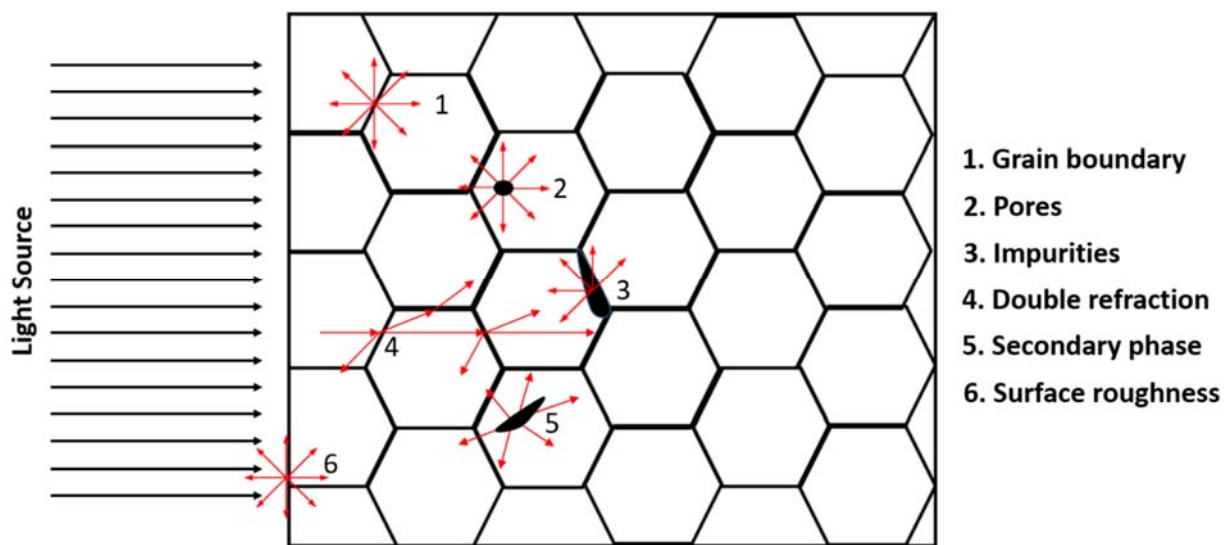


Figure 2: Different sources for scattering the light.

Most of the TCs are single-phase materials with a cubic (optically isotropic), spinel, garnet, or bixbyite crystalline structure. However, it is also possible to achieve a significant degree of transparency in the case of non-cubic materials, either by the orientation of grains [43] or by producing ceramics with a very fine grain size that are significantly below the wavelength of the passing light [7]. The latter also applies for nanocomposites, where the presence of a second phase may limit the transmittance only at shorter wavelengths (UV, visible) (e.g., $\text{MgO}/\text{Y}_2\text{O}_3$ nanocomposite [114] transparent above 1-2 μm or $\text{MgAl}_2\text{O}_4/\text{Si}_3\text{N}_4$ [48]).

Many TCs are refractory materials and the robust bond strength and coupled with a low diffusion coefficient, pose difficulties during densification at temperatures below 1500°C, often even below 1800°C. Therefore, sintering aids are generally required to obtain high-density TCs at lower temperatures or pressures [58,59]. Transparent ceramics can be manufactured by various ceramic processing techniques, including synthesis or mixing of starting powders, eventually further

powder processing (milling, granulation), shaping, heat treatments (calcination/debinding, sintering, annealing), and polishing. Compared to single crystals, TCs usually do not require secondary operations, like cutting and machining, before the final polishing step, as TCs can be prepared in near-net shape. However, compared to traditional ceramic materials, the production of transparent ceramics necessitates specific equipment, particularly for the powder synthesis and sintering processes. In particular, high-purity powders with good sinterability, low level of agglomeration and regular morphology are required to avoid introducing defects and second phases. The two main approaches are the synthesis of precursor powders and the reactive sintering of a mixture of powders, and both are widely described in literature [115–119]. Shaping approaches cover many of the commonly used techniques for transparent ceramics (e.g., dry pressing [120,121], slip casting [118], gel casting [39,122], tape casting [121,123], pressure slip casting [124], and additive manufacturing [125,126]) with particular attention on limiting potential contamination and the presence of voids. While all the process parameters have to be aligned to reach a defect-free microstructure, the focus is firmly on the characteristics of the starting powders and the sintering step.

In most cases, pressureless sintering in air does not entirely remove porosity from ceramics. Therefore, pressure-assisted sintering techniques are requested, viz. hot pressing [127,128], hot isostatic pressing [129,130]), vacuum sintering [131], spark plasma sintering [95,111,132,133], microwave sintering [134,135] or a combination thereof. Moreover, sintering aids are also very often used to enhance the densification and removal of pores, limit grain growth, and lower the sintering temperature. The high pressure-temperature technique is extensively utilized to manufacture superhard and ultrahard TCs [136,137]. These TCs have excellent wear resistance. TCs, as triboelements, can be widely employed in diverse fields. Different tribological applications where TCs can be employed include windows in re-entry vehicles, lookdown windows in aircraft and military vehicles, armor, face shields, missile tops, infrared domes protections, window floors, and space shuttle windows. Among TC materials, the effect of various processing factors on transparency has been studied extensively [138]. However, tribological properties of TC are relatively poorly studied.

Transparent ceramics with better mechanical properties have been identified as the next-generation transparent materials for tribological applications. Salem studied the mechanical characteristics of translucent AlON and MgAl₂O₄ ceramics considering their utilization in spaceship windows [22]. However, the processing and characterization of TCs are difficult and costly [24,59,115,139,140]. Therefore, modelling and simulations are used to predict mechanical

and tribological performance in extreme conditions [33]. Moreover, the literature on TCs reveals that the modelling of scattering by residual pores and the resulting transmittance predictions can be made using the Mie theory [32,33,46,141]. Approximation techniques may be used to model the effect of tiny pores and huge pores (compared to the wavelength of light) based on the Rayleigh approximation and the Fraunhofer approximation, respectively. Recent research indicates that the Rayleigh-Gans approximation provides better results than the Rayleigh approximation in small-size regions. The van de Hulst approximation (also known as the anomalous diffraction approximation) [142] is the only approximation capable of predicting the decrease in in-line transmittance as pore size increases in the small-size region and the increase in transmittance as pore size increases in the large-size region. Indeed, the Van de Hulst approximation provides transmittance predictions that are the most closely related to the exact Mie theory predictions over a wide range of pore sizes [33]. These modelling techniques can be used to predict the optical, mechanical, and tribological properties of newly synthesized TCs, thereby saving money and time.

The purpose of this review is to deliver a theoretical framework for the tribological properties of transparent ceramic materials. Different types of TCs used for tribological applications have been explored. This review discusses the impact of microstructure and mechanical characteristics of TCs on tribological performances, without neglecting the importance of the optical transparency. In this view, wear testing, and scratch testing of TC materials have been reviewed to understand the mechanical and tribological properties. This approach provides insight into different TC's surface deformation characteristics and material removal mechanisms. In addition, a significant part of the study has been devoted to understand the dominant processes of material removal as a function of microstructure and mechanical properties of transparent ceramics when they are subjected to wear conditions. The following section will discuss different transparent ceramics used in different tribological conditions.

2. Different transparent ceramics for tribological applications

. Transparent ceramic material must be developed beyond the state of art with high durability, efficiency, improved performance, lightweight, and high strength, in order to fulfil the requirements of the different application fields [22]. Transparent ceramics used for tribological applications require excellent hardness, fracture toughness, and elastic modulus (better contact damage resistance) [58,59]. In addition, the properties like high compressive strength (relevant for applications requiring high load at tribo-contact), low density (better specific properties than many metals), and high melting and mechanical property retention at elevated temperature (high-

temperature tribological applications) are also required for the tribological applications mentioned above. Friction and wear behaviour of TCs, which are the critical components for operation in various tribological applications, have been discussed extensively [143–145]. However, there is scarcity in the research of tribological and mechanical behavior of transparent ceramics. Since the main focus is on tribological applications, TCs with low strength have been excluded in this review. The most promising transparent materials with the highest strength and potential tribological properties are MgAl_2O_4 , Al_2O_3 , AlON, Lu_2O_3 , c-BN, Y_2O_3 , Si_3N_4 , and SiAlON, and are therefore discussed in the present review [27,59].

2.1 MgAl_2O_4

MgAl_2O_4 (spinel) has a high potential as transparent armor ceramics and protective windows and domes for sensor application. It provides a high levels of optical and mechanical performance required by these types of applications [146,147]. Earlier research has shown that such transparent windows require excellent mechanical and tribological properties, i.e., hardness, fracture toughness, wear resistance with high transmission, and a suitable refractive index [35]. MgAl_2O_4 is transparent from UV to mid-IR (from 0.2 to 5.5 μm) [11,146] and exhibits a density of 3.578 g/cm^3 . The advancement of fabrication technology and the quality of raw powders have resulted in the production of large size MgAl_2O_4 ceramics with high optical quality, making them suitable for use in transparent armor, domes, and windows for applications in ultraviolet (UV), visible (VIS), and infrared (IR) [117,146].

Fabricating transparent MgAl_2O_4 ceramics via pressureless sintering is challenging [34,148] and therefore, advanced sintering techniques like hot pressing (HP), hot isostatic pressing (HIP), and spark plasma sintering (SPS) are required for its manufacturing [97,149–152]. Sintering aids used to produce transparent spinel ceramics are LiF [153], B_2O_3 [154], and CaO [155,156]. It is possible to prepare transparent spinel ceramics without sintering aids [157], but the use of sintering aid helps to achieve maximum transparency.

To understand the tribological behaviour of transparent MgAl_2O_4 , a sandblasting experiment was carried out for five minutes on the surface of transparent MgAl_2O_4 . It was observed that the mass loss from the surface was 2 mg (0.06%), which is very low compared to other glasses with a mass loss value ranging from 6.8 to 114.8 mg (0.3-4.7%). The surface roughness and maximum crater depth in the transparent MgAl_2O_4 spinel were found to be $0.1 \pm 0.01 \mu\text{m}$ and 3 μm , respectively. The surface roughness of the different glasses was found to be in between $1.1 \pm 0.1 \mu\text{m}$ to $3.7 \pm 0.4 \mu\text{m}$, while the maximum crater depth was 4 μm to 229 μm [66]. It shows that transparent MgAl_2O_4

exhibits an excellent wear resistance, much higher compared to glasses, with low surface roughness and crater depth. **Figure 3** represents various cracks (radial, median, and lateral cracks) formed during the scratch test of transparent material with increasing load. Three regimes were developed during scratch, i.e., micro-ductile, micro-cracking, and micro-abrasive. In the micro-ductile regime, the cracks formed are underneath. During micro-cracking, radial and lateral cracks are formed, which results in chip formation of the transparent material. However, debris formation is observed in micro-abrasive regime.

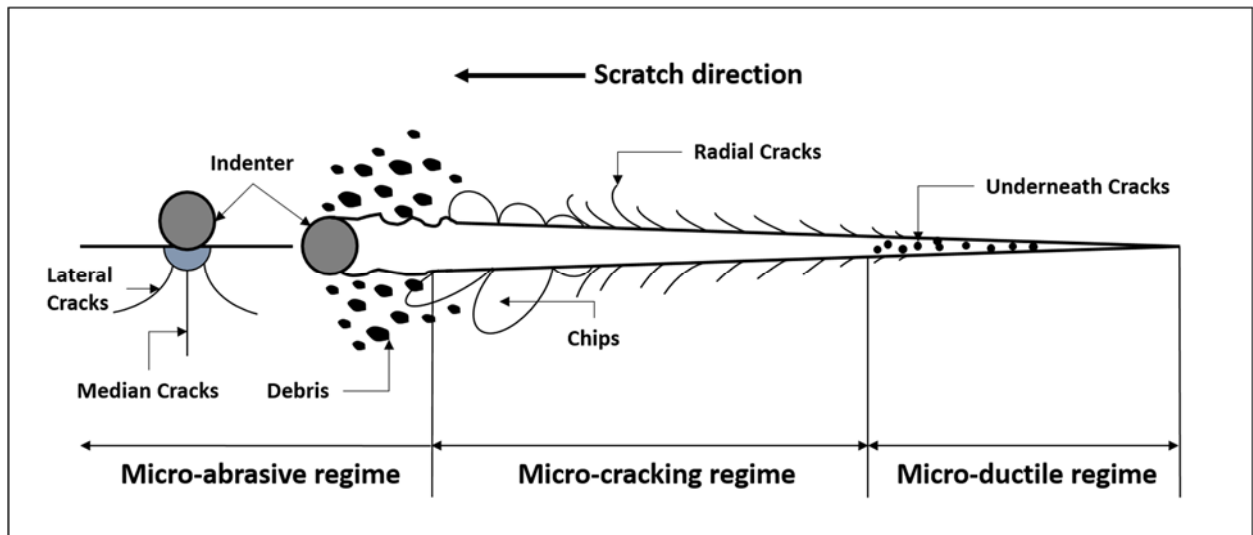


Figure 3: Typical scratch patterns on brittle materials during a progressive scratch [66].

The optical transmittance and tribological and mechanical properties are improved with the reduction of porosity. Moreover, the wear resistance can be further improved by the reduction of grain size. Benaissa et al. [35] prepared transparent MgAl_2O_4 without any sintering aid using SPS at different temperatures. The microstructure of transparent MgAl_2O_4 without any sintering additive at different sintering temperatures is shown in **Figures 4a-4c**. Sintering of the powder was done at 73 MPa pressure with three different sintering temperatures, i.e., 1300 °C (**Figure 4a**), 1350 °C (**Figure 4b**), and 1400 °C (**Figure 4c**). The heating rate was 100 °C/min to 800 °C, 10 °C/min to 1100 °C, and 1 °C/min to final temperature. With an increase in sintering temperature, the relative density of the material dropped slightly and it was found to be 99.93%, 99.63%, and 99.58% at 1300 °C, 1350 °C, and 1400 °C, respectively. At wavelength of 550 nm, the transmittance was 70%, 45%, and 6% for 1300 °C, 1350 °C, and 1400 °C, respectively, owing to the reduced relative density and increased porosity. The use of sintering aids for the production of spinel by SPS can change the microstructure both in terms of porosity and grain size [158,159].

The tribological properties may also be affected by the use of dopants or additives as the grain boundary and grain size of the TC maybe altered. This may reduce the porosity and improve the

tribological behaviour. Esposito et al. [60] examined the effect of LiF (0 to 1 wt %) doping in MgAl₂O₄ on the microstructure of the transparent ceramics sintered by hot pressing. The transparent MgAl₂O₄ without additive obtained by HP at 1600 °C for 60 min exhibits a bimodal microstructure as shown in **Figures 4d**. Pore-free TC with equiaxed grains of approximately 38µm and fine grains of approximately 3µm size with intergranular pores were observed when no LiF was used (**Figure 4d**). The addition of LiF to the MgAl₂O₄ provides uniformity in the microstructure of TC. LiF acts as a sintering aid as 0.5% LiF produces TCs with a grain size of 20 µm without any residual porosity (**Figure 4e**). Adding 1% LiF to MgAl₂O₄ processed under the same conditions results in a more uniform microstructure with an average grain size of less than 20 µm (**Figure 4f**). The addition of LiF promotes a fine structure and low porosity and may improve the hardness and in turn the tribological characteristics.

Nassajpour et al. [48] prepared MgAl₂O₄/Si₃N₄ nanocomposite using MgAl₂O₄ and Si₃N₄ powders of average particle sizes of 250 nm and 40 nm, respectively. The TC was obtained using SPS with maximum pressure and temperature of 80 MPa and 1550°C for 20 min. The microstructures of MgAl₂O₄-1wt% Si₃N₄ and MgAl₂O₄-3wt% Si₃N₄ are shown in **Figure 4g** and **Figure 4h** respectively. The hardness obtained for pure MgAl₂O₄, MgAl₂O₄-1wt% Si₃N₄, and MgAl₂O₄-3wt% Si₃N₄ was 7.7, 8.1, and 10.2 GPa respectively. Increasing the Si₃N₄ concentration in the spinel-based composite increased its hardness. This is because small-scale bridging bonds developed in the spinel composite structure during sintering, which increased the strength at the surface. After heat treatment, the hardness of pure MgAl₂O₄, MgAl₂O₄-1wt% Si₃N₄, and MgAl₂O₄-3wt% Si₃N₄ samples increased to 8.2, 9.3, and 12.1 GPa, respectively. This rise in the hardness indicates the presence of superficial oxidation on the surface which caused compressive stress on the nanocomposite's surface. The sample MgAl₂O₄-1wt% Si₃N₄ exhibits the greatest shear strength. The regions under the shear stress-displacement curves for pure MgAl₂O₄ and MgAl₂O₄-1wt% Si₃N₄ are almost identical and nearly twice as large as those for sample MgAl₂O₄-3wt% Si₃N₄. It indicates that adding 3% Si₃N₄ significantly reduces the fracture toughness of MgAl₂O₄-based nanocomposites. The addition of a second phase to the ceramic matrix may impact the sintered composite's reinforcing mechanism. While adding a second phase to the matrix may toughen the ceramic through multiple processes ranging from crack deflection to fracture bridging, grain growth inhibition is the primary mechanism in this instance. It means that Si₃N₄ particles may significantly impair grain development. The inclusion of Si₃N₄ at a concentration of up to 1% had no detrimental effect on the fracture toughness of nanocomposite samples. However, when 3% Si₃N₄ was added to the matrix, fracture toughness fell substantially, since it was also

accompanied by a significant increase in the volume percentage of voids, which accounts for most of the dispersion hardening effect [48].

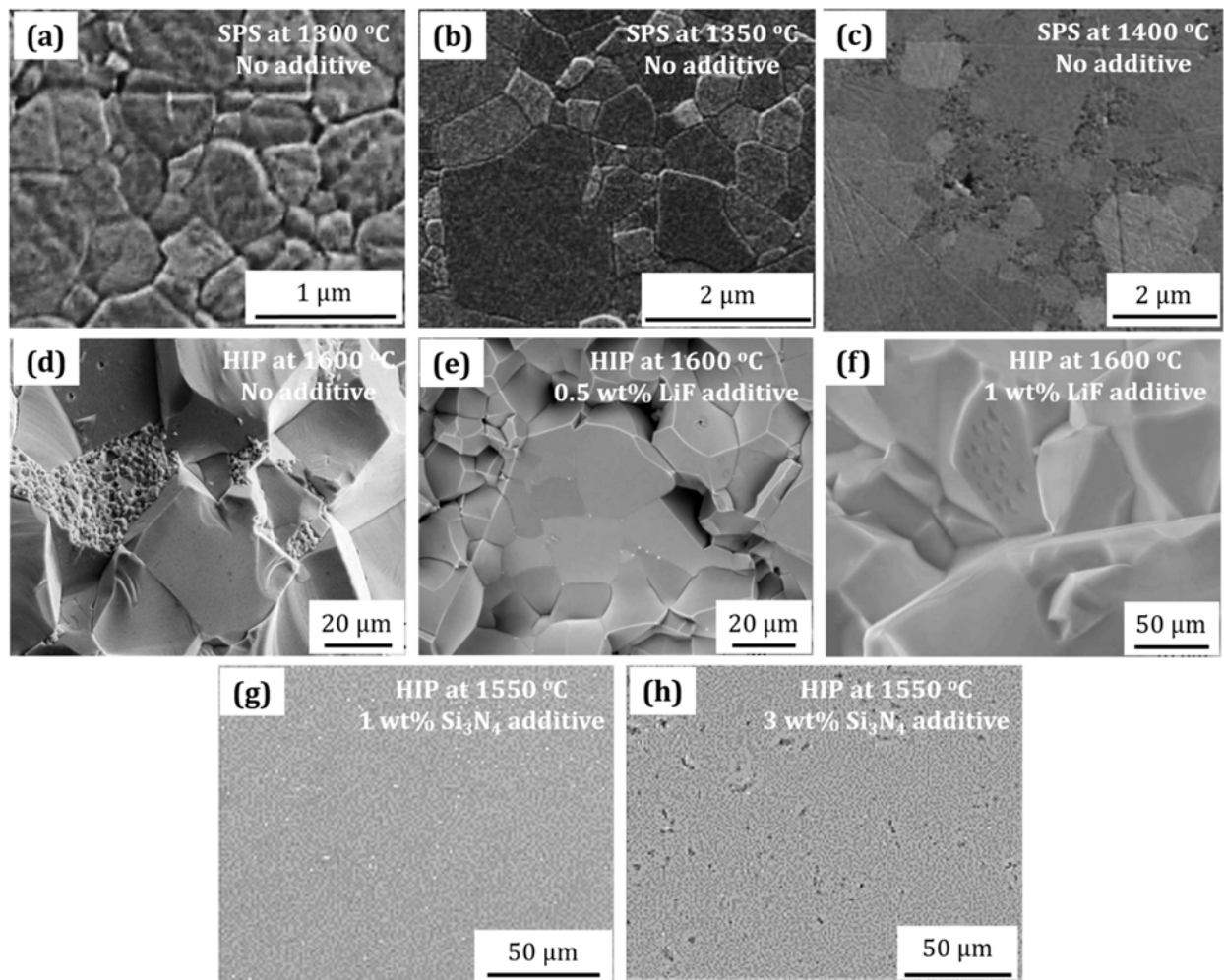


Figure 4: Microstructure of $MgAl_2O_4$ obtained a), b), c) via SPS at different temperature without additive [35], d) via HIP without additive [60] e), f) via HIP at different temperature with 0.5 wt% LiF and 1 wt% LiF [60], g) and h) via HIP at different temperature with 1 wt% Si_3N_4 and 3 wt% Si_3N_4 [48].

Toughening and strengthening mechanisms also improve the tribological properties of the TCs [49,50]. Sheikh et al. [51] studied the effect of toughening on hardness, fracture toughness, and transparency for transparent $MgAl_2O_4/Si_3N_4$ nanocomposite sintered by SPS. The average particle size of $MgAl_2O_4$ and Si_3N_4 nanopowder was 40-50 nm and 30-40 nm, respectively. The synthesised transparent $MgAl_2O_4$ -2 wt% Si_3N_4 showed spherical grains of 5 μm size and density of 3.561 g/cm^3 (99.8% of the theoretical density). The nanocomposite experiences a reduction of 60% transparency compared to pure spinel. Also, the heat treatment did not led to any variation in the optical transmittance of the nanocomposite. However, a significant improvement in the mechanical properties of the nanocomposite was observed after heat treatment 1000°C such as an increase of approximately 4% increase in the elastic modulus of $MgAl_2O_4/Si_3N_4$ nanocomposite compared to pure $MgAl_2O_4$. The hardness (14.7 ± 0.1 GPa) and fracture toughness (1.68 ± 0.04

MPa.m^{0.5}) of MgAl₂O₄/Si₃N₄ nanocomposite was found to be in the same order as the hardness (14.1±0.1 GPa) and fracture toughness (1.67±0.05 MPa.m^{0.5}) of pure MgAl₂O₄. Heat-treated nanocomposite material improved instead the TC's hardness (16.3±0.1 GPa) and fracture toughness (2.1±0.06 MPa.m^{0.5}). The decrease of transparency and enhancement in mechanical properties is due to the presence of Si₃N₄ nanoparticles that scatter light but at the same time reinforce the material by toughening mechanism. As was shown in the case of pore size [45], if the size of the scatterers is sufficiently small, a deleterious effect on transparency is reduced.

In MgAl₂O₄ with a coarse microstructure (grain size ≈50μm), intergranular fracture was observed and a fracture toughness of 1.4-2 MPa.m^{0.5} was measured [160]. The low fracture toughness of transparent MgAl₂O₄ has been linked with grain-boundary embrittlement induced by additive, impurities, or residual stress [146]. A tearing resistance curve, or R-curve, indicates a material's resistance to progressive crack growth (implying that the fracture toughness of the material varies with crack development). As a result, a tearing resistance curve is a function of fracture toughness and crack growth [161]. Coarse-grained microstructures of MgAl₂O₄ exhibit limited resistance to crack propagation due to grain bridging and wedging induced by friction and therefore low tearing resistance is provided by coarse grained transparent MgAl₂O₄. Porosity and second phases are not necessarily the only flaws that must be limited (0.01 % porosity) in transparent ceramics for tribological applications: coarse-grained microstructures have also been recognized as a source of weakness [162]. Microstructure refinement leads to significant increases in hardness for grain sizes as low as 1 μm as determined by Hall–Petch relationship. Even though hardness of MgAl₂O₄ increases significantly with microstructural refinement which increases the erosion resistance during penetration, the exact mechanism by which wear varies is unclear.

Nonetheless, one of the primary goals of transparent spinel processing is to decrease the particle size of the finished product. The cost of transparent armor, on the other hand, outweighs the minor hardness advantage associated with small particle sizes, and grain sizes in the hundreds of microns are often acceptable. It is difficult to determine the effect of grain size on ballistic performance because of the complexity of the failure mechanism, the high costs of the tests and the limited available reports on that. Even though spinel is susceptible to fracture formation, which is assisted by moisture, the effect is most apparent in coarse-grained microstructures. Although there seem to be no delayed fracture development studies for single crystals, the findings emphasize the vital role that grain boundaries play on influencing the strength of materials [31]. Other than armor application, the TCs has a potential to be used for biomedical application as wear resistant load bearing implant, which generally experience fretting wear in the joint. At present, two materials,

i.e., MgAl_2O_4 and AlON compete with single crystals for such applications. Bodhak et al. [28] compared the tribological characteristics of these two ceramics in freshly prepared medium, i.e., stimulated body fluid at 37°C . It was observed that the wear rate of MgAl_2O_4 was 62% lower than that of AlON for 1000 m test run and 47% less for 3000 m test run (**Figure 5**).

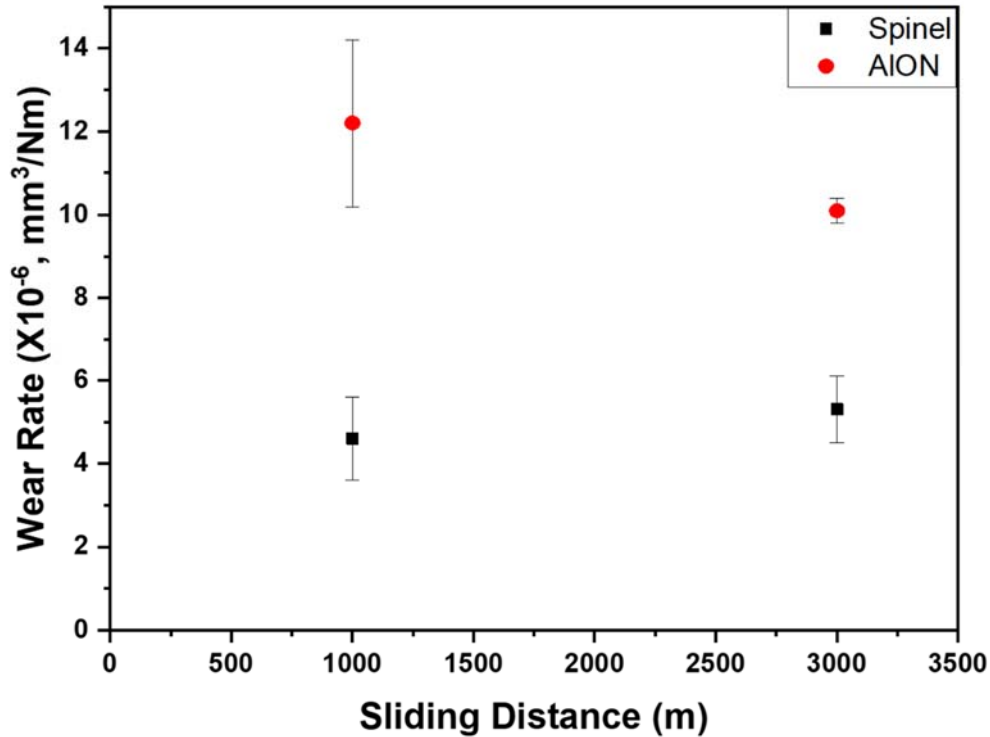


Figure 5: Wear rate of Spinel and AlON [28].

As mentioned above, the porosity present in the TC influences the transparency, hardness, elastic modulus, and fracture toughness of the material (**Figure 6**). The tribological characterization on the flat surface of the spinel TCs was measured using alumina balls of 6 mm as contact means for 6 min at 20 N load and 100 rpm [35]. The resulting coefficient of friction was 0.06 and 0.13 for samples fabricated at sintering temperatures of 1300°C and 1350°C , respectively. **Figure 6** shows that the wear resistance of transparent spinel was improving with decreasing sintering temperature, which results in an increase in hardness due to smaller grain size, and decrease in fracture toughness. Also, low friction coefficient was observed with decreasing sintering temperature. The reduction in fracture toughness is due to the slight increase in porosity for the samples sintered at 1400°C compared to 1300°C . Slight porosity deflects the direction of movement and spread a high energy crack in several low energy cracks which cannot propagate too far as compared to the high energy ones. However, the presence of pores compromises the transparency of the ceramics. The sintering temperature must be kept low to fulfill the requirement of high hardness. So, it can be concluded that porosity is a more prompting factor than grain size for good wear resistance. A

small grain size with high density, hardness, and transmittance is observed at low sintering temperatures. In contrast, large grain size with high fracture toughness and low transmittance is observed at high sintering temperatures. Therefore, the optimum sintering temperature is required to achieve high wear resistance and transparency.

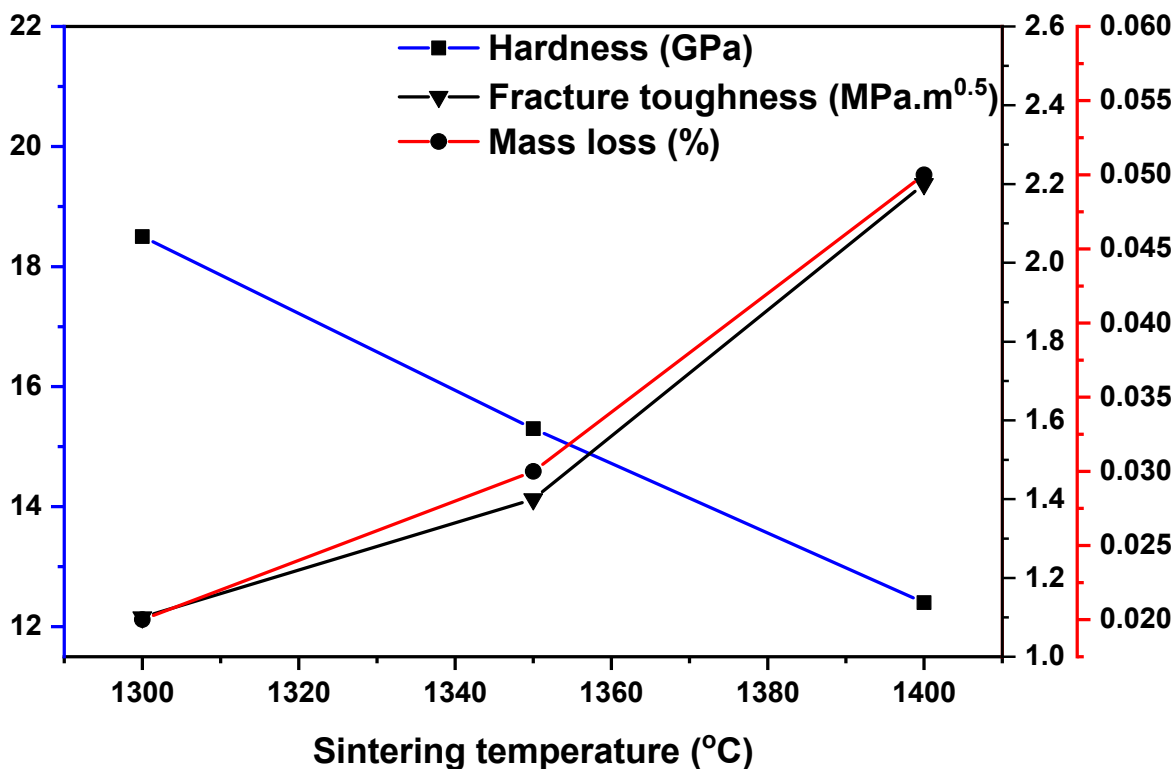


Figure 6: Hardness, fracture toughness and mass loss upon friction vs. sintering temperature of spinel [35].

Bodhak et al. [28] fabricated a disc shaped sample of MgAl_2O_4 by conventional powder processing routes followed by sintering, grinding, and polishing with average surface roughness (r.m.s) $\approx 0.001 \mu\text{m}$ for an application like total hip arthroplasty and total knee arthroplasty. The TC formed was analyzed for tribological characteristics as these applications experienced fretting wear in the joint. A linear-reciprocating ball on a disc testing tribometer was used for all the experiments. A linear oscillatory motion of 10 mm was made with a constant load of 20 N and a constant speed of 5000 mm/min with Al_2O_3 as a counter body. Wear rate for distances 1000 m and 3000 m was measured to be $4.72 \pm 1.22 \times 10^{-6} \text{ mm}^3 \text{ Nm}^{-1}$ and $5.27 \pm 0.85 \times 10^{-6} \text{ mm}^3 \text{ Nm}^{-1}$, respectively. Volume loss for similar distances was estimated to be $0.094 \pm 0.02 \text{ mm}^3$ and $0.316 \pm 0.05 \text{ mm}^3$, respectively. Hardness and friction coefficient value of fabricated MgAl_2O_4 sample was $13.09 \pm 0.71 \text{ GPa}$ and 0.43 ± 0.009 .

The strength of the spinel may be enhanced by grain refinement while preserving its transparency in infrared (IR) wavelength range, as shown recently in a nanostructured transparent spinel with

an average strength of 470 MPa and Weibull modulus of 6.2 [88]. Nanostructured spinel is fragile and its strength is susceptible to deterioration through the development of defects during service. It is very important in IR windows/domes since the spinel are exposed to extreme loading conditions during high-speed missile flight. As a result, there is a need for transparent ceramics that are not only strong but also damage-tolerant and perform well under the harsh circumstances of service. In this aspect, the insertion of reinforcements, such as particles, whiskers, or fibers, into ceramic matrices, may improve the damage tolerance of the toughened composites. When the size of the reinforcement is limited and no clustering occurs, transparency may be maintained at longer wavelengths. For creating a well-dispersed slurry, a spinel powder was combined with 2.5 vol% Si_3N_4 (average particle size 50 nm) and 0.5 vol% Y_2O_3 (average particle size 10 nm). The slurry was spray dried and the globular powder was pressed at 50 MPa and heat-treated at 500°C for 24 hours. The samples were then HP at 60 MPa pressure at 1300°C for 3 hours. Some samples were again heat-treated at 1000°C for 4 hours to strengthen the $\text{MgAl}_2\text{O}_4/\text{Si}_3\text{N}_4$ composite. The relative density of the fabricated composite material was found to be 99.5%. TEM microscopy revealed that Si_3N_4 was present as a nanodispersoid with grain size of 100 nm within a polycrystalline spinel matrix of 300 nm [141]. The transmission was 70 % for IR radiations of wavelength 3-4.5 μm . The reduction in transparency was attributed to the presence of Si_3N_4 grains and the residual porosity. The results showed a 29% increase in strength and an 85% increase in fracture toughness compared to processed TCs. From the previous discussion, we can conclude that the rise in fracture toughness may vary the tribological characteristics of the TC by reducing the wear resistance properties [141].

It can be summarized that the transparent MgAl_2O_4 can be fabricated without an additive, but it exhibits a bimodal microstructure with low transparency. The addition of a second phase impacts on the sintered reinforcing mechanism. The addition of LiF or Si_3N_4 to MgAl_2O_4 results in fine structure and low porosity, improving the hardness and tribological characteristics of the TCs and their transparency. The improvement in the mechanical and tribological properties is only up to a specific percentage increase of additive, i.e. below 2-3 vol%. Therefore, an optimum quantity of additives is required to be added.

Various cracks, i.e., radial, median, and lateral, are formed during the scratch test of transparent material with increasing load. The development of small-scale bridging bonds in the spinel composite structure during sintering is required to increase the surface strength. A post sintering heat treatment improves the mechanical and tribological properties of TCs. The porosity factor sometimes overcomes the fracture toughness factor for wear performance. The porosity in the TC

also increases the fracture toughness value of the material but leads to deterioration in the wear resistance. So, for good wear resistance properties, low porosity, fine grain size, high hardness, and fracture toughness must be targeted by keeping low sintering temperature, allowed in particular by the use of SPS.

2.2 Al_2O_3

Alumina (Al_2O_3), is one of the earliest transparent ceramics which has found significant commercial success [163]. Alumina is used widely due to its low cost, biocompatibility, and appropriate mechanical, chemical, electrical, and thermal properties. It has potential for tribological applications, such as transparent electromagnetic dome structures, armors, envelopes, and windows. The tribological and mechanical properties of Al_2O_3 ceramics can be optimized by controlling the grain size [39,40,164]. For altering the grain size of the transparent Al_2O_3 , different processing techniques and sintering aids can be used. A theoretical maximum in-line transparency of polycrystalline Al_2O_3 is found in the infrared wavelength range between 2000 and 4000 nm [122,165]. The main drawback of Al_2O_3 as a TC is the birefringence [23], which limits the thickness for which the material can be transparent. A reduction of grain size is an approach that allows to further improve transparency, even at lower wavelengths.

SPS is demonstrated to be a reliable process for producing transparent polycrystalline alumina with real inline transmittances greater than 50% (for 640 nm, 0.8mm thickness) [166]. Despite the short sintering cycles (usually 15 minutes) of SPS, it was shown that doping is essential to provide satisfactory optical characteristics in polycrystalline alumina [166,167]. The SPS of pure alumina cannot prevent substantial grain development, leading to the presence of pores at the grain boundary (**Figure 7a**). Therefore, sintering of Mg-, Y-, and La-doped submicron alumina was examined using SPS [166] which successfully suppressed grain growth. The microstructures of sintered samples at 1350 °C with Mg, Y, and La as doping agents are shown in **Figures 7b, 7c, and 7d**, respectively. Compared to single doping techniques, co-doping each pairing often improves the transparency by lowering the grain size [166]. Triple doping with Mg, Y, and La in equal proportions resulted in the highest real inline transmittance of 57%. Such high transmittance coupled with very fine grain size is made possible with SPS and needs high sintering pressures and low sintering temperatures. The findings of this work should pave the way for more research and development of transparent polycrystalline alumina generated by fast sintering methods such as SPS. Polycrystalline Al_2O_3 ceramics prepared by pressureless pre-sintering followed by HIP at 198 MPa for 3 hours between temperature range from 1190 °C to 1295 °C revealed an in-line

transmission of up to 70.4% at a wavelength of 632.8 nm for 0.8 mm sample thickness [165]. Al₂O₃ ceramic was doped by ZrO₂ (0.3 wt%) and MgAl₂O₄ (0.175 wt%) by gel-casting and then sintered. Grain size refinement in the completely dense alumina structure can be observed in **Figure 7e**. A similar method, i.e., pre-sintering followed by HIP, was also followed for Al₂O₃ with 0.03 wt% MgO and 0.2 wt% ZrO₂ which resulted in 60% in-line transparency at 650 nm wavelength for 0.8 mm sample thickness. The sintered sample had a grain size of approximately 0.5 μm (**Figure 7f**) and 99.9% relative density with 20–21 GPa hardness. The developed TC (600–700 MPa four-point bending strength and 750–900 MPa three-point bending strength) is suitable for scratch-resistant windows and transparent Al₂O₃ armour. Therefore, it is possible to fabricate sophisticated hollow components and big flat windows with good wear resistance properties of sintered and HIPed Al₂O₃ using Al₂O₃ powder and a gel-casting method.

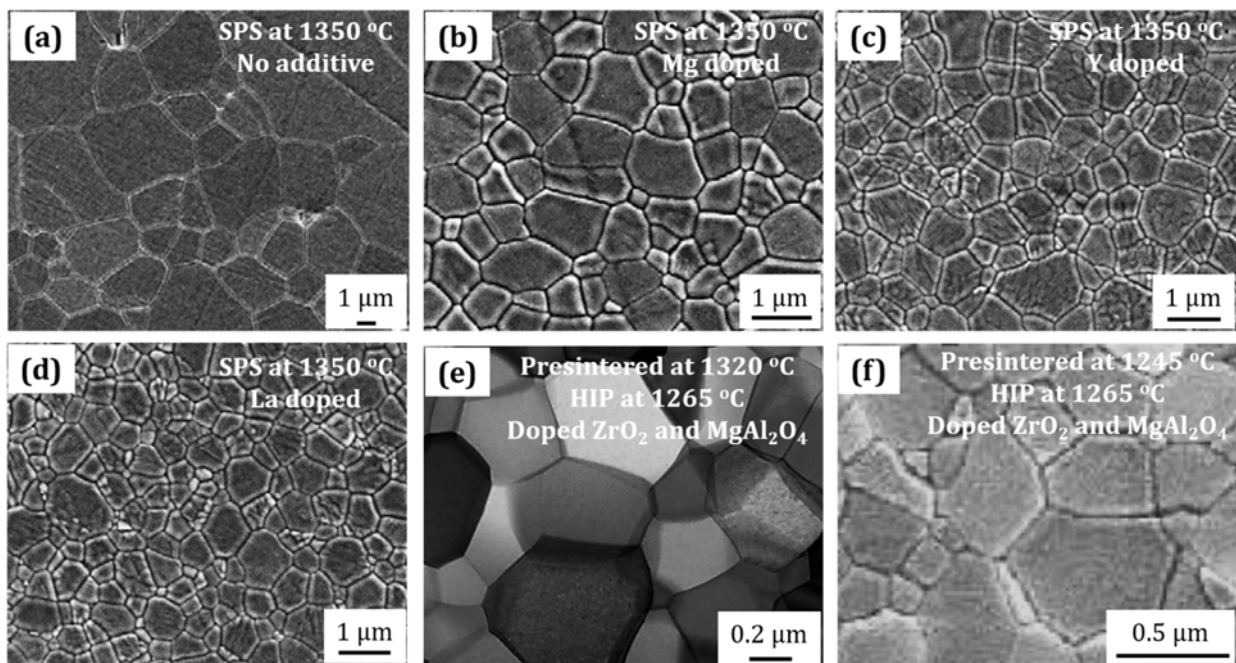


Figure 7: Microstructure of Al₂O₃ obtained via SPS at 1350 °C a) pure and doped with b) Mg, c) Y and , d) La [166], or e) doped by ZrO₂ and MgAl₂O₄, [165] and f) by ZrO₂ and MgO, presintered and HIPed [39]

Transparent Al₂O₃ ceramics have been produced (flat windows 0.8 mm thick) with real in-line transmittance of nearly 60% with submicron grain size (0.4-0.6 μm), high hardness (HV10 20-21 GPa), and strength (four-point bending 600-700 MPa; three-point bending 750-900 MPa) [39]. It was found that doped Al₂O₃ transparent ceramic prepared using SPS technique resulted in higher transparency than pure Al₂O₃ [166,167]. However, Al₂O₃ transparent ceramic, doped with aluminium ethoxides, prepared using SPS technique results in higher transparency than pure Al₂O₃[166]. It was investigated that doping with aluminium ethoxide (0.1-1 wt%) leads to form α-Al₂O₃ nanoparticles, which minimizes grain growth and changes the sintering mechanism from

volume to grain boundary diffusion. The nucleated particles, which provide the energy barrier during sintering, block grain reorientation required for the diffusion of the grains during sintering. α -Al₂O₃ nanoparticles at the grain boundaries of the Al₂O₃ thus decrease the grain mobility and, in turn, prevent the joining of the grains. Due to the steric impediment provided by the α -Al₂O₃ nanoparticles and reduction in the grain size of the TC, it can be concluded that the addition of aluminium ethoxide to Al₂O₃ reduces the wear resistance of the TC.

The optical, microstructural, mechanical, and fracture properties of Er³⁺ doped transparent alumina produced by co-precipitation method were investigated [75]. The real in-line transmittance of Er³⁺ doped samples was in the range of 55–59% for 1 mm thickness, which belongs to higher transmittance values in comparison with transmittance found in the other research [39]. Segregation of Er atoms at the grain boundaries probably caused a reduction of grain boundaries mobility, which led to decreasing the mean grain size (0.33–0.35 μ m) compared to undoped alumina. The Vickers hardness of the Er³⁺ doped alumina was measured at different loading conditions, achieving 26.9 GPa at 10 N load. The fractography analysis showed a higher transgranular character of fracture surface in Er³⁺ doped alumina compared to undoped alumina, confirming the enhanced grain boundary cohesion due to Er doping. The indentation fracture toughness of Er³⁺ doped alumina was in the range 2.1–2.2 MPa.m^{0.5}. Therefore, Er³⁺ doped Al₂O₃ is a suitable combination of superior optical and mechanical properties [75].

It can be concluded that transparent Al₂O₃ ceramics' optical and mechanical qualities rely on grain size and residual porosity. Various methods have been used to manage grain size and porosity. The mechanical strength and optical transparency of transparent Al₂O₃ ceramics were significantly improved with a decrease in grain size of TC. Al₂O₃ exhibits a Vickers micro-hardness of HV10 GPa to HV 27 GPa (at 10 kgf load). When the grain size of sintered alumina is reduced to the submicron range, a considerable improvement in hardness is produced. The fine grain size is accompanied by a high relative density and a low frequency of defects. Dopants like Mg, Y, La, ZrO₂, and MgO significantly improved the mechanical properties of the TC by altering the microstructure. Er atoms on the grain boundary causes a reduction of grain boundaries mobility, which led to decreasing the mean grain size. The wear resistance of transparent Al₂O₃ increases by strengthening grain boundaries, providing micro-mechanical stability. During scratch test, crushing, cracking, and delamination of the TC occurs. Self-doped Al₂O₃ transparent ceramic prepared using SPS technique provided higher transparency than pure Al₂O₃. Such high transmittance is only possible with SPS and needs high sintering pressures and low sintering

temperatures. The Vickers hardness of the Er³⁺ doped alumina was one of the hardest (26.9 GPa at 10N load) materials in this category.

2.3 AION

Yamaguchi and Yanagida discovered aluminium oxynitride (AION), a spinel structure in the pseudo binary Al₂O₃-AlN system [168]. Based on tests and theoretical calculations, the most acceptable model is McCauley's constant anion structural model with the formula Al_{(64+x)/3}V_{(8-x)/3}O_{32-x}N_x (where V refers to cation vacancies and 2 ≤ x ≤ 5) [24]. McCauley was the first to use reactive sintering to create translucent AION ceramics using Al₂O₃ and AlN as raw materials [68]. Ish-Shalam [169] then adopted a carbothermal reduction and nitridation process to synthesize AION powder, which was then used to make translucent AION ceramics. Raytheon [27] developed and commercialised large-scale transparent ceramics with exceptional optical quality over several decades. The transmission range of AION can extend from 0.2 μm in the UV through the visible to 6.0 μm in the infrared, which makes it a very useful material for many optical applications [168]. The high strength and high hardness make AION an ideal material for transparent armor products [170]. Transparent AION exhibit superior slow crack resistance relative to fused silica [22] and has a potential in spacecraft window systems [77]. Transparent windows of AION are produced in various sizes ranging from 8 to 24 inches and even greater. AION has similar mechanical and thermal properties to that of polycrystalline alumina. Because of superior mechanical, tribological, and optical properties Raytheon Company (now Surmet) has used AION for IR domes for missiles for many years. Compared to Al₂O₃, AION has the advantage of cubic crystal structure and thus of optical isotropy.

Among the various types of processes to manufacture transparent AION, the typical method of pressing has been widely employed due to its simplicity, time-saving, and low cost [171]. The manufacture of highly transparent aluminium oxynitride (AION) ceramics in a variety of sizes and forms was accomplished using non-aqueous tape-casting forming method [123]. The tape-casting process employs both warm and cold isostatic pressing, which improves the microstructure and density of the AION green tapes. This technique was used to obtain transparent AION ceramics with pressureless sintering at temperature of 1800°C for 8 hours [123,160]. The finished product has a transmittance of 84 % at wavelength of 2000 nm. AION has hardness and fracture toughness value of around 18 GPa and 1.4 MPa.m^{0.5}, respectively. The improvement in these mechanical properties may result in good wear resistance resulting enhanced tribological properties. The microstructure of AION is shown in **Figure 8a**.

Bodhak et al. [28] studied in vitro tribological properties of transparent AlON ceramics for implant applications. Tribometric tests with 3 mm Al₂O₃ ball performed in a simulated body fluid at 37 °C provided wear rate of the order of 10⁻⁶ mm³ Nm⁻¹, much lower compared to Al₂O₃ on Al₂O₃ or ZrO₂ on ZrO₂ reported in other publications [89,172,173]. A linear-reciprocating ball on a disc testing tribometer was used for all the experiments. A linear oscillatory motion of 10mm was made with a constant load of 20N and a constant speed of 5000 mm/min with Al₂O₃ as a counter body. Wear rate for distances of 1000 m and 3000 m was 12.5±2.16 x 10⁻⁶ mm³ Nm⁻¹ and 10.1±0.27 x 10⁻⁶ mm³ Nm⁻¹, respectively. Volume loss for similar distances was estimated to be 0.250±0.01 mm³ and 0.606±0.03 mm³, respectively. Hardness and friction coefficient value of fabricated MgAl₂O₄ sample was 15.14±0.46 GPa and 0.46±0.02.

The tribological behaviour of AlON depends on the sintering additives. Zhao et al. [174] added nano-sized silicon carbide (SiC) and zirconia (ZrO₂) particles to AlON produced by hot-press sintering, which significantly increased the mechanical characteristics (relative density, microhardness, Young's modulus, flexural strength and fracture toughness) than AlON fabricated without additive. Zirconium nitride (ZrN) phase was observed to have formed as a result of the addition of nanoparticles during sintering. The majority of the SiC and ZrN nanoparticles were positioned at the grain boundaries of micro-scale AlON particles and limited the expansion of AlON grains owing to the pinning action of SiC and ZrN nanoparticles, as shown in **Figure 8b**. It causes the reduction in the grain size in nanoparticulate reinforced composites. The reinforcement and grain size reduction can reduce the crack propagation and the wear of the TC.

Liu et al. [175] fabricated transparent MgAlON ceramic with the composition Mg_{0.27}Al_{2.58}O_{3.73}N_{0.27} exhibiting a maximum transmittance of 84% by pressureless sintering of fine single-phase powders. The sintered sample exhibits excellent in-line transmittance, which is due to the high density and the rare pores coupled with a high purity, as shown in **Figure 8c**. Transparent MgAlON ceramic exhibits a broad transparency range from 0.22 to 6.24 μm, excellent mechanical properties, dielectric constant of 9.19 MHz at 1 MHz, and thermal conductivity of 8.16 Wm⁻¹K⁻¹ at 32°C. The hardness of MgAlON (13±0.18 GPa) was found higher than MgAl₂O₄ (12-15 GPa) but lower than γ-AlON (~15 GPa). The fracture toughness of MgAlON (2.46±0.30 MPa.m^{0.5}) was higher than MgAl₂O₄ (1.5-2.2 MPa.m^{0.5}) and similar to γ-AlON (~2 MPa.m^{0.5}) [160,175]. The physical properties of AlON seems to be influenced by the simultaneous introduction of Mg in cation sites and N in anion sites. Ma et al. [176] synthesized MgAlON powder at 1600 °C for 2 h via the carbothermal reduction and nitridation method. The obtained MgAlON powder is crystalline and exhibits a spinel structure. It shows high sinterability, with a

bimodal particle size distribution at 0.3 μm and 0.9 μm . The microstructural sintering evolution showed that significant densification occurs at the temperature range of 1600–1700 $^{\circ}\text{C}$, and rapid grain growth appeared at higher temperature (≥ 1750 $^{\circ}\text{C}$). Pressureless sintering with additional holds at the intermediate temperature regions (1650–1700 $^{\circ}\text{C}$) was effective in controlling the microstructure with reduced porosity, which in turn improved the light transmittance. Three samples were prepared at different sintering temperature, shown in **Figure 8d, 8e, and 8f**. A highly transparent MgAlON ceramic was prepared by pressureless sintering at 1700 $^{\circ}\text{C}$ for 2 h and then at 1850 $^{\circ}\text{C}$ for 20 h, which exhibits excellent transmittance from the visible to middle IR regions (82.37 % at 0.60 μm and 86.59 % at 3.70 μm). The Vickers hardness and flexural strength are ~ 13.5 GPa and ~ 246 MPa, respectively.

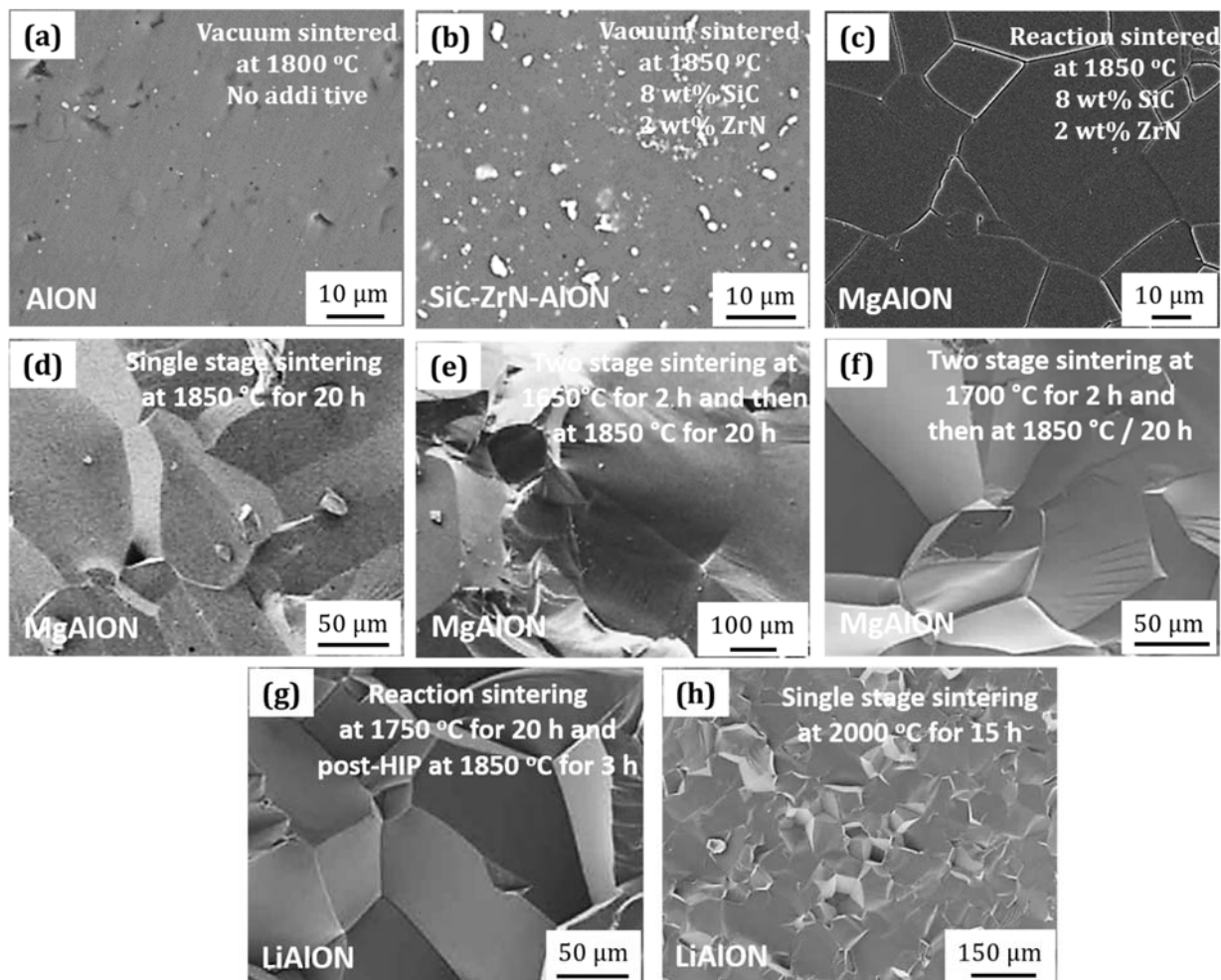


Figure 8: Microstructure of a) pure AlON [174] b) SiC-ZrN-AlON composite [174] c), d), e) MgAlON [175,176], f), and g) LiAlON [177,178]

Highly transparent LiAlON ceramic was successfully manufactured by Zhang et al. [177] via reaction sintering (1750 $^{\circ}\text{C}$, 20 hours) of AlN-Al₂O₃-LiAl₅O₈ composite and post-HIP (1850 $^{\circ}\text{C}$,

3 hours, 180 MPa). Al₂O₃ acts as secondary phase in LiAlON. Transparency of 85.5% at 3.7 μm wavelength was achieved thanks to a complete pore removal (Figure 8g). LiAlON has a potential of high wear resistance, as it exhibits high flexural strength and Vickers hardness (303 MPa and 15.06 GPa, respectively). Clay et al. [178] also fabricated transparent LiAlON by pressureless reaction sintering at sintering temperature 1800 °C and HIPing at 2000 °C at 207 MPa for 2 hours (Figure 8h). In addition, they also show that transparent LiAlON can be obtained by pressureless sintering, without HIPing, if annealed at 2000 °C for 10-15 hours. The hardness of LiAlON obtained with the two processes was 17 GPa with 1 kg load Vickers indent. High optical transmittance and good mechanical properties of LiAlON, along with its comparatively low processing temperature, make it a viable material to compete with MgAlON and AlON. Table 3 shows different mechanical and optical properties of transparent AlON.

Table 3: Mechanical and optical properties of different AlON-based ceramics.

Material	Vickers hardness (GPa)	Flexural Strength (MPa)	Grain size (μm)	Transparency
AlON [179–181]	17	-	-	~80% (at 2.5 to 4 μm)
AlON [174]	13.78±0.21	296±63	~5	-
AlON [28,160]	~15	~310	~200	~80% (2.5-4 μm)
LiAlON [177]	15.06±0.20	303±8	~120	~85.5 % (at 3.7 μm)
LiAlON [178]	16.50±0.50	-	~80-100	~65 % (at 3.3 μm)
MgAlON [176]	13.50±0.15	246±5	100-150	~86.59 (at 3.7 μm)
MgAlON [175]	13.39±0.18	274±5	57.5	~82% (at 0.5 to 4 μm)
SiC-ZrN-AlON [174]	18.19±0.30	418±52	< 5	-

It may be concluded that the presence of second phase reinforcements and a fine grain size can reduce the crack propagation and the wear of the TC. Sintered specimens with porosity below 0.5-1.2% have low wear resistance and provide good tribological behaviour. This can be achieved with the addition of sintering additives at low sintering temperature and high pressure. On the other hand, secondary phases reduce transparency due to scattering.

2.4 Lu₂O₃

In recent years, some researchers have validated a strong interest in the production of Lu₂O₃ TCs of high quality and large size [78,79], and their characterization [182,183], including the tribological characteristics [184]. For characterisation of tribological and mechanical properties,

scratch testing is used to provide the understanding of the surface deformation characteristic and material removal mechanism of hard-brittle materials. Single nanoscratch, repeated nanoscratch, and double nanoscratch experiments of Lu_2O_3 TCs (diameter of 6 mm and a thickness of 1 mm) have been carried out on a nanoindenter [184] using Berkovich indenter's tip radius of about 80 nm. Chemical-mechanical polishing was used to polish the workpiece surface and the polished surface has a roughness of less than 3 nm as determined by atomic force microscopy (AFM). Prediction values for penetration depth in single and repeated nanoscratch tests are very close to experiment observations, as shown in **Figure 9a**.

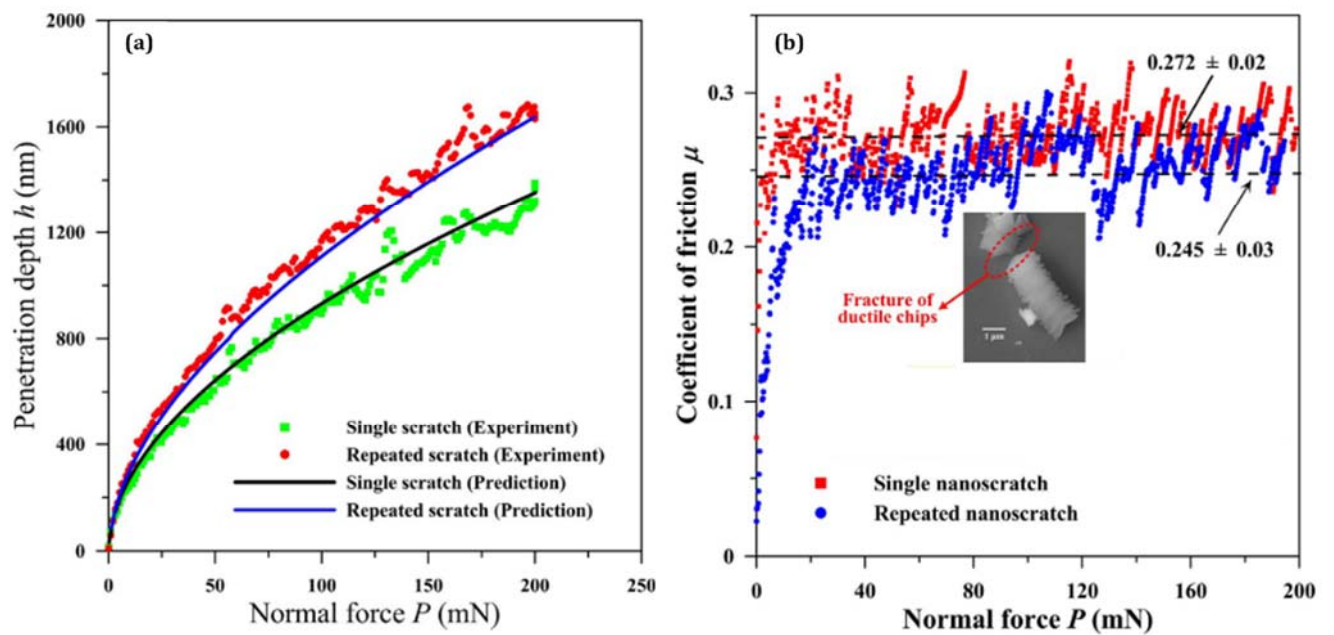


Figure 9: Relationship of a) penetration depth vs. normal force and b) coefficient of friction vs. normal force in single nanoscratch and repeated nanoscratch tests on Lu_2O_3 TCs [184]

The coefficient of friction is generally calculated using normal force and tangential force. The relationships between the friction coefficient and normal force in single nanoscratch and repeated nanoscratch tests are shown in **Figure 9b**. The grain boundary, chip fracture, and plastic flow lines all contribute to the variation of the friction coefficient during the nanoscratch process. In repeated nanoscratch tests, the friction coefficient is lower than in single nanoscratch tests. This can be due to the reason that subsurface damage caused by the first nanoscratch modifying the mechanical characteristics of the material which in turn modify the tribological characteristics. After the first scratch, the residual material transforms into a mixture of polycrystalline nanocrystals and amorphous material, compared to the original micron-size grains. Simultaneously, many defects, including dislocations, stacking faults, nano twins, atomic plane torsion, atomic plane fracture, and atomic plane misalignment, are generated in nanograins during the nanoscratch process. The

mechanical properties of a mixture of polycrystalline and amorphous material compared with many atomic-scale flaws are different from micron-sized grains. These changes in mechanical properties result in a reduction in the friction coefficient with repeated scratching. The friction coefficient increases and then tends to be stable with the increase of the normal force.

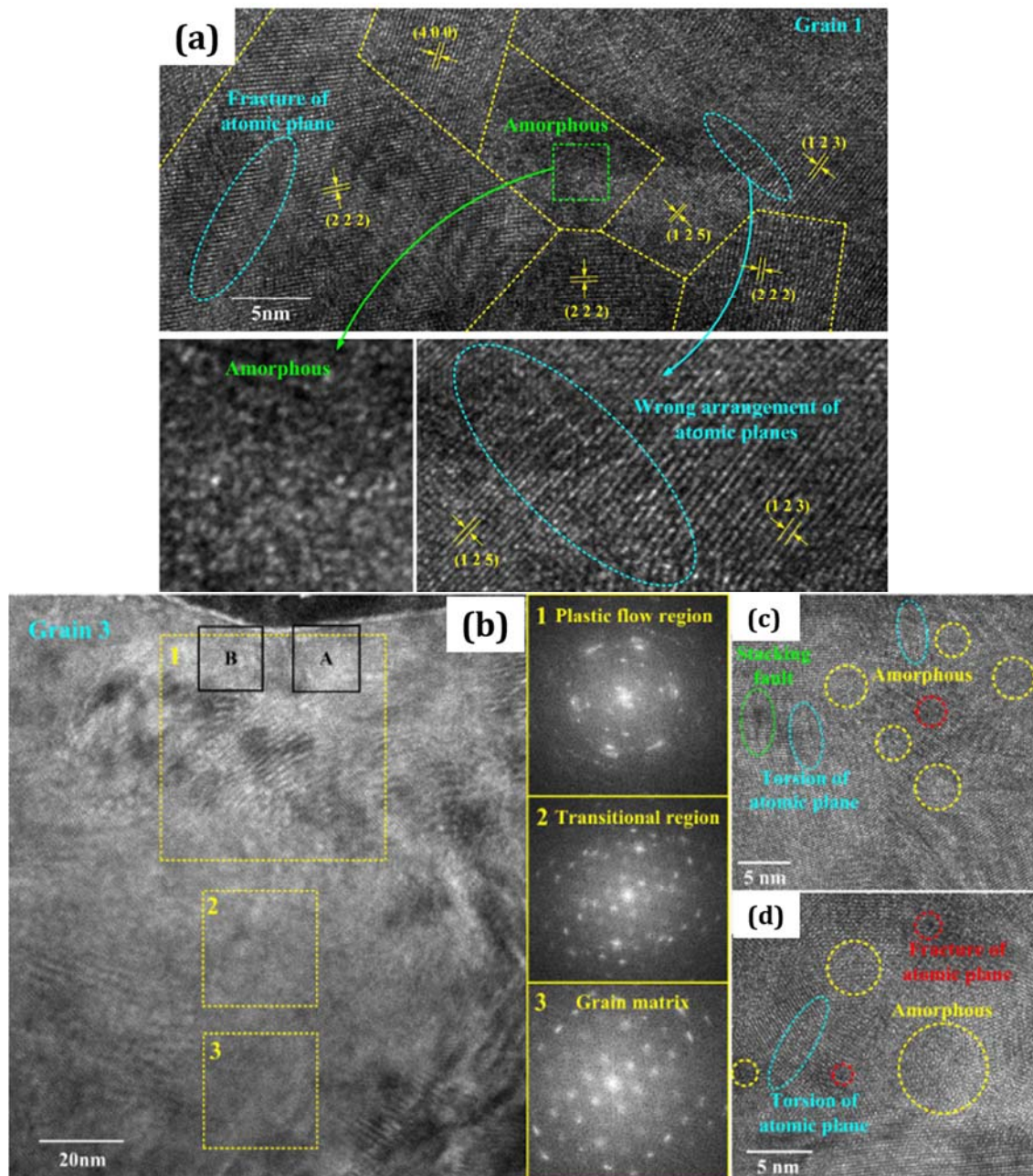


Figure 10: High-resolution transmission electron microscopy of section a) I, and b) II shown in figure 22b. c) and d) represents the types of flaws formed beneath scratch [184].

The tribological behaviour of TCs depends on the load applied during wear. In a scratch test of transparent Lu_2O_3 [184] cracks were not formed under low load conditions, i.e., below 5 mN load. At higher load conditions, median cracks were formed at a deeper depth than the depth of the scratch indenter. It was observed that intergranular fracture was the most common mode of crack

propagation (**Figure 10a**). Additionally, the subsurface has a modest number of transgranular and discontinuous fractures (**Figure 10a and 10b**). Discontinuous cracks at low load (**Figure 10a**) are converted to transgranular load at high load (**Figure 10b**). In TCs, grain boundaries are especially weak and the mismatch degree between neighbouring grains is high [185]. As a result, subsurface fractures spread along grain boundaries in TCs. Lu_2O_3 powder was used for fabricating TC by SPS technique [186]. The pressure and temperature of SPS varied between 20-100 MPa and 1000°C-1600°C, respectively, with soaking time of 5-600 minutes. The microstructures were uniform, with homogeneous equiaxed polyhedral grains, and had few residual pores at the triple junctions. The concentration of pores dropped as the sintering temperature increased from 1300°C to 1500°C and then rose again above 1500°C accompanied by abnormal grain growth. The fracture surface of the TC was intergranular below 1500°C and transgranular above. **Figures 11a, 11b, and 11c** show that an increase in sintering temperature leads to the increase in grain size of the TC, which results in a loss of transparency after attaining the maximum value. The increase in grain size reduces the hardness and fracture toughness value. It, in turn, increases the mass loss tendency upon wear test. **Figure 11d and 11e** show the increase in the grain size of the material when Lu_2O_3 is doped with additives. Ytterbium (Yb) doped Lu_2O_3 TCs fabricated using SPS sintering technique have a smaller grain size than TC fabricated using vacuum sintering (**Figure 11d and 11e**) [187]. **Figure 12** shows the decrease in transparency with the rise in relative density and grain size. The small-sized grain TC is likely to perform well in the tribological application for which an optimum sintering temperature is required [186,187].

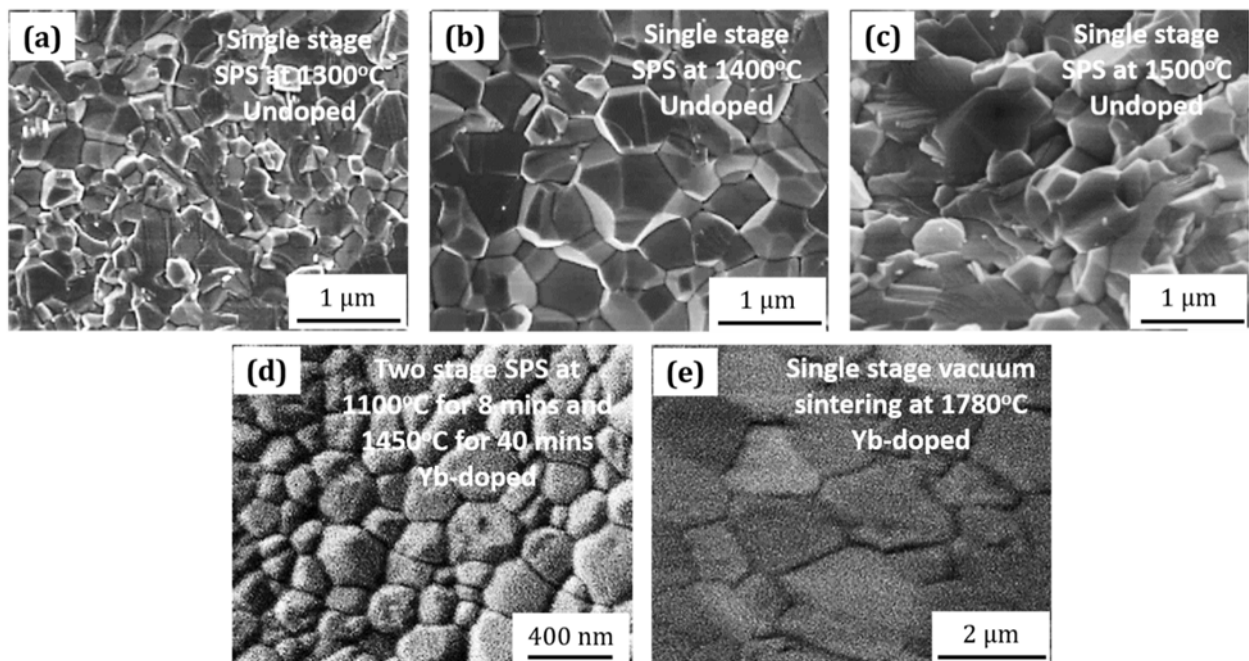


Figure 11: Microstructure of a), b), c) undoped Lu_2O_3 sintered by single stage SPS, d) Yb-doped two stage SPS, and e) Yb-doped two stage vacuum sintering [186,187].

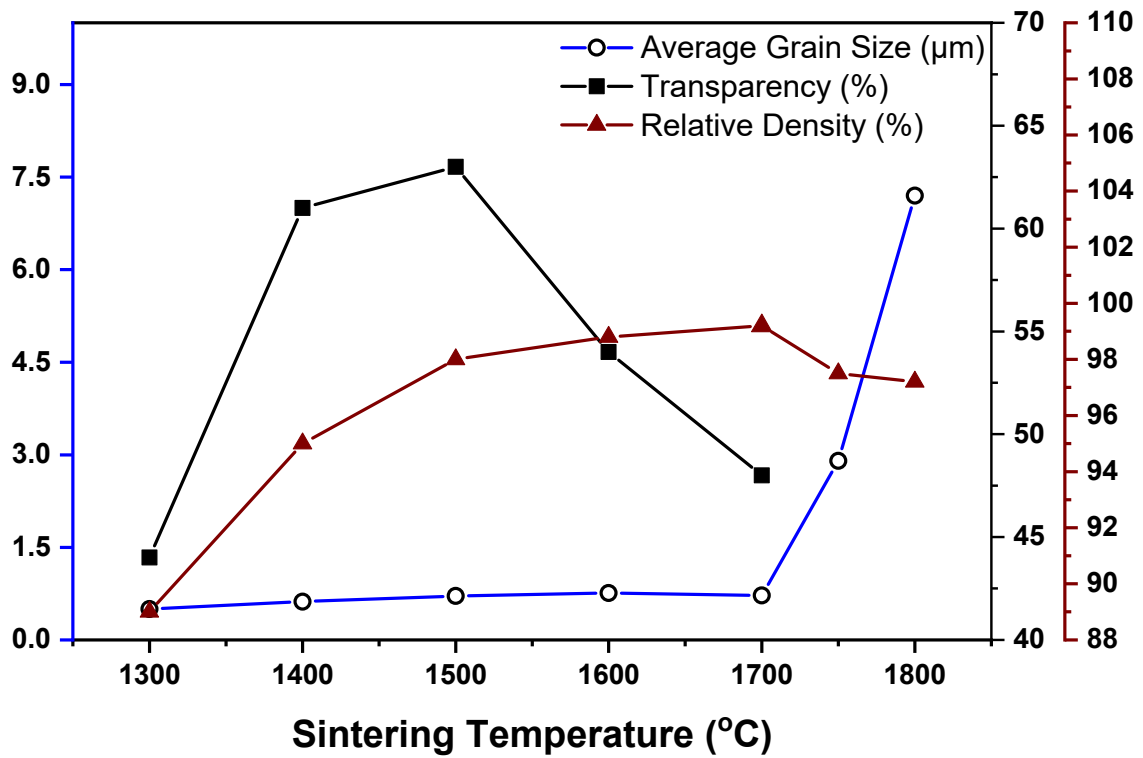


Figure 12: Variation of average grain size (μm), transparency (%), and relative density (%) of transparent Lu_2O_3 without additive as a function of the sintering temperature by SPS [186,187].

It can be concluded from the above discussion that the grain boundary, chip fracture, and plastic flow lines all contribute to the disparity of the wear behaviour during scratching. The wear of TC is a function of porosity. The porosity of the fabricated TC depends on many factors. One out of these factors is sintering temperature. The optimum sintering temperature is desirable for achieving low porosity.

2.5 Y_2O_3

Transparent polycrystalline Y_2O_3 has significant physical and chemical properties, such as low thermal expansion ($8.1 \times 10^{-6} \text{ K}^{-1}$) [188], the refractive index of 1.935 [189], high density (5.031 g/cm^3) [81], high thermal conductivity (13.6 W/m.K at 300 K) [188], a broad transparency range from violet to infrared light (0.2 to 8 μm), and high corrosion resistance. Consequently, Y_2O_3 ceramics are used as promising TCs in various applications, including high-intensity discharge lamps, infrared missile domes, gas nozzles, and heat-resistive windows [81,82]. Liu et al. [113] fabricated high-strength transparent Y_2O_3 ceramics using the SPS technique by optimizing the heating rate. The heating rate substantially affects the microstructure of transparent Y_2O_3 , which affects the optical/mechanical characteristics of TCs due to reduced grain growth with the rise in

heating rate. SPS has effectively synthesized dense Y_2O_3 materials at lower sintering temperatures, 1100-1300°C and shorter sintering times [94,190,191]. As in the case of Lu_2O_3 , the final microstructure depends strongly on the sintering process used, and SPS offers a faster treatment at a lower temperature in comparison with vacuum sintering [192], leading thus to a finer grain size.

Numerous articles have been published on the production of transparent Y_2O_3 ceramics using pressureless sintering in vacuum or in an H_2 environment [193–196]. Densification was facilitated with decreased particle size of the powder. Jin et al. [194] reported on a vacuum sintering technique for fabricating transparent Y_2O_3 ceramics using ZrO_2 doping, with varying ZrO_2 concentrations after 8 hours of sintering at 1860°C. The starting Y_2O_3 powder had an average particle size of 2 μm , which was decreased to approximately 0.34 μm after 12 hours of ball milling in ethanol. The optimal concentration of ZrO_2 was found to be 5 mol% in terms of densification and reduced grain size. The good tribological properties of Y_2O_3 ceramics may be explained by their improved densification and inhibited grain development characteristics caused by the presence of ZrO_2 . **Figure 13a-13d** shows SEM images of samples sintered at 1860°C for 8 h. No pore was seen in the sample doped with 5 mol% ZrO_2 . This reduction in porosity will provide better wear resisting properties to the TC. To increase the density of TCs with high transmittance, transparent Y_2O_3 ceramics are also fabricated using vacuum and air sintering in combination with HIPing [197]. The results show that sintering in air in combination with HIPing is similar to sintering in vacuum and HIPing for the preparation of transparent Y_2O_3 ceramics. The density of the resulting air-sintered ceramics is limited to about 98–99%. HIPing is required to take the ceramics to full density. Nanophase Y_2O_3 powder can simply be processed into green bodies with high densities. **Figure 13e** represents SEM image of sintered and etched transparent Y_2O_3 . The nanophase Y_2O_3 powder was dry-pressed in a stainless steel die under 632 MPa for 30 minutes to prepare 2 mm thick green body. The green body was then sintered at 1600°C for 2 hours in air. The resulting translucent ceramic of relative density of about 99.4% was polished to gain 61% transparent Y_2O_3 .

Recently, nanocrystalline Y_2O_3 ceramics were prepared [57] with very fine grains (20 nm) and good mechanical properties (hardness 10.5 GPa, fracture toughness 2.21 $Mpa\ m^{1/2}$), although the production method required very high pressure (5 GPa). Y_2O_3 -MgO nanocomposites transparent in the near-infrared light have been also produced using hot pressing [198,199] and SPS [132]. The production of transparent nanocomposites is a particularly interesting concept, as while the combination of phases with different refractive index generally does not allow reaching

transparency, the scattering is limited when the grain size is significantly reduced below the wavelength of light. At the same time, such approach offers a lot of space for the tuning of effective material properties. Furthermore, Y_2O_3 nanopowder was also used a starting material to produce transparent Y_2O_3 ceramic by SPS at 1200 °C to 1600°C for 20 minutes under the pressure of 100 Mpa [200]. It was observed that an optimum sintering temperature is required for obtaining good mechanical properties while maintaining good transmittance value.

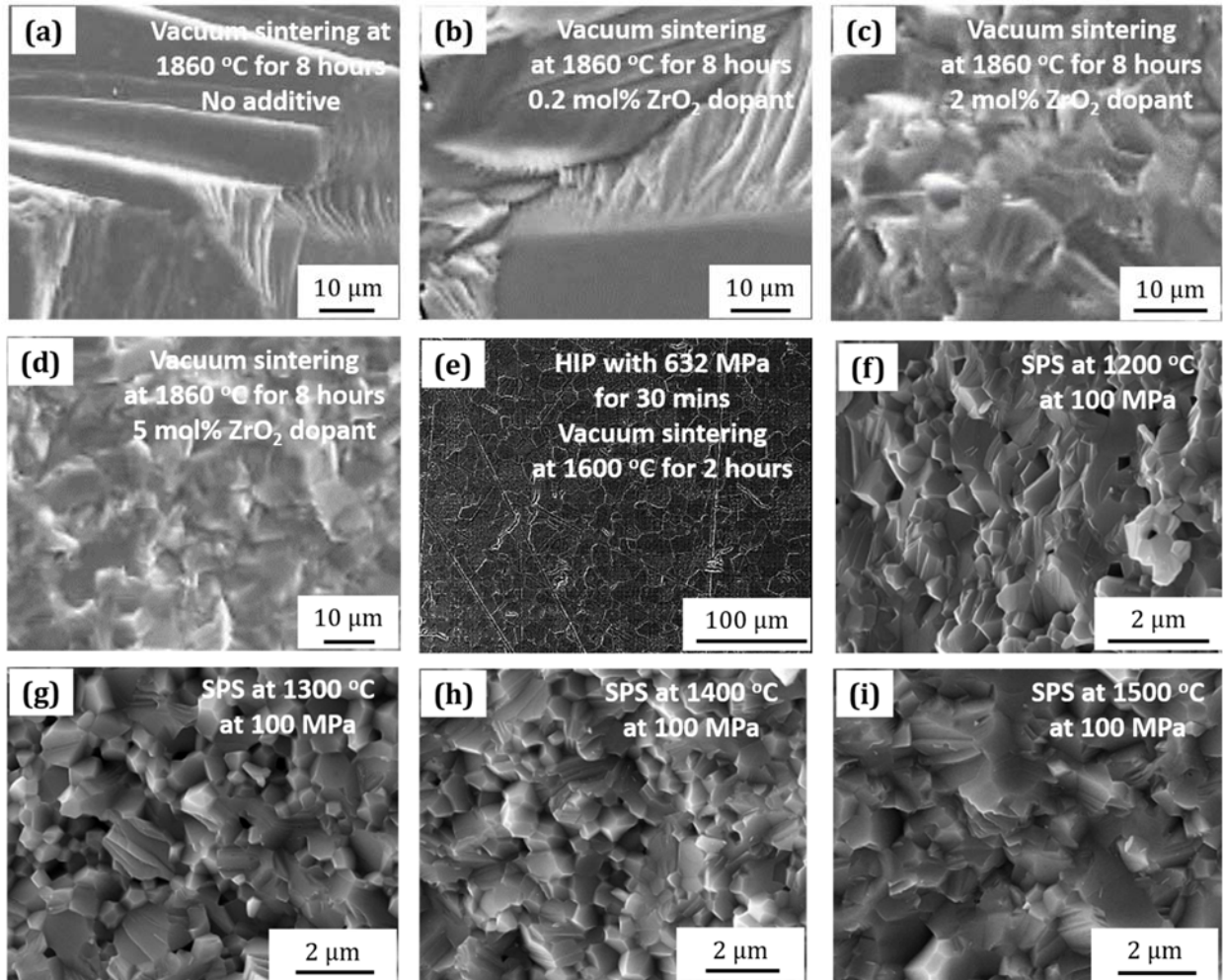


Figure 13: Micrographs of transparent Y_2O_3 obtained a) via vacuum sintering without additive [194] b), c), d) via vacuum sintering with 0.2 mol%, 2 mol% and 5 mol% ZrO_2 dopant [194] e) via HIP followed by vacuum sintering [197], f), g), h) and i) via SPS at different temperatures [200].

Table 4: Mechanical and optical properties of different Y_2O_3 TCs.

Material	Vickers hardness (GPa)	Fracture Toughness ($MPa \cdot m^{0.5}$)	Grain size (μm)	Transparency (%)
Y_2O_3 [197]	7.41-7.67	-	21.5 ± 11.1	61 at 1000 nm
Y_2O_3 [200]	6.87-7.60	1.99-2.06	0.58 ± 0.11	54 at 800 nm
Y_2O_3 [57]	10.4-10.5	2.20-2.21	~ 0.02	81.3 at 1100 nm
Er: Y_2O_3 [201]	7.23 ± 0.35	0.81 ± 0.07	~ 328	32 at 2000 nm
Er: Y_2O_3 [201]	9.09 ± 0.41	1.39 ± 0.07	~ 0.34	81 % at 2000 nm

The micrographs of fracture surface of sintered samples obtained at different temperatures are shown in **Figure 13f-13i**. The hardness of the TC increased from 6.87 to 7.60 GPa and flexural strength increased from 75 MPa to 122 MPa with increase in the sintering temperature up to 1500°C due to relative density improvement and decreased with further rise in temperature. However, the fracture toughness did not show the same trend and decreased with rise in the temperature due to the reduction in the porosity. The change in mechanical properties of the TC may improve the tribological properties and need to be further investigated. **Table 4** collects the mechanical and optical properties of different transparent Y₂O₃ ceramics available in the open literature. The hardness of transparent Y₂O₃ increases with increasing heating rate and follows the Hall–Petch relationship, i.e., with grain size reduction [113]. On the other hand, the toughness is less susceptible to heating and grain size and takes on a comparable value. Therefore, the influence of heating rate on wear resistance and coefficient of friction of material requires further research.

However, it should also be kept in mind that the fracture toughness of transparent Y₂O₃ is relatively low compared to other transparent ceramics, affecting the tribological behavior. Most research has been done on TC's densification and microstructure. There is no systematic research on the correlation between the change in the microstructure of transparent Y₂O₃ and the mechanical characteristics, which improves the wear resistance of materials.

2.6 Cubic boron nitride, cBN

In comparison to cubic boron nitride (cBN) single crystals, polycrystalline cBN (PcBN) sintered bodies have better mechanical and tribological characteristics. PcBN was subjected to high pressure (20 GPa) and temperature (1500 °C), resulting in nanostructures with a grain size of 20 nm and hardness of 85 GPa. The Hall Petch effect, in which the mobility of dislocations is effectively inhibited, is responsible for the increase in hardness of nanostructured PcBN to about 50-70% [202]. As a consequence of the high hardness value, there may be a high wear resistance associated with it. A high wear resistance may be expected considering the high hardness. Tian [109] first incorporated nano twins into nanostructured PcBN produced from onion-like Boron Nitride (oBN), which led to an increase in hardness to 100 GPa. Grains were equiaxed of the same size but irregular in shape. However, there is still debate regarding this outcome[203]. Conversely, the above-mentioned manufactured superhard PcBN exhibits transparent properties with a maximum transmittance ranging from 20% to 40% at 400–800 nm [110].

Taniguchi et al. [80] developed bulk single-crystal cBN that was colorless and had worthy transmission by utilizing $Ba_3B_2N_4$ as solvents. Researchers [108–110] used hexagonal BN (hBN) or organic BN (oBN) as a starting material for the production of superhard cBN blocks without any further additives or modifications. The fabrication requires very high sintering pressure and temperature, which modifies the phase from hBN/oBN to cBN, leading to optical transparency. For manufacturing transparent ultra-hard polycrystalline cBN with a grain size of 200 nm, a two-stage multi-anvil cell pressing was utilized in conjunction with pressures as high as 14 GPa and temperatures ranging from 1300–2000°C. Translucent polycrystalline cBN was obtained with a maximum hardness of about 69 GPa, which is almost two times harder than single-crystal [204]. cBN powders of different sizes were sintered at pressure 7.7 GPa and temperatures varying from 1500 to 2500°C [205]. It was observed that the transparency of the materials decreases if the powders is sintered between 2000 to 2500°C. The fracture mechanism for transparent cBN changed from intergranular to transgranular when the sintering temperature was increased during the fabrication of TC. The performance of the materials changed also with the initial particle size. The performance of the materials changed also with the initial particle size.

Figure 14a, 14b, and 14c represent the variation of relative density, hardness, and fracture toughness as a function of the sintering temperature of transparent cBN with an initial particle size of 0.5-1.2, 2-4, and 8-12 μm , respectively. It depicts that with an increase in sintering temperature, the relative density increases. The value of hardness and fracture toughness of the TC first increased with an increase in particle size from 0.5-1.2 to 2-4 μm , and then decreased with a further increase in particle size from 2-4 to 8-12 μm . So, the optimum size of initial particle size is between 1-2 μm for maximum hardness and fracture toughness. Hence, the particle size affects the tribological behavior of TC as wear resistance of the sintered sample possibly increases with the increase in hardness and fracture toughness. The maximum hardness value was obtained at sintering temperature around 2350°C for all inial particle sizes. However, the maximum fracture toughness was received for 0.5-1.2 μm , 2-4 μm , and 8-12 μm at around 2200°C, 2000°C, and 2400°C, respectively.

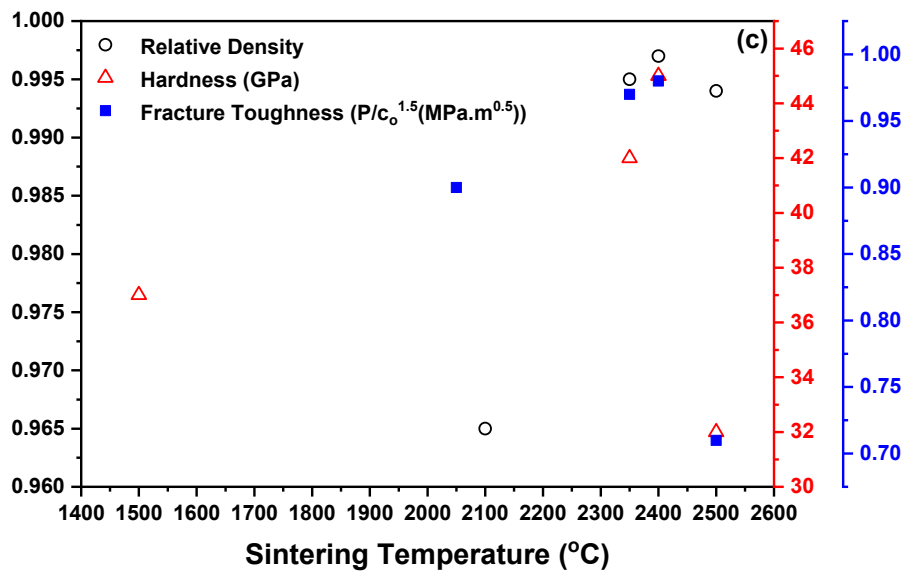
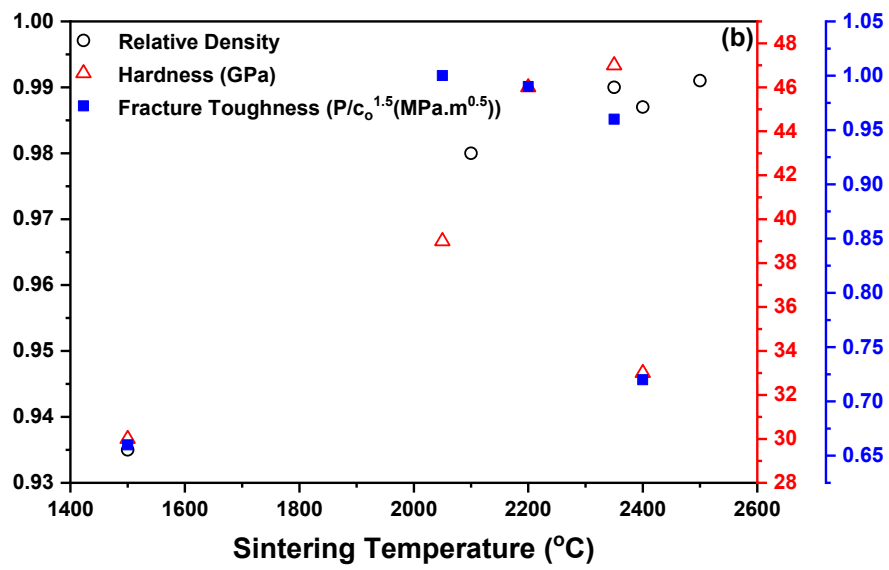
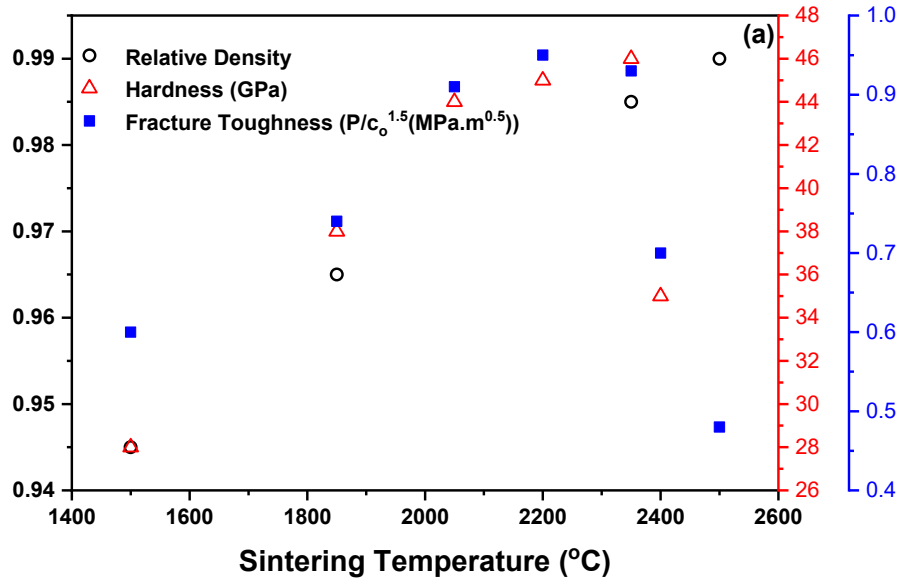


Figure 14: Relative density, hardness, and fracture toughness vs. sintering temperature of cBN with initial particle size a) 0.5-1.2 μm b) 2-4 μm, and c) 8-12 μm [205]

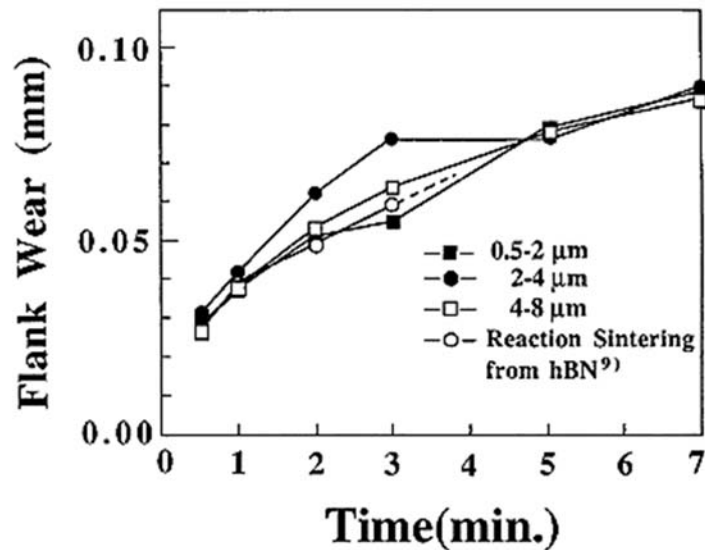


Figure 15: Flank wear versus cutting time of different samples made by cBN [205].

Wear resistance is an essential characteristic for the use of sintered transparent cBN. To understand the wear behaviour of cBN, the machine tool made of cBN synthesized by reaction sintering were compared to other sintered tools made by vacuum sintering method. The degree of wear in the cutting edge of the manufactured cutting tools is represented by the flank wear. **Figure 15** depicts the relation between the amount of flank wear and the cutting time of the test specimens made of different initial particle size and the relationship between the amount of flank wear and the cutting time of the sample produced by reaction sintering. Four specimen at different sintering conditions were fabricated, i.e., specimen of initial particle size of 0.5–2 μm and 2–4 μm: sintered at 2050°C and 7.7 GPa, specimen of initial particle size of 4–8 μm: sintered at 2350°C and 7.7 GPa, and specimen obtained by reaction sintering method: synthesized at 7.7 GPa and 2150°C. Machining conditions were cutting speed of 10 m/min, depth of cut 0.2 mm, and feed/rev of 0.1 mm/rev with no coolant on work material WC-24 wt.% Co alloy. According to the research findings, there was no noticeable difference between any test specimens in terms of wear characteristics. There was a significant overlap between the wear resistance of test specimens and that produced by the reaction-sintering technique. According to Hooper and Brookes [206], the high value of hardness is associated with the higher fraction of cBN aggregate material. It is due to the deformed cBN skeletal structure produced during the synthesis process. SEM and TEM studies of the grain and microstructure of transparent polycrystalline cBN have shown that both the Hall–Petch effect and microscopic flaws contribute to the enhanced hardness and wear resistance of the TC. It can be concluded that an optimal size of initial particle is required to develop TC with the hardness and fracture toughness needed for tribological application. The production of equiaxed grains resist the mobility of dislocations which is desired for high wear resisting TCs.

2.7 SiAlON and Si₃N₄

SiAlON ceramics are solid solutions of silicon nitride (Si₃N₄) containing variable amounts of additional aluminum (Al) and oxygen (O). High strength over extensive high temperatures, high thermal shock resistance, and relatively high chemical stability of SiAlON ceramics place them amongst other important engineering ceramics. Advanced sintering technologies have been used to fabricate translucent and even transparent SiAlON ceramics, demonstrating their potential as engineering ceramics [101,207]. SiAlON is structurally identical to Si₃N₄, except that Al and O, respectively, have replaced the Si and N of Si₃N₄. Sintering of Si₃N₄ powder with AlN-Al₂O₃-MO_x and AlN-MO_x systems, where M denotes Li, Mg, Ca, Y, and rare earth elements, can produce SiAlON ceramics (excluding La, Ce, Pr, and Eu) which are transparent and suitable for tribological applications. The translucent α -SiAlON ceramics stabilized with metal cations, such as Nd³⁺, Y³⁺, Gd³⁺, Dy³⁺, Yb³⁺, Lu³⁺, etc. have been developed with high transmittance in the infrared region [84–86].

Silicon Nitride (Si₃N₄) is an extensively used ceramic material with numerous industrial applications. Atoms of silicon and nitrogen of Si₃N₄ have strong covalent bonds and hence, it exhibits poor atomic mobility and high resistance to deformation. Usually, two polymorphs of Si₃N₄ (α and β), having silicon atoms tetrahedrally coordinated by nitrogen atoms, exist at wide temperature range: a low-temperature α -Si₃N₄ whereas and high-temperature β -Si₃N₄. A third polymorph (γ -Si₃N₄) was obtained at high pressure (~13 GPa). It has a cubic structure with two-thirds of silicon atoms octahedrally placed and one-third of silicon atoms tetragonally placed. It has a very high density and closer atomic packing and good transparency in the visible range. However, so far the production of larger bodies was not demonstrated Si₃N₄ is one of the most successful ceramic materials for spacecraft applications [208,209] because of its mechanical strength and good wear resistance in harsh environments that include constant rain and extreme thermal shock [210,211]. In addition, the bending strength and hardness of 100 % dense pure Si₃N₄ developed without additives are almost temperature independent from room temperature to 1500 °C [212]. It makes Si₃N₄ an appealing material for high-temperature tribological applications [213]. Si₃N₄ exhibits properties such as high flexural strength, good wear resistance, corrosive resistance, fracture resistance, creep resistance, and high hardness. The optical properties of Si₃N₄ are of enormous interest over decades [214]. Si₃N₄ can be transparent in the IR range, but the transparency in the visible range is usually limited. Many researchers have developed transparent Si₃N₄ by different techniques with appreciable transparency and improved mechanical and tribological properties. Some researchers have recently shown an interest in preparing translucent

ceramics [86,215–219]. Pechenik et al. [220] used a laser-driven gas-phase reaction between silane and ammonia, followed by diamond cell pressing at 100 GPa and sintering at 1000-1400°C, to create translucent Si₃N₄.

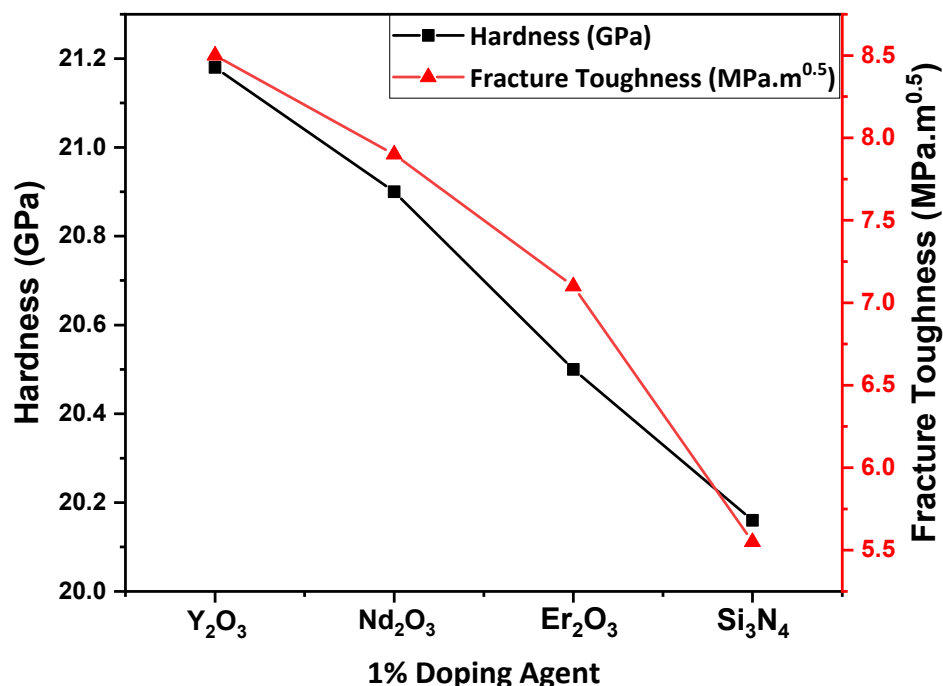


Figure 16: Doping agent vs. Hardness and Fracture Toughness in Si₃N₄.

Doping agents in Si₃N₄ ceramics affect sliding wear characteristics. Joshi et al. [65] used Y₂O₃, Er₂O₃, and Nd₂O₃ doping agents and developed transparent Si₃N₄ ceramics with 3 wt.% MgO, 9 wt.% AlN, 87 wt.% α-Si₃N₄ and 1% doping agent by hot press technique with a sintering temperature of 1850 °C and a pressure of 30 MPa. The addition of a 1wt.% doping agent increases hardness and fracture toughness, as shown in **Figure 16**. Y₂O₃ results out to be one of the most successful doping agents in increasing the hardness and fracture toughness and reducing friction and wear of Si₃N₄, thus improving its tribological behavior. This increase in the mechanical properties can reduce the wear of Si₃N₄ at room and elevated temperatures and enhance tribological behavior [61,62]. Translucent single-phase Li-α-SiAlON ceramics were successfully developed using SPS at a heating rate of 100 °Cmin⁻¹ for 5 minutes at 1750 °C. The results indicate that SPS significantly retards the volatilization of Li₂O due to the quick consolidation process. Within a few minutes, Li-α-SiAlON densification is efficiently accelerated. The resulting sample exhibited a reasonably high infrared transmittance of 57% at 1.4 μm, which may be attributed to the dense, homogeneous, and equiaxed-grain microstructure with low amount of intergranular glassy phase. The density, hardness, and fracture toughness of the sintered sample were 3.12 gm⁻³, 20.1±0.2 GPa, and 3.0±0.1 MPa.m^{0.5}, respectively. These improved mechanical properties show that Li-α-sialon has the potential to be used as a high wear resistance TC [217].

fabrication of transparent Si_3N_4 , $\alpha\text{-Si}_3\text{N}_4$ transforms to $\beta\text{-Si}_3\text{N}_4$, lower tribological properties are achieved along with low transparency. To enhance the formation of the α phase of the material and suppress that of the β phase, MgO-AlN spinel was used as a sintering additive, reducing the material fracture toughness [221]. To enhance the material fracture toughness, h-BN was used as the sintering additive [90], as it resists the crack propagation by forming a composite material. The wear volume decreased due to the reduced grain pull-out of h-BN and $\beta\text{-Si}_3\text{N}_4$ and the lubrication properties of $\alpha\text{-Si}_3\text{N}_4$.

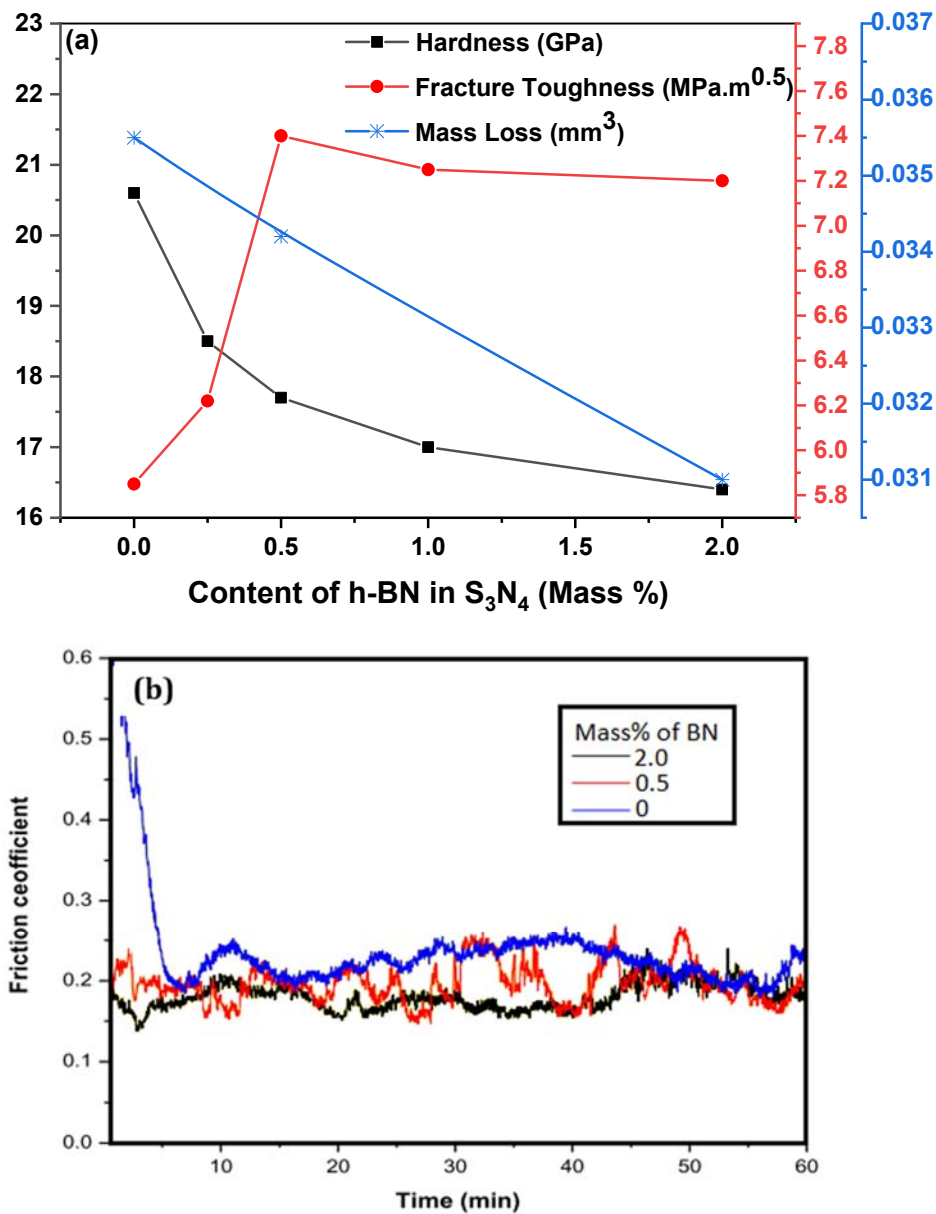


Figure 17: Variation of a) hardness, fracture toughness, wear volume, and b) friction coefficient with different h-BN content [100].

Tribological properties, like wear volume and coefficient of friction, decreased with an increase in h-BN content (0 mass % to 2 mass %), as shown in **Figure 17a and 17b**, respectively [100].

The addition of h-BN to Si₃N₄ improved the fracture toughness but reduced the hardness of the transparent ceramic. The fracture toughness of this TC first increased and then slightly decreased with the increase in amount of h-BN to Si₃N₄. Joshi et al. [37] examined the hot-pressed samples of the mixture of α -Si₃N₄, AlN, MgO, and h-BN sintered at 1850°C and 30 MPa, respectively. It was observed that h-BN was dispersed in β -Si₃N₄ after sintering. With the increase in the sintering aid, i.e., h-BN (0.25 to 2 wt%), the density, flexural strength, hardness, and transparency of the material decreased, while the wear resistance and fracture toughness of the TCs was enhanced. With the addition of h-BN, density of the material decreases due to porosity, compromising also transparency. But the fracture toughness of the material with BN content is higher than that without BN content due to the resistance to crack propagation provided by BN content. Also, the fracture toughness increases after adding a small amount (0.25 to 2 wt%) of BN to Si₃N₄. Conversely further addition of BN content showed no further improvement of fracture toughness [37].

Many researchers recommended the fabrication of fine grain-sized α -Si₃N₄ TC as it increases the density of the material. High density and small grain sizes TC provide good tribological properties. Su et al. [101] also commented that α -Si₃N₄ has high optical transmission in visible and IR regions. Besides, the addition of Dy₂O₃, AlN, and Al₂O₃ in α -Si₃N₄ exhibited high hardness and high fracture toughness. Yang et al. [222] examined the effect of mixing different amounts of AlN-MgO, AlN-Y₂O₃, and Al₂O₃-Y₂O₃ systems in Si₃N₄ and observed that the addition of a low amount of sintering aids to Si₃N₄ leads to the formation of β -Si₃N₄, increases the transparency and leads to fine structure, which was opposite to previous results. It can be concluded that transparent Si₃N₄ exhibits different tribological properties and transparency by varying the amount of sintering additives. Transparent Si₃N₄ is one of the best transparent materials that can be used for high temperature tribological applications due to its high temperature metastability.

3. Effect of microstructure and mechanical properties

Microstructure (such as pores, grain size, and grain boundaries) of TCs affects their fracture toughness and hardness. In response to the change in the mechanical properties of the TCs then affects the tribological performance of the material [73,223,224]. It was revealed that TCs have a higher hardness and lower mass loss compared to all types of glasses and hence higher wear resistance. It is evident that TCs also show brittle fracture as dominant wear mechanism. To calculate sliding wear in the tribocontact of brittle materials in the absence of any layer development, a sharp indenter model and a blunt indenter model were presented. According to Marshall et al. [225], wear in brittle materials occurs as a consequence of the development and

propagation of lateral cracks. For a given applied load (P), total sliding distance (S), hardness (H), fracture toughness (K_{Ic}) and elastic modulus (E), wear volume of the brittle solid (V_1) can be assessed using the following equation:

$$V_1 = \alpha \frac{P^{9/8}}{K_{Ic}^{1/2} H^{5/8}} \left(\frac{E}{H}\right)^{4/5} S \quad (1)$$

where α is a material constant. When a blunt indenter is placed against a brittle solid, surface ring cracks are created. These cracks spread downward with repeated sliding contact and eventually develop into conical cracks, resulting in material pull-out [226]. With a big data set of wear data, another method for examining wear across materials and operating situations is to study correlational models against crucial material and operational characteristics [227,228]. The basic mechanism of wear in an ideal contact model based on our current knowledge. Wear may be regarded as simple asperity-scale abrasion in the mild regime. In this situation, the product of the wear depth, contact breadth, and length of sliding within each "sliding cycle" may be used to estimate the wear caused by each asperity contact, as shown in **Figure 18a**. The "sliding cycle" is defined as the entire slide distance l divided by the Hertzian contact width $2a$, i.e., $l/2a$. With these assumptions, mild wear may be represented as follows:

$$\text{Wear Volume} \propto \frac{P_m N}{H_v E} f(\text{roughness parameter}) \times l \quad (2)$$

where P_m denotes the mean Hertzian pressure, H_v denotes the hardness, N is the load, E the composite Young's modulus and f may be considered as a constant in this analysis. Thus, mild wear was proportional to $P_m \times N \times l$, which was correlated to the operating parameters, and inversely proportional to the material characteristics, H_v and E' . Due to the existence of fractures, edge effects from those cracks, and third-body wear particles in the severe wear regime, the asperity contacts might exhibit different properties, as demonstrated in **Figure 18b**. The entire volume of wear may be stated as follows:

$$\text{Wear Volume} \propto \frac{\sigma_{\max}(T^*/T_o) \sqrt{d_{50}}}{K_{Ic}} \frac{N}{H_v(T^*)} l \quad (3)$$

where T^* is the nominal contact's interfacial temperature [229], T_o is the ambient temperature set to 20 °C, K_{Ic} is the fracture toughness, d_{50} is the mean grain size, and σ_{\max} is the maximum tensile stress. Archard's temperature equation [230] is used to compute the interfacial temperature (T) rise due to friction.

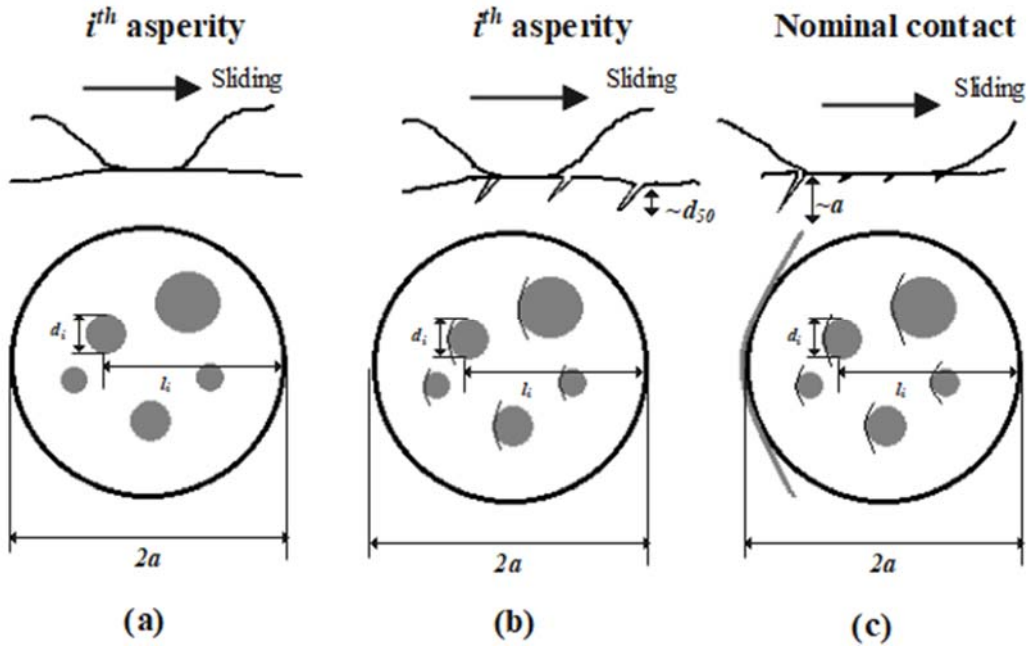


Figure 18: Modeling wear in different wear regimes. (a) Asperity-scale abrasion in mild wear regime, (b) tensile cracks inside the nominal contact in severe wear regime, and (c) gross fracture in the nominal contact in ultra-severe wear regime [228]

Thermal shock may be attributable to a temperature gradient between the hot patch and the surrounding low temperature region under an extremely severe wear regime. Because the interfacial temperature occurs in a layer with a thickness of half the Hertzian width, the wear equation in Eq. (3) is expanded by substituting a for the d_{50} term; that is, the crack length that affects the stress intensity is equal to a , as shown in **Figure 18c**. This results in the following equation:

$$\text{Wear Volume} \propto \frac{\sigma_{\max}(T^*/T_0)\sqrt{a}}{K_{1c}} \frac{N}{H_v(T^*)} l \quad (4)$$

where cone crack length, a , is given as:

$$a = \left(\frac{\chi P}{K_c}\right)^{2/3} \quad (5)$$

Increased (T/T_0) ratio and fracture length in combination with a drop in $H_v(T^*)$ should result in a much greater amount of wear compared to corresponding to the extreme wear stated in Eq. (3).

The scratch wear test provides evidence that TCs have higher wear resistance properties than all glasses [66]. Si_3N_4 has superior mechanical and tribological properties compared to glasses and can be used in applications like armor, missiles domes, and laser windows for elevated temperatures [231]. However, Si_3N_4 is generally not transparent in the visible range. However, altering the microstructure of transparent Si_3N_4 improves the transparency and mechanical properties of the material. Joshi et al. [36] produced Si_3N_4 transparent in the IR and translucent in

the visible region using hot pressing and the addition of h-BN. A small amount of h-BN led to a good densification, but as the h-BN content increased, the performance deteriorated and a higher porosity was observed. It was also found that the presence of inclusions of α - Si_3N_4 and AlN increased the hardness of the material. During the fabrication of transparent Si_3N_4 with γ -phase at high pressure (13 GPa) and high temperature (1800°C), the α -phase and β -phase of Si_3N_4 change to γ -phase [44]. The average grain size of γ - Si_3N_4 was 143 nm. The hardness and fracture toughness of TC were 34.9 GPa and $3.5 \text{ MPa}\cdot\text{m}^{1/2}$, respectively. Similar observations have been reported for other TCs [35,37,38]. High-density transparent MgAl_2O_4 with fine grain size exhibits high hardness but low fracture toughness [35].

~~Also, the TCs fabricated at low sintering temperatures achieve high density with maximum transmittance and hardness value.~~ To improve the transparency of Al_2O_3 , a reduction in grain size is the most promising approach [23,45,163]. In the case of Al_2O_3 , an increase in sintering temperature results in grain growth which causes birefringence and reduces transparency [DOI: 10.1016/j.jeurceramsoc.2020.10.025]. The grain refinement of transparent ceramics is required to improve the mechanical behavior, which further enhances the tribological performance of TCs. Therefore, optimum grain size is needed for a combination of good tribological behavior of TCs with good transparency. The reduction of porosity level in TCs improves the mechanical properties and transparency of the materials, leading to a further improvement of their tribological behavior. It is important to note that the impact of even a small amount of porosity is much stronger on the optical quality than on the mechanical properties .

Recent investigations show that the SPS is one of the best techniques to fabricate TCs as it produces small grain structures at low sintering temperatures [55,56]. Alumina ceramics with a transparency of 65.4 % and an average grain size of 200 nm were produced using high-pressure (> 400 MPa) SPS [64,67]. Nishiyama et al. [63] also developed transparent Al_2O_3 ceramics with nanocrystalline grains employing high pressure (7.7 GPa) and low temperature (800°C) SPS method. The resulting samples had a mean grain size of 0.15 μm , with a maximum in-line transmission of 71% at 640 nm for 0.8-mm thick samples. More notably, the transparent Al_2O_3 ceramics exhibited excellent mechanical properties, with average microhardness and fracture toughness of 25.5 GPa and $2.9 \text{ MPa}\cdot\text{m}^{1/2}$, respectively. So, it can be concluded that TC can be fabricated by SPS can improve the tribological behavior.

Using HIP and a vacuum-pressure slip-casting method, Mizuta et al. [52] produced fine-grained transparent Al_2O_3 ceramics with a transparency up to 46% and bend strength of 600–800 MPa.

Pre-sintering at 1240°C for 2 hours, with heating and cooling rates of 40°C/min and 5°C/min, was done followed by HIP sintering at 1050–1400°C for 1 hour at 150 MPa, i.e., 30 °C/min to 500 °C, 20 °C/min to 1050°C, and 10 °C/min to the ultimate sintering temperature. During HIP, the pressure raised at a rate of 3.4 MPa/min above 500°C. After sintering at 1350°C, samples reached a maximum transparency of 46%. Grasso et al. [64] also fabricated transparent Al₂O₃ with a grain size of 107 nm and a transparency of 65.4%. This fine structure of TC should provide high mechanical strength and good tribological properties [52]. To better control the grain size of transparent Al₂O₃, dopants like 0.3% zirconia and 0.175% MgAl₂O₄ were used by Trunec et al. [53], which increased the transparency by 7-12%. SPS and self doping techniques were also used to manipulate the grain size of the TC, which affect the mechanical and tribological behavior of the material. Zheng et al. [129] fabricated transparent MgAlON with an approximate grain size of 10 μm by vacuum sintering and HIP. Optically transparent MgAlON can be obtained by reactive sintering of a MgO, AlN, and Al₂O₃ powder mixture at 1650°C for 15 hours. The fabricated TC yield 40% increase in the mechanical strength due to the Hall Patch effect and twin lamella strengthening mechanism. Therefore, it can be considered a promising candidate material for tribological applications. Zheng et al. [177] also developed transparent LiAlON with no porosity by reactive sintering at 1750°C for 20 hours of powders AlN, Al₂O₃, and LiAl₅O₈, which eliminated Al₂O₃ secondary phase and porosity to obtain TC with maximum transparency of 85.5%. The hardness and flexural strength of developed TC were 15 GPa and 303 MPa, which may provide good wear resistance to the material. The tribological performance of transparent MgAl₂O₄ fabricated by SPS at 73 MPa with different sintering temperatures shows that the friction coefficient and mass loss increase with an increase in sintering temperature [35]. The variation in the mass loss during the wear experiment of transparent spinel with the deviation of hardness and fracture toughness is depicted in **Figure 6**. High hardness and low fracture toughness achieved at low sintering temperature were suitable for low mass loss during wear. Fracture toughness is highly affected by the microstructure of materials. It may be enhanced by encouraging strengthening processes such as grain bridging, which absorbs some of the energy required to propagate fractures.

Lopez et al. [54] also showed that the hardness of TCs increases with decreasing the grain size whereas, the fracture toughness remains the same with the decrease in grain size. The lubricated sliding wear of three transparent MgAl₂O₄ spinel materials with various grain sizes designated as Nano (345nm), Fine (2.1μm), and Coarse (15 μm) has been studied. Fine MgAl₂O₄ has traditional wear behavior, including mild wear, followed by a rapid shift to severe fracture-controlled wear.

A significant grain pull-out was observed on worn surfaces of Fine MgAl_2O_4 , which is compatible with the intergranular mechanism of fracture. Compared to Fine MgAl_2O_4 , Nano and Coarse MgAl_2O_4 both demonstrate a progressive transition from moderate to severe wear and have substantially lower overall wear rates. Both Nano and Coarse MgAl_2O_4 have worn surfaces that show transgranular fracture and material loss, similar to lateral-crack driven chipping. Stronger grain boundaries in Nano MgAl_2O_4 can be ascribed to the Y_2O_3 sintering additive employed for grain refining, which might explain the transgranular fracture mode. At the same time, the transgranular fracture seen in Coarse spinel might be due to the enormous size of the grains in that spinel. The fracture surfaces of pure MgAl_2O_4 spinel (**Figure 4a and 4b**) and spinel with-1 wt% Si_3N_4 (**Figure 4e**), show that in the latter the grain size is significantly smaller [48]. The same is true for spinel with 3 wt% Si_3N_4 , (**Figure 4g**) which exhibits much smaller grains on the fracture surface than pure spinel. However, in this sample, it seems as if the density of voids had a stronger correlation with the fracture toughness of nanocomposite samples. The fracture toughness of pure spinel, spinel-1 wt% Si_3N_4 , and spinel-3 wt% Si_3N_4 was 5.1, 5.3, and 3.1 $\text{MPa}\cdot\text{m}^{0.5}$, respectively. The similarity of the toughness values in pure spinel and spinel having 1% Si_3N_4 indicates that 1% Si_3N_4 has a minimal impact on the toughness of spinel composites. Gledhill et al. reported a toughness of 1.3 $\text{MPa}\cdot\text{m}^{0.5}$ for an unheated composite, lower than the value obtained in previously discussed research [17]. The hardness of pure spinel, spinel-1 wt% Si_3N_4 , and spinel-3 wt% Si_3N_4 was 7.7, 8.1, and 10.2 GPa, respectively. Heat-treated samples provide a greater hardness value than unheated samples. The combined effect of high hardness and high fracture toughness is observed in the spinel-1 wt% Si_3N_4 and can be believed to provide good wear resistance. On the other hand, the presence of voids or secondary phases has a deteriorating effect on the transparency of ceramics, in particular in the visible range. Thus, a careful optimization is required.

Figure 19 provides a comparison of hardness and shear modulus of different TCs. The cubic Si_3N_4 results as the third hardest transparent material after diamond and c-BN[72]. The excellent mechanical properties will most likely lead to excellent tribological performance of the material. In the case of TCs, there is a very significant relationship between grain size and wear resistance. TCs have the highest hardness and lowest mass loss during the scratch wear test with the load increasing progressively, which provides high wear resistance properties to TCs.

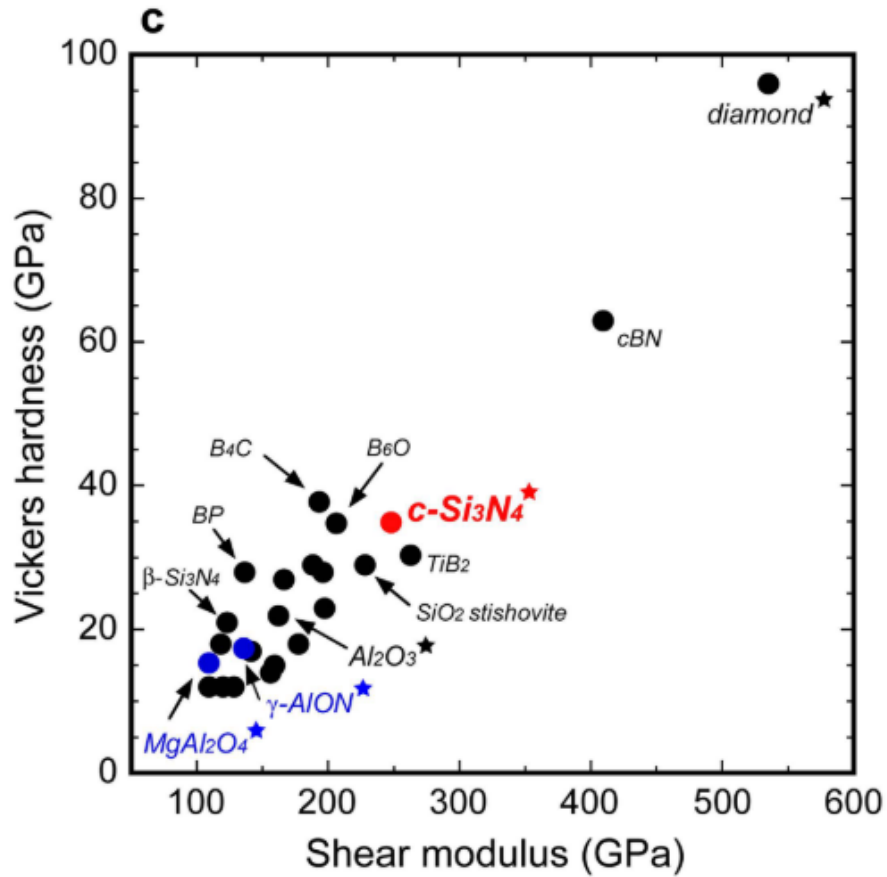


Figure 19: Vickers Hardness (1kg) of cubic silicon nitride compared to other super-hard ceramics [72].

TCs can be produced by SPS or by vacuum sintering. Compared to single crystals, the transmittance of ceramics may be lower due to scattering, as described in section 1 and illustrated in **Figure 2**. Light scatters mainly on secondary phases, grain boundaries and pores [26], which may be minimized by improving powder processing and ceramic fabrication methods. Lopez et al. [54] observed the change in the microstructure when different grain sized TC is subjected to wear. The material removal from the surface of the coarse and nano grained TCs experience transgranular fracture while performing sliding wear test. In contrast, fine grain size TCs i.e., the grain size between coarse grain and nano grain experience intergranular fracture during sliding wear. The micrographs of fracture surface for coarse, nano and fine grain after sliding wear are shown in **Figure 20a, 20b and 20c** respectively.

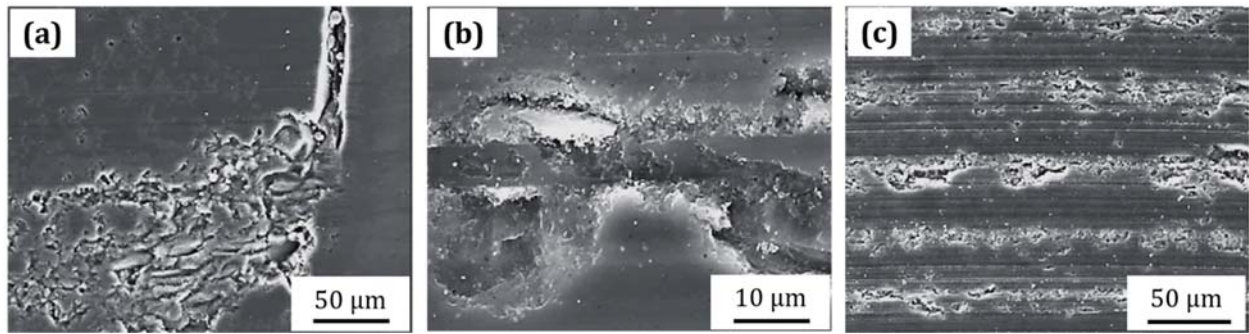


Figure 20: SEM micrographs of fracture damage in wear scars in a) coarse spinel, b) nano spinel and c) fine spinel at the end of the sliding wear test (1000 min) [54].

Subsurface damage induced in the nanoscratch changes the mechanical properties of the TC [184]. Zang et al. [184] investigated the wear performance of Lu_2O_3 TCs by single nanoscratch, repeated nanoscratch, and double nanoscratch experiments on a nanoindenter. After the first scratch, the residual material changed to a combination of polycrystalline nanocrystallites and amorphous from original micron-size grains. At the same time, many defects, viz., dislocations, stacking faults, nano twins, torsion of an atomic plane, fracture of the atomic plane, and wrong arrangement of the atomic plane were induced in nanograins during the nanoscratch process. The mechanical property of a combination of polycrystalline nano-crystallites and amorphous phases with many atomic-scale defects was different from that of micron-sized grains. These changes of mechanical properties result in the decrease of friction coefficient in the repeated scratch.

Table 4 shows the mechanical, optical, and tribological behavior of different TCs and **Table 5** shows the potential tribological behavior with respect to improved mechanical properties of TCs. **Figure 21a and 21b** show the comparison of mechanical properties (hardness and fracture toughness) and transparency of selected TCs. In the case of spinel, Y_2O_3 , Si_3N_4 or SiAlON the change that led to an increase of hardness led also to a better transparency, while in the case of fracture toughness such a trend is not fully clear. All these properties are highly microstructure-dependent, but not always in the same way.

Table 5: Mechanical, optical, and tribological behaviour of TCs.

Material	Sintering Additives	Sintering Parameters	Transparency (%)		Mechanical Properties			Tribological test parameters	Cof	Wear Vol. mm ³ /Rate mm ³ Nm ⁻¹	Microstructure	Tribological outcomes	Ref.
					Relative Density (%)	Hardness (GPa)	Fracture Toughness (MPa.m ^{0.5})						
Si₃N₄ (3wt.% MgO + 9wt.% AlN + 1 wt.% REO) (α phase)	Y ₂ O ₃ 1wt%	Type- HP Atmosphere- N ₂ Pressure- 30 MPa Sintering Temperature- 1850 °C Holding Time- 60 min	54	From 500-2500 nm	99.6	21.1	8.5	Load-10N Time-30min Reciprocating	0.33	-	Lower β phase than undoped silicon nitride with interwoven structure. Grain pull-out showed abrasive wear during sliding	An increase in hardness and fracture toughness results in decreased cof	[65]
	Nd ₂ O ₃ 1wt%	50	99.5		20.9	7.9	0.36						
	Er ₂ O ₃ 1wt%	40	99.3		20.5	7.1	0.39						
	None	64	99.0		20.1	5.9	0.41						
Si₃N₄ (3wt.% MgO + 9wt.% AlN + BN) (α phase)	h-BN (0.25%)	Type- HP Atmosphere- N ₂ Pressure- 30 MPa Sintering Temperature- 1850 °C Holding Time- 60 min	57	From 500-2500 nm	96.7	18.5	6.2	Time-60min Reciprocating	-	0.0350 mm ³	Debris of α-Si ₃ N ₄ made a thin film and decreased wear volume.	Decrease in hardness and increase in fracture toughness results indecreased cof and wear volume	[37,100]
	h-BN (0.5%)	43	93.6		17.75	7.4	0.21		0.0345 mm ³				
	h-BN (1%)	40	92.3		17	7.3	-		0.0320 mm ³				
	h-BN (2%)	25	90.1		16.5	7.3	0.19		0.0280 mm ³				
	None	-	99.0		20.5	5.9	0.24		0.0355 mm ³				
Spinel (MgAl₂O₄)	Commercially available TC was used for the experimentation	Highly transparent	99.5		14.12 ± 0.77	-	Linear reciprocating ball- on-disc Counter-body- Al ₂ O ₄ Load- 20N Velocity- 5000 ms ⁻¹	0.42 ± 0.02	0.094 ± 0.02 mm ³ / 4.72 ± 1.22 mm ³ Nm ⁻¹ (for 1000m) 0.316 ± 0.05 mm ³ / 5.27 ± 0.85 mm ³ Nm ⁻¹ (for 3000m)	-	An increase in the sliding distance, the wear rate increases. Parallel arrays of fatigue cracks, oriented perpendicular to sliding direction were observed on surface indicating fatigue type wear.	[28]	
AION	Commercially available TC was used for the experimentation	Highly transparent	99.6		16.33 ± 0.5	-	Linear reciprocating ball- on-disc Counter-body- Al ₂ O ₄ Load- 20N	0.45 ± 0.02	0.250 ± 0.01 mm ³ / 12.5 ± 2.16 mm ³ Nm ⁻¹ (for 1000m)	-	Parallel arrays of fatigue cracks, oriented perpendicular to sliding direction were observed on surface indicating fatigue type wear. It was observed that with an increase in the sliding distance, the wear rate	[28]	

						Velocity- 5000 ms ⁻¹		0.606 ± 0.03 mm ³ 10.1 ± 0.27 mm ³ Nm ⁻¹ (for 3000m)		gradually decreased and reached a constant value	
Lu ₂ O ₃	Commercially available TC was used for the experimentation	Highly transparent	-	10.95	-	Single Nanoscratch	0.272 ±0.02	-	Grain boundaries in Lu ₂ O ₃ TCs are extremely weak, and the mismatch degree between neighbouring grains is high. As a result, subsurface fractures cracks propagate along grain boundaries	In repeated nanoscratch tests, the friction coefficient increases and tends to be stable with the increase of normal force. The ductile deformation mechanism of Lu ₂ O ₃ TCs during the nanoscratch process is a combination of polycrystalline nano-crystallites in inner grain and amorphous transformation. The dominant subsurface crack propagation for Lu ₂ O ₃ TCs is an intergranular fracture. In addition, a small number of transgranular cracks and discontinuous cracks are also found in subsurface	[184]
						Repeated Nanoscratch	0.245 ±0.03				

Table 6: Potential tribological behaviour with respect to improved mechanical properties of TCs.

Material	Experiment condition	Sintering Parameters	Transparency (%)		Mechanical Properties				Microstructure	Potential Tribological outcomes	Ref.
					Mean grain size (nm)	Relative Density (%)	Hardness (GPa)	Fracture Toughness (MPa.m ^{1/2})			
Si ₃ N ₄ (α phase) <0.5 μ m	Additive- MgO (10nm) 12wt%	Type- SPS Atmosphere- N ₂ Pressure- 50 MPa Sintering Temperature- 1850 °C Holding Time- 5 min	~ 0	From 400-900 nm	290	97	12.1-13.1	6.7-7.7	β phase was formed after sintering. No change in the mean grain size, i.e., 0.29 μ m of transparent Si ₃ N ₄ , was observed with a change in percentage of MgO, but the mean grain size was reduced from 0.37 μ m to 0.34 μ m when Y ₂ O ₃ was increased from 2% to 12%.	2 wt% Y ₂ O ₃ in Si ₃ N ₄ can provide high wear resisting properties to the TC.	[99]
	Additive- Y ₂ O ₃ (0.7 μ m) 12wt%		~ 0		340	99.8	13.4-14.0	6.3-7.1			
	Additive- Al ₂ O ₃ (0.5 μ m) 12wt%		-		-	95.3	-	-			
	Additive- MgO (10nm) 2wt%		~ 0		290	99.3	14.0-16.0	6.4-6.6			
	Additive- Y ₂ O ₃ (0.7 μ m) 2wt%		0-35		370	99.9	14.9-15.9	6.1-6.7			
	Additive- Al ₂ O ₃ (0.5 μ m) 2wt%		-		-	85.9	-	-			
Y ₂ O ₃ (<74 μ m)	Heating rate- 10 °Cmin ⁻¹	Type- SPS Pressure- 70	46		499	-	-	1.1	With an increase in the heating rate, the mean grain size of	High heating rate may result to provide small grain size	[95]

	Heating rate- 20 °Cmin ⁻¹	Sintering Temperature- 1250 °C Holding Time- 10 min	49		410			1.4	transparent Y ₂ O ₃ was decreased significantly	and high fracture toughness which can lead to high wear resistance	
	Heating rate- 50 °Cmin ⁻¹		64		205			1.3			
	Heating rate- 100 °Cmin ⁻¹		66		164			1.3			
Y₂O₃ (90nm)	Preload Pressure – 10MPa	Pressure conditions- It was increased to 100 MPa at 1000 °C and was kept constant during sintering and cooling Heating rate conditions- 100 °C/min 600°C, 25°C/min 1000°C, held 5 minutes, 10°C/min 1300 °C	76.7	At 200 nm	260	99.4	8.32 ± 0.18	1.25 ± 0.07	With an increase in preload pressure, mean grain size is reduced, and no phase transformation was observed	An increase in preload pressure results in to decrease in the hardness and fracture toughness value, which may provide less wear resistance properties	[94]
	Preload Pressure – 30MPa		70.2		320	98.8	7.56 ± 0.16	1.20 ± 0.05			
	Preload Pressure – 50MPa		51.1		450	98.7	7.01 ± 0.20	1.14 ± 0.04			
MgAl₂O₄	0 wt% LiF	HP vacuum sintering at 1600 °C for 60 min	34	At 1100 nm	3 ± 0.8	-	-	-	Bimodal microstructure converted to equal grain size distribution with increase in wt% addition of LiF	The addition of LiF promotes a fine structure and low porosity and may improve the hardness and in turn the tribological characteristics	[60]
	0.5 wt% LiF		40		38 ± 13						
	1 wt% LiF		44		20 ± 10						
MgAl₂O₄	0 wt% Si ₃ N ₄	SPS with maximum pressure and temperature of 80 MPa and 1550 °C for 20 min and heat treated	75	At 2500 nm	-	-	8.2	-	The porosity of the composite material increased with increase in the addition of Si ₃ N ₄	Maximum shear strength of MgAl ₂ O ₄ -1 wt% Si ₃ N ₄ indicates the maximum fracture toughness and potential for highest wear resistance	[48]
	1 wt% Si ₃ N ₄		71				9.3				
	3 wt% Si ₃ N ₄		58				12.1				

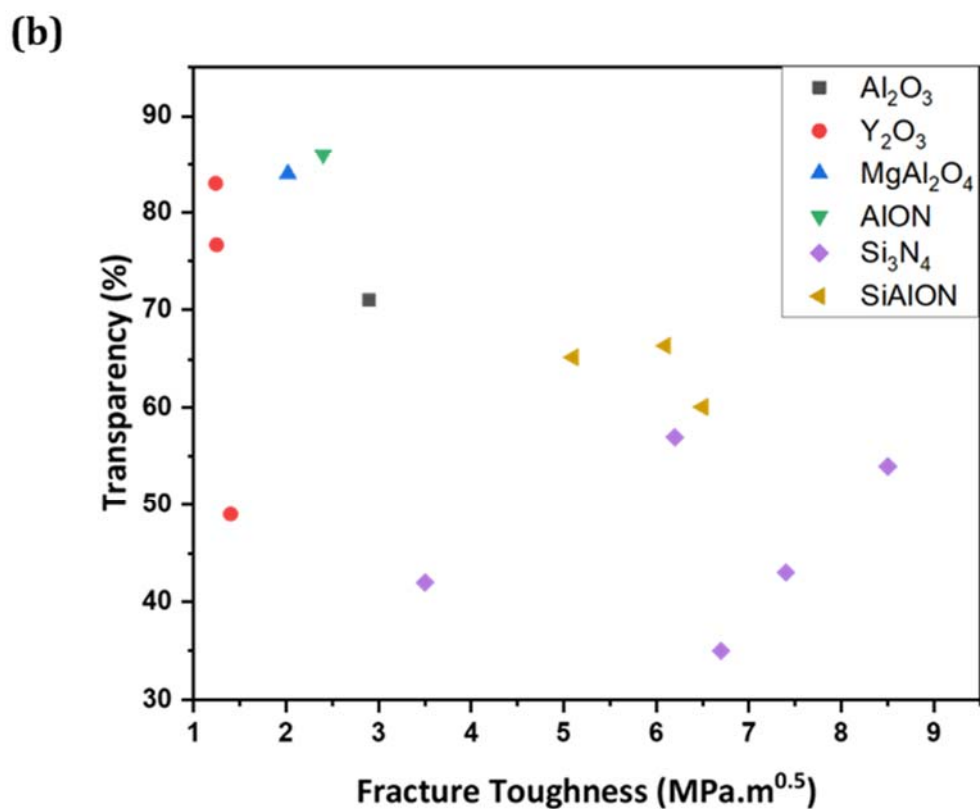
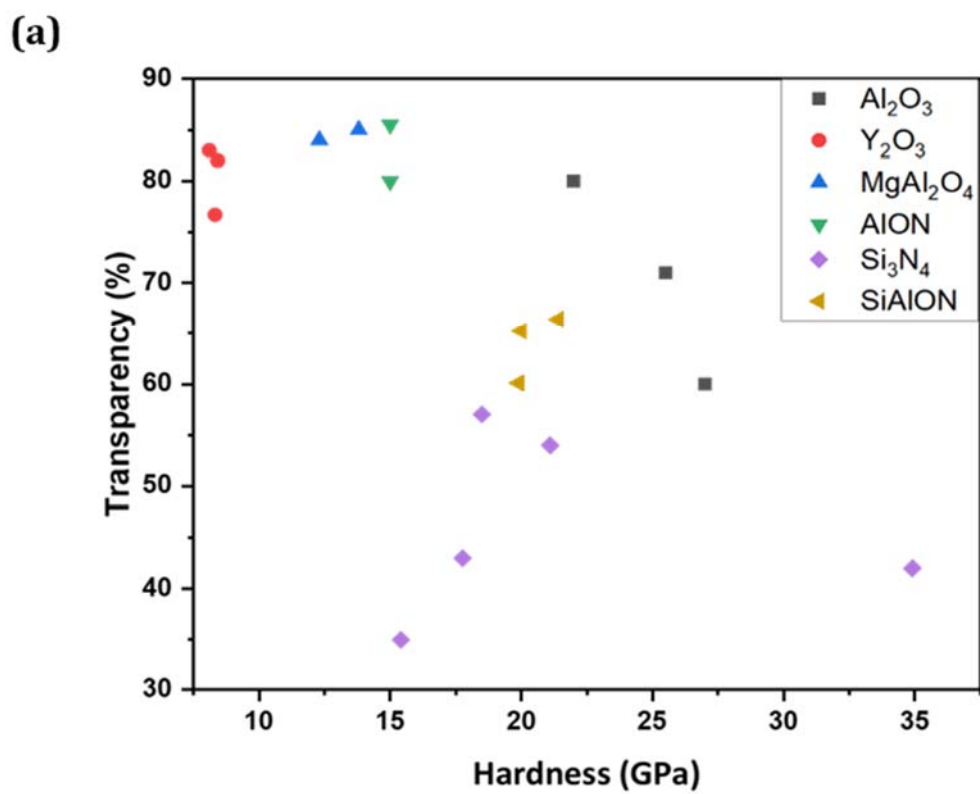


Figure 21: Transparency vs. a) Hardness, and b) Fracture Toughness for different TCs [27,37,59,63,65,75,83,86,92–101,111,112]

The effect of pressure during sintering has various conflicting outcomes for the change in the microstructure of the TCs. When it comes to transparent cubic zirconia (c-ZrO₂), the studies established no effect of pressure on grain growth [232,233]. However, another study [234] found an increase in grain size when the pressure was increased, which may decrease the wear resistance. On the other hand, a study [235] found both phenomena to occur: a minimal pressure influence on grain growth at low temperature (1100°C) and a considerable pressure effect on grain growth acceleration at high temperature (1200°C).

In addition, when compared to pressureless sintering under vacuum, the use of pressure-assisted methods allows the use of lower sintering temperatures. The densification is one of the significant factors for wear resistance because densification and reduction of porosity during sintering affect the tribological performance of the TC. When SPS is used to obtain transparent ceramics, sintering occurs from inside to outside of the sample for the low heating rate at high pressure (400 MPa) [235], and from outside to inside for high heating rate at low pressure (80 MPa) [236]. The increase in pressure allows to reduce the sintering temperature and to develop a fine grain size [47,237]. Kim et al. [235] also studied the pressure effect on the grain and grain boundary of the MgO-doped transparent Al₂O₃. It was observed that the compressive pressure [238] lowers both the free volume and the transfer of atoms between grain boundaries, resulting in reduced grain-boundary mobility and decreasing the wear resistance of the TC. Consequently, the increase in the hydrostatic pressure leads to the densification of the polycrystals and to a decrease of the grain growth rate.

It may be concluded that the pressure increase during sintering should lead to the production of TCs with a fine structure and a low grain-boundary movement, which in turn may increase the wear resistance of these materials.

4. Mechanisms of material removal

Wear modes vary according to the materials in contact, working load, mode and speed of relative motion, temperature, lubrication conditions, and environment. As a result, wear mechanisms vary considerably from case to case [239]. In addition, the predictive and quantitative modelling of the wear mechanism is complicated compared to contact mechanic issues. This section includes discussions on a material removal mechanisms in terms of material properties during the tribological application of TCs. Different friction and wear coefficients between different tribopairs indicated complicated material removal processes. The change in the microstructure and mechanical properties of the TCs affects its material removal mechanism [73,223,224]. The

densification of TCs and the respective sintering conditions also affect the material removal mechanism during wear.

Abrasive particles may develop during the wear process due to work hardening, phase changes, and the creation of a third body at the interface during sliding [240]. When hard asperities or hard particles travel over a soft surface, as well as when hard particles travel over a hard surface, abrasion occurs in both cases [145]. There are three types of mechanisms observed during abrasive wear, i.e., micro-cutting, wedge formation, and ploughing [241,242]. When the hard particles slide over a soft surface it may result in formation of debris. When the debris is produced in form of chips, the mechanism is called micro-cutting. The wedge formation is observed when the abrasive particles slide on the material and the material deposit at certain position. The micro-cutting and wedge formation of abrasion are generally observed for low scratch length during sliding [243]. However, if debris is not formed, the action is called ploughing. Both cutting and ploughing result in plastic deformation and strain hardening of the material which improve the hardness and wear resistance of the material. This is not the case when hard asperities travel over a hard surface as no plastic deformation is possible for brittle material. Therefore, three types of cracks are observed in the material, i.e., radial, median and lateral cracks (**Figure 3**). Studies reveal that the wear behaviour of TCs is abrasive [35,37,65,66]. Joshi et al. [37] depicted that worn surfaces on transparent Si₃N₄ were formed due to the pulling out of grains during the wear experiment, with an abrasive wear. Also, if the grains of doping agents are more easily pulled, because of the interlocking of the asperity and the grain of the doping agent, the abrasion increases. The interlocking of abrasive particles and doping particles and their wear is shown in **Figure 22a and 22b**. The grain size of the doping agents and of the parent phase must be similar for low abrasive wear rate. The shape of the grain also affects the wear behaviour, like β-Si₃N₄ has a large elongated grain structure compared to α-Si₃N₄, and indeed α-Si₃N₄ has better tribological characteristics [65]. Similarly, the incorporation of nano twins into nanostructured polycrystalline cBN produced from onion-like Boron Nitride (oBN) results to form equiaxed grains, which led to an increased hardness and improved wear resistance of TC.

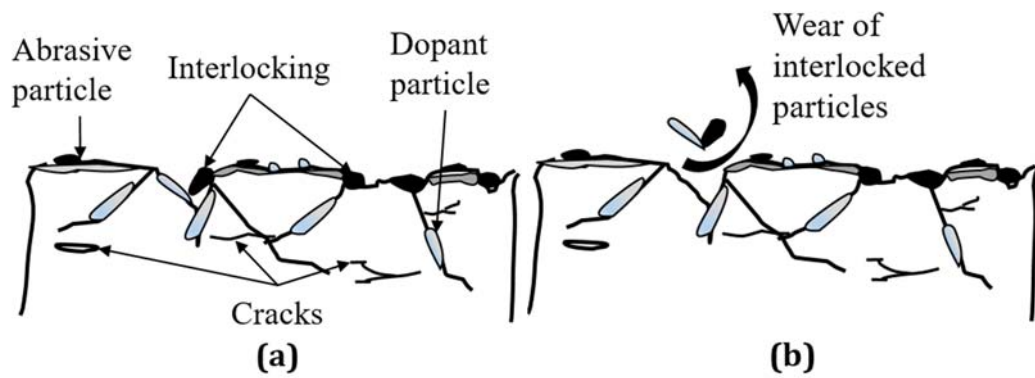


Figure 22: Representation of a) interlocking of abrasive and doped particle, and b) their wear during sliding of abrasive particle on transparent ceramic.

To understand the wear mechanism, a scratch test was performed on TC-like MgAl_2O_4 [66]. Three different regimes were distinguished along the scratch direction *viz.*, micro-ductile, micro-cracking, and micro-abrasive as discussed previously in **Figure 3**. In every regime, the transport and removal of material are governed by abrasive wear. Different types of cracks are intensely influenced by applied load and stress. The median, radial, and lateral fractures contribute to the characteristic wear pattern. Scratch testing was also used to analyze the mechanical and tribological properties of transparent Lu_2O_3 , as mentioned in **section 2.4**. Hard-brittle transparent materials with a brittle surface deformation characteristic and a material removal process were studied, and the results offered valuable information [184]. Several imperfections, comprising dislocations, stacking faults, nano twins, atomic plane torsion, atomic plane fracture, and atomic plane misalignment were produced in nanograins due to the nanoscratch process. All kinds of defects interacted differently towards material removal during scratching. When scratching TCs, the interaction between scratches has a significant effect on the material removal mechanism. While performing the scratch experiment, the material removal mechanism is dependent on scratch length. A ductile material removal mechanism is observed if the scratch length is large and brittle for a small scratch length [243].

Benaissa et al. [35] fabricated various MgAl_2O_4 TCs by SPS at different sintering temperatures and observed after tribological testing that these samples had an abrasive wear mechanism. Besides, it was also noted that the friction coefficient changed in a specific way for each sintering temperature variation. The authors further pointed out that the mass loss increased during wear as the sintering temperature increased. The wear volume of the TC was found to be proportional to its hardness. The hardness of TCs increases with the reduction of the sintering temperature as the grain size decreased and the hard TC prevent the particles being pulled away from the surface. On

increasing the grain size of the sintered samples during high sintering temperature, the grain pulled-out and abrasion wear of TCs increased. As the wear rate and mechanism is directly related to the mechanical properties of the material, Zhao et al. [174] observed wear mechanism for TC with additives. The nano-sized silicon carbide (SiC) and zirconia (ZrO₂) particles were added to AlON by hot-press sintering which significantly increased the mechanical characteristics (relative density, microhardness, Young's modulus, flexural strength, and fracture toughness). Additionally, the fracture mode in the nanoparticle reinforced composites shifted from intergranular to mixed cracking. Numerous toughening mechanisms were observed in SiC and ZrN nanoparticulate reinforced AlON composites, including crack deflection, crack bridging, and crack branching, as indicated in **Figure 23**. These mechanisms effectively increased the crack propagation resistance, resulting in an increase in flexural strength and fracture toughness of 41.4% and 28.6%, respectively, when compared to pure AlON.

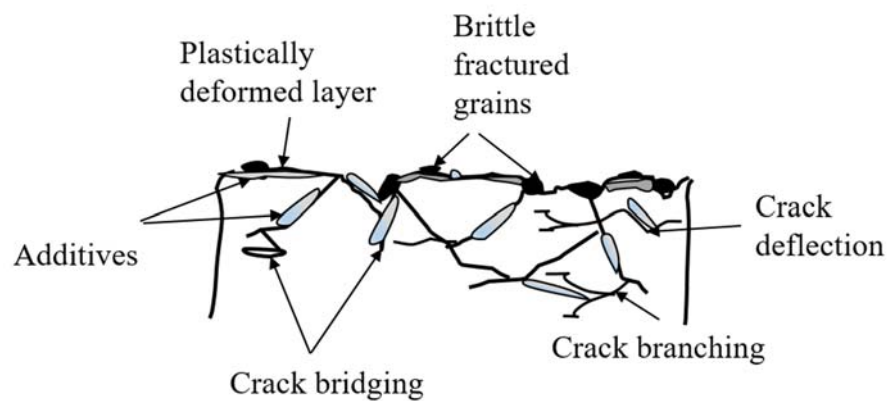


Figure 23: Different toughening mechanisms observed in TCs, including crack deflection, crack bridging, and crack branching.

To understand the ductile deformation mechanism of transparent Lu₂O₃ during sliding wear, transmission electron microscopy was conducted [184]. It was observed that subsurface of TC contains three types of grains beneath the scratch, as shown in **Figure 24a and 24b**. The first scratch is concentrated on Grain 1, whereas the second scratch is concentrated on Grain 3. When the cutting depth was within a certain depth, there was an evident plastic flow region with no fractures in the subsurface and the machining operation was fully ductile machining. The TEM images indicated that the mechanism was a mix of polycrystalline nanocrystallites in the inner grain and amorphous transformation, as shown in **Figure 25a**. Numerous defects like dislocations, stacking faults, nano twins, twisting of atomic planes, fracture of atomic planes, and incorrect arrangement of atomic planes were induced in nanograins formed during the nano-scratch process as a result of the stress field (**Figure 25**). Similar to the research on the ductile deformation mechanism of Gd₃Ga₅O₁₂ single crystal [244], when single crystal grains transform into

polycrystalline nanocrystallites, the plastic deformation mechanism shifted from intragranular dislocation to grain boundary movements, such as grain sliding [245,246], grain rotation [247–250], and grain migration [251]. Specifically, the scratch subsurface of Grain 3 was separated into three regions, as shown in **Figure 25b**: the plastic flow region, the transitional region, and the grain matrix. Large amount of residual stress was observed in plastic flow region. Numerous flaws formed during the machining operation are also present in the nano grains of the plastic flow zone (**Figure 25c and 25d**).

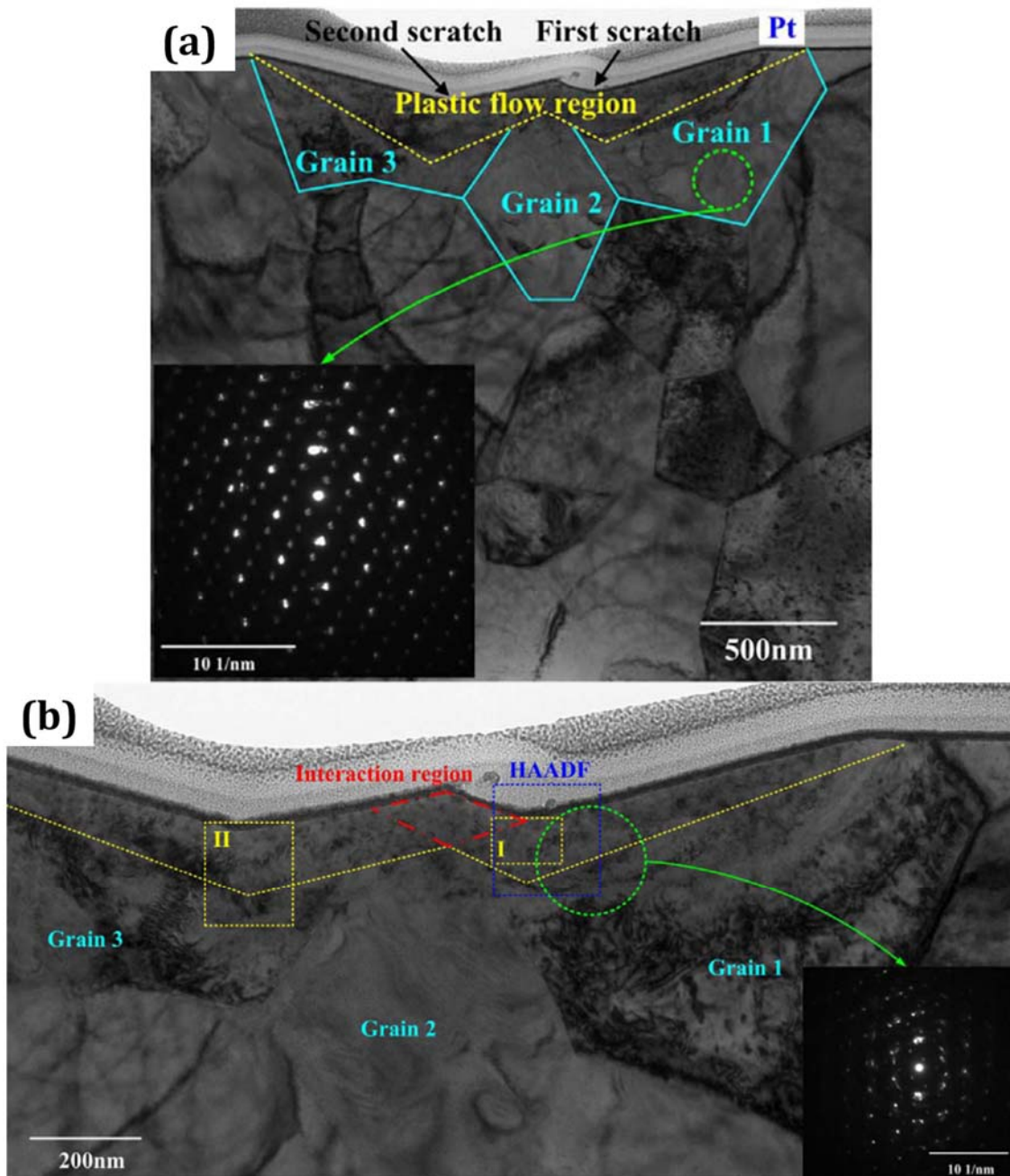


Figure 24 Transmission electron micrographs of transparent Lu_2O_3 during sliding wear [184].

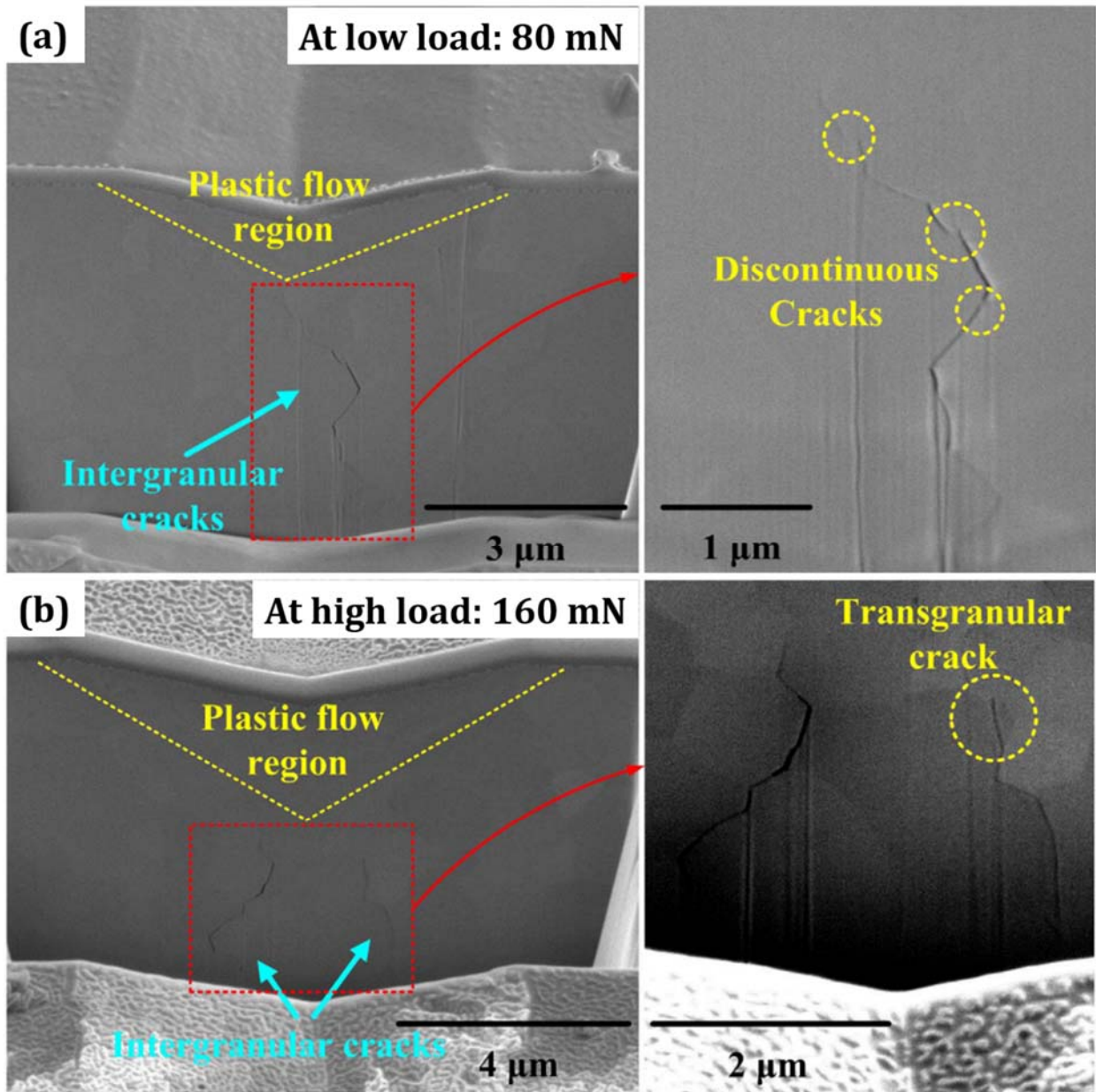


Figure 25 Crack propagation in transparent Lu_2O_3 under a) low load and b) high load conditions [184].

Microstructure refinement generally leads to a significant increase in hardness. The hardness of the TC is affected by numerous factors. The wear volume of the TC is found to be proportional to its hardness. TC's hardness increases as the grain size decreases, and the hard TC resists surface wear [35]. Sheikh et al. [51] also investigated transparent $\text{MgAl}_2\text{O}_4/\text{Si}_3\text{N}_4$ nanocomposite for hardness, fracture toughness, and transparency. The decrease of transparency and enhancement in mechanical properties is due to the presence of Si_3N_4 reinforcing nanoparticles and the relative toughening mechanism of MgAl_2O_4 . **Figure 26** illustrates the surface morphologies of the wear surfaces of TC sintered at 1300°C , 1350°C , and 1400°C . The grain size obtained at a higher sintering temperature is considerably higher than that obtained at a lower temperature. At all

sintering temperatures, wear surfaces of the transparent spinel showed some grooves, demonstrating that abrasion wear was the dominant mode of wear in sintered samples. It was evident that increasing the grain size of the sintered sample resulted in increased abrasion wear. The addition of Dy₂O₃ to Si₃N₄ combined with AlN and Al₂O₃ resulted in a TC with a high fracture toughness and hardness. No glassy phase was observed at the grain boundary coupled with a homogeneous microstructure with equiaxed grains [101]. The addition of a doping agent provided a homogenous crystalline microstructure with increased hardness and fracture toughness resulting in improved wear resistance with a change in material removal mechanism.

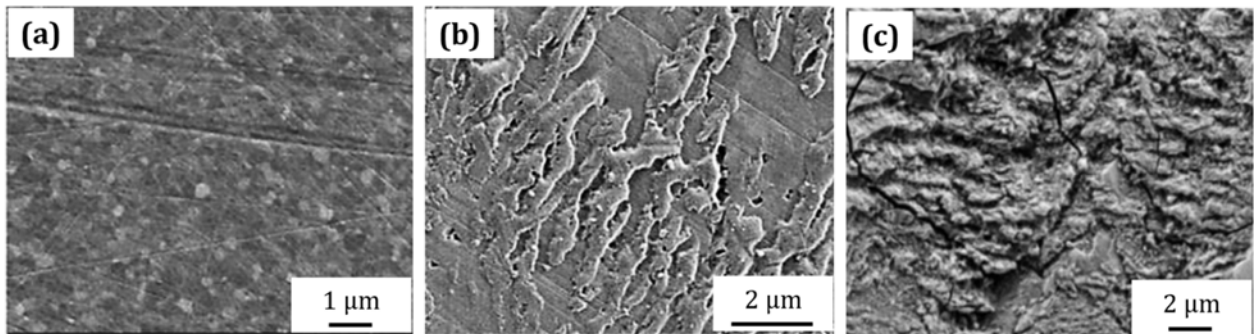


Figure 26: Morphologies of the worn surfaces of transparent MgAl₂O₄/Si₃N₄ nanocomposite sintered at a) 1300°C b) 1350°C c) 1400°C [35] passing from grooves, to accumulated material and cracking of the worn surface due to an increased grain size of the matrix.

Bodhak et al. [28] fabricated MgAl₂O₄ for an application in total hip arthroplasty and total knee arthroplasty, testing the fretting wear in the joint. Generally, a material's wear resistance is directly proportional to its hardness, i.e., the higher the hardness, the greater the wear resistance. However, there are certain circumstances and materials in which hardness does not go along with wear [252–254]. To understand the wear mechanism, SEM images of spinel and AlON's worn tracks were observed by Bodhak et al. [28] in stimulated body fluid medium. High magnification analysis revealed parallel arrays of fatigue fractures aligned perpendicularly to the sliding direction. The surface of both transparent AlON and MgAl₂O₄ indicated fatigue type wear. Repeatedly, the tiny microcracks merged to form a longer crack. However, the degree of flaking and formation of wear debris increase and became more visible on AlON surface. The wear mechanism was believed to change from abrasive and brittle fracture to fatigue wear due to the formation of lubricating films on the surfaces during the wear tests. Another study on wear simulation of Al₂O₃-on-Al₂O₃ prosthetic hip joints used a multidirectional motion pin-on-disk device in distilled water and calf serum [89] and also showed mild abrasion as dominating wear mechanism. It was concluded that the differences in surface roughness and method of preparation of TC contributed to different wear mechanisms and wear rates.

The material removal mechanism of TCs is directly affected by their densification degree. Transparent Y_2O_3 ceramic demonstrated that the powders processed with ball milling exhibit enhanced densification during SPS, possibly changing the material removal mechanism during wear [113]. There are two potential explanations: 1) The imperfections produced on the powder surfaces increase the electric current's impact during SPS processing. The milling process introduces large amounts of defects onto the powder surfaces. These defects enhance the conductivity of Y_2O_3 and subsequently improve sintering kinetics by an increase of electric current during SPS sintering. 2) The milling process may decrease particle size, which may be related to the current effect generated during SPS processing. Both these explanations demonstrate that the mechanism for material removal will be different for different wear tests.

An [186] fabricated transparent Lu_2O_3 ceramics by SPS using LiF as a sintering aid. The pressure and temperature of SPS varied between 20-100 MPa and 1000°C-1600°C, respectively, for 5-600 minutes. The fracture surface of the TC was intergranular below 1500°C and transgranular above 1500°C. A relationship has been established between the fracture toughness of TC and intergranular fracture occurring in TCs. An intergranular fracture occurs with coarse-grained microstructures, which is most likely caused by grain-boundary embrittlement. The embrittlement is produced by residual LiF, impurities, or residual stress [146]. It has been postulated that the weak boundaries of huge grains serve as critical surface defects in forming large grains. The fracture between grains that persists in coarse-grained microstructures lowers the overall strength of the material, which subsequently affects the tribological characteristic of the TC. Similarly, the fracture mechanism for transparent cBN changed from intergranular to transgranular when the sintering temperature is increased [205].

During rapid grain formation, the residual porosity in the sintered body may be maintained, decreasing fracture toughness [205]. Thus, pore removal at the optimal sintering temperature is critical for creating a well-sintered material with superior mechanical properties. Comparing the sintering behavior of fine powder and coarse powder reveals that fine powder has a more significant driving force potential due to its large surface area. For example, the surface area of fine powder with particles ranging from 0.5 to 1.2 μm is about ten times that of coarse powder with particles ranging from 8 to 12 μm [205]. These findings suggest that rapid grain formation occurs quickly in fine powders around the optimum sintering temperature. With decreasing particle sizes, controlling the sintering environment to create dense sintered bodies becomes increasingly tricky. Controlling the sintering temperature in fine-grained powders without causing grain formation is not straightforward, but affects the tribological characteristics.

5. Conclusions

This review aims to provide some meaningful guidelines for tribologists on the future study of tribological behaviour of transparent ceramics while identifying the wear mechanisms under particular wear conditions. Considering the wide range of tribological applications, wear behaviour of TCs is extensively discussed in the present review and the following observations have been derived.

1. The microstructure of the TCs influences the mechanical, tribological and optical properties. There is a strong effect of microstructure, but the effect may not always be the same. Porosity affects all of the properties negatively, the presence of a secondary phase may enhance mechanical (and tribological) properties, but has a deleterious effect on the transparency. A solution may come from a significant reduction of the grain size. The effect is stronger in the visible range compared to IR.
2. An increase in sintering temperature results in grain growth. In the case of non-cubic materials (e.g. alumina) or composite ceramics, this causes a reduction of transparency. The grain refinement of transparent ceramics is required to improve the mechanical behavior, which further enhances the tribological performance of TCs. Therefore, optimum grain size is needed to achieve good tribological behavior and good transparency. Fine-grained TCs are promising for both mechanical and optical properties and can be successfully produced by SPS.
3. Fracture of TCs introduce median, radial, and lateral cracks, which result in formation of debris. Besides the major microstructural factors affecting the wear of TC (porosity, phase composition, surface finishing) other minor influence is given by dislocations, stacking faults, nano twins, atomic plane torsion, atomic plane fracture, and atomic plane misalignment during scratching or erosion of TC.
4. Fracture toughness is highly affected by the microstructure of materials. It may be enhanced by encouraging strengthening and toughening mechanisms such as crack bridging, crack deflection, and crack branching, which absorbs some of the energy required to propagate fractures.
5. The mechanical properties of a combination of polycrystalline nano-crystallites and amorphous phases with many atomic-scale defects is different from that of micron-sized grains. These changes of mechanical properties result in the decrease of friction coefficient in the scratching or erosive environment.
6. Abrasive particles may develop during the wear process due to work hardening, phase changes, and the creation of a third body at the interface which are responsible for abrasive wear mechanism

in the TCs. TCs operated under lubricated conditions are observed to experience fretting wear mechanism rather than abrasive wear mechanism.

6. Future Scope

For a comprehensive wear behaviour of TCs, microstructural characteristics must be included into modern wear models/theories in order to accurately estimate material removal under sliding or erosive situations. The majority of studies reported ambient temperature wear behaviour by estimating mechanical and microstructural characteristics of TCs, whereas the effect of mechanical and microstructural features at elevated temperatures must be considered for tribological applications at higher temperatures. Additionally, little research has been conducted on TCs to better understand their behaviour in low temperature wear applications. A future research examining the influence of mechanical or microstructural properties at low temperatures should evaluate the possibility of using TCs for space or marine applications.

Additionally, the mechanics of deterioration under various wear circumstances must be completely understood. In light of the tribological performance, the parameters defining the microstructure (e.g. the amount of additive, the sintering method, sintering temperature, and sintering pressure) which are responsible for microstructural features must be studied in detail. Furthermore, studies must be expanded to better understand the performance of TC with high hardness and fracture toughness. The dependence of the ratio between hardness and fracture toughness, which is a prominent aspect of wear resistance of the ceramic materials, should be studied in case of TCs. Also the material removal mechanisms of TCs should be investigated in detail. While the majority of published research focuses on understanding the behaviour of transparency of TCs, one needs to examine the tribological potential of TCs for use in critical fields such as, explosive ordnance visors, aircraft, spacecraft, re-entry vehicles, electromagnetic windows, face shields, screens for smartphones and more. Lastly, and most importantly, the optical properties upon impact or scratch should be investigated in view of prolonged use.

References

1. Coble, R.L. Transparent Alumina and Method of Preparation 1962.
2. Gatti, A.; Noone, J. Feasibility study for producing transparent spinel. *AMMRC-CR* **1970**, 70–80.
3. Ballard Jr, C.P. Transparent ceramic armor 1978.
4. Ikesue, A.; Kinoshita, T.; Kamata, K.; Yoshida, K. Fabrication and Optical Properties of High-Performance Polycrystalline Nd:YAG Ceramics for Solid-State Lasers. *J. Am. Ceram. Soc.* 1995, 78, 1033–1040.
5. Wei, G.C. Transparent ceramic lamp envelope materials. *J. Phys. D. Appl. Phys.* **2005**, 38, 3057–3065, doi:10.1088/0022-3727/38/17/S07.
6. IKESUE, A.; AUNG, Y.L.; LUPEI, V. Ceramic Lasers. *J. Phys. D. Appl. Phys.* **2013**, 28, 3057–3065.
7. Krell, A.; Klimke, J.; Hutzler, T. Advanced spinel and sub-micrometer Al₂O₃ for transparent armour applications. *J. Eur. Ceram. Soc.* **2009**, 29, 275–281, doi:10.1016/j.jeurceramsoc.2008.03.024.
8. Harris, D.C. Durable 3–5 μm transmitting infrared window materials. *Infrared Phys. Technol.* **1998**, 39, 185–201, doi:10.1016/S1350-4495(98)00006-1.
9. Wang, S.F.; Zhang, J.; Luo, D.W.; Gu, F.; Tang, D.Y.; Dong, Z.L.; Tan, G.E.B.; Que, W.X.; Zhang, T.S.; Li, S.; et al. Transparent ceramics: Processing, materials and applications. *Prog. Solid State Chem.* **2013**, 41, 20–54, doi:10.1016/j.progsolidstchem.2012.12.002.
10. Krell, A.; Bales, A. Grain size-Dependent hardness of transparent magnesium aluminate spinel. *Int. J. Appl. Ceram. Technol.* **2011**, 8, 1108–1114, doi:10.1111/j.1744-7402.2010.02583.x.
11. Goldstein, A. Correlation between MgAl₂O₄-spinel structure, processing factors and functional properties of transparent parts (progress review). *J. Eur. Ceram. Soc.* **2012**, 32, 2869–2886, doi:10.1016/j.jeurceramsoc.2012.02.051.
12. Sands, J.M.; Fountzoulas, C.G.; Gilde, G.A.; Patel, P.J. Modelling transparent ceramics to improve military armour. *J. Eur. Ceram. Soc.* **2009**, 29, 261–266,

- doi:10.1016/j.jeurceramsoc.2008.03.010.
13. Straßburger, E. Ballistic testing of transparent armour ceramics. *J. Eur. Ceram. Soc.* **2009**, *29*, 267–273, doi:10.1016/j.jeurceramsoc.2008.03.049.
 14. Klement, R.; Rolc, S.; Mikulikova, R.; Krestan, J. Transparent armour materials. *J. Eur. Ceram. Soc.* **2008**, *28*, 1091–1095, doi:10.1016/J.JEURCERAMSOC.2007.09.036.
 15. Lempicki, A.; Brecher, C.; Szupryczynski, P.; Lingertat, H.; Nagarkar, V. V.; Tipnis, S. V.; Miller, S.R. A new lutetia-based ceramic scintillator for X-ray imaging. *Nucl. Instruments Methods Phys. Res. Sect. A Accel. Spectrometers, Detect. Assoc. Equip.* **2002**, *488*, 579–590, doi:10.1016/S0168-9002(02)00556-9.
 16. Wei, N.; Lu, T.; Li, F.; Zhang, W.; Ma, B.; Lu, Z.; Qi, J. Transparent Ce:Y 3Al 5O 12 ceramic phosphors for white light-emitting diodes. *Appl. Phys. Lett.* **2012**, *101*, doi:10.1063/1.4742896.
 17. Nishiura, S.; Tanabe, S.; Fujioka, K.; Fujimoto, Y. Properties of transparent Ce:YAG ceramic phosphors for white LED. *Opt. Mater. (Amst)*. **2011**, *33*, 688–691, doi:10.1016/J.OPTMAT.2010.06.005.
 18. Hinklin, T.R.; Rand, S.C.; Laine, R.M. Transparent, polycrystalline upconverting nanoceramics: Towards 3-D displays. *Adv. Mater.* **2008**, *20*, 1270–1273, doi:10.1002/adma.200701235.
 19. Stanciu, G.; Stanciu, C.A.; Brandus, C.A.; Voicu, F.M.; Dascalu, T. Laser gain transparent ceramics media. *Opt. InfoBase Conf. Pap.* **2017**, *Part F67-L*, 10–12, doi:10.1364/LIC.2017.LWA5.5.
 20. Jones, I.K.; Seeley, Z.M.; Cherepy, N.J.; Duoss, E.B.; Payne, S.A. Direct ink write fabrication of transparent ceramic gain media. *Opt. Mater. (Amst)*. **2018**, *75*, 19–25, doi:10.1016/j.optmat.2017.10.005.
 21. Observatories Across the Electromagnetic Spectrum Available online: https://imagine.gsfc.nasa.gov/science/toolbox/emspectrum_observatories1.html (accessed on Jan 15, 2022).
 22. Salem, J.A. Transparent armor ceramics as spacecraft windows. *J. Am. Ceram. Soc.* **2013**, *96*, 281–289, doi:10.1111/jace.12089.

23. Krell, A.; Hutzler, T.; Klimke, J. Transmission physics and consequences for materials selection, manufacturing, and applications. *J. Eur. Ceram. Soc.* **2009**, *29*, 207–221, doi:10.1016/j.jeurceramsoc.2008.03.025.
24. Xiao, Z.; Yu, S.; Li, Y.; Ruan, S.; Kong, L.B.; Huang, Q.; Huang, Z.; Zhou, K.; Su, H.; Yao, Z.; et al. Materials development and potential applications of transparent ceramics: A review. *Mater. Sci. Eng. R Reports* **2020**, *139*, 100518, doi:10.1016/j.mser.2019.100518.
25. <https://ntrs.nasa.gov/citations/20170005664>.
26. <https://www.marketsandmarkets.com/Market-Reports/transparent-ceramic-market-78249828.html>.
27. Goldstein, A.; Krell, A.; Burshtein, Z. *Transparent Ceramics*; 2020; ISBN 9781119429494.
28. Bodhak, S.; Balla, V.K.; Bose, S.; Bandyopadhyay, A.; Kashalikar, U.; Jha, S.K.; Sastri, S. In vitro biological and tribological properties of transparent magnesium aluminate (Spinel) and aluminum oxynitride (ALON). *J. Mater. Sci. Mater. Med.* **2011**, *22*, 1511–1519, doi:10.1007/s10856-011-4332-5.
29. *Ceramic Armor and Armor Systems*; Medvedovsk, E., Ed.; The American Ceramic Society, 2003; ISBN 1574980505.
30. Kerwienb, H.; Arsenal, P. Evaluation of ALON for cannon window application. *Wind. Dome Technol. Mater.* **1999**, *3705*.
31. Patel, P.J.; Gilde, G.A.; Dehmer, P.G.; McCauley, J.W. Transparent ceramics for armor and EM window applications. *Inorg. Opt. Mater. II* **2000**, *4102*, 1–14, doi:10.1117/12.405270.
32. Boulesteix, R.; Maître, A.; Baumard, J.-F.; Rabinovitch, Y.; Reynaud, F. Light scattering by pores in transparent Nd:YAG ceramics for lasers: correlations between microstructure and optical properties. *Opt. Express* **2010**, *18*, 14992, doi:10.1364/oe.18.014992.
33. Hříbalová, S.; Pabs, W. Modeling light scattering by spherical pores for calculating the transmittance of transparent ceramics – All you need to know. *J. of the Eur. Ceram. Soc.* **2020**, *41*, 2169–2192, doi:10.1016/j.jeurceramsoc.2020.11.046.
34. Dericioglu, A.F.; Kagawa, Y. Effects of grain boundary microcracking on the light transmittance of sintered transparent MgAl₂O₄. *J. Eur. Ceram. Soc.* **2003**, *23*, 951–959, doi:10.1016/S0955-2219(02)00205-4.

35. Benaissa, S.; Hamidouche, M.; Kolli, M.; Bonnefont, G.; Fantozzi, G. Characterization of nanostructured MgAl₂O₄ ceramics fabricated by spark plasma sintering. *Ceram. Int.* **2016**, *42*, 8839–8846, doi:10.1016/j.ceramint.2016.02.130.
36. Joshi, B.; Fu, Z.; Niihara, K.; Lee, S.W. Fabrication of translucent boron nitride dispersed polycrystalline silicon nitride ceramics. *IOP Conf. Ser. Mater. Sci. Eng.* **2011**, *20*, doi:10.1088/1757-899X/20/1/012014.
37. Joshi, B.; Fu, Z.; Niihara, K.; Lee, S.W. Optical, mechanical and tribological properties of boronnitride dispersed silicon nitride Ceramics. *Korean J. Mater. Res.* **2010**, *20*, 444–449, doi:10.3740/MRSK.2010.20.8.444.
38. Tingting, W.U.; Jian, Z.; Bolin, W.U.; Wenjie, L.I. Effect of La₂O₃ content on wear resistance of alumina ceramics. *J. Rare Earths* **2016**, *34*, 288–294, doi:10.1016/S1002-0721(16)60027-3.
39. Krell, A.; Blank, P.; Ma, H.; Hutzler, T.; Bruggen, M.P.B. Van; Apetz, R. Transparent Sintered Corundum with High Hardness and Strength. *J. Am. Ceram. Soc.* **2003**, *86*, 12–18.
40. Krell, A.; Klimke, J. Effects of the homogeneity of particle coordination on solid-state sintering of transparent alumina. *J. Am. Ceram. Soc.* **2006**, *89*, 1985–1992, doi:10.1111/j.1551-2916.2006.00985.x.
41. Li, K.; Shapiro, Y.; Li, J.C.M. Scratch test of soda-lime glass. *Acta Mater.* **1998**, *46*, 5569–5578, doi:10.1016/S1359-6454(98)00163-3.
42. Bull, S.J. Failure modes in scratch adhesion testing. *Surf. Coatings Technol.* **1991**, *50*, 25–32, doi:10.1016/0257-8972(91)90188-3.
43. Sato, Y.; Arzakantsyan, M.; Akiyama, J.; Taira, T. Anisotropic Yb:FAP laser ceramics by micro-domain control. *Opt. Mater. Express* **2014**, *4*, 2006, doi:10.1364/ome.4.002006.
44. Nishiyama, N.; Ishikawa, R.; Ohfuji, H.; Marquardt, H.; Kurnosov, A.; Taniguchi, T.; Kim, B.N.; Yoshida, H.; Masuno, A.; Bednarcik, J.; et al. Transparent polycrystalline cubic silicon nitride. *Sci. Rep.* **2017**, *7*, 1–8, doi:10.1038/srep44755.
45. Stuer, M.; Bowen, P.; Cantoni, M.; Pecharroman, C.; Zhao, Z. Nanopore characterization and optical modeling of transparent polycrystalline alumina. *Adv. Funct. Mater.* **2012**, *22*, 2303–2309, doi:10.1002/adfm.201200123.

46. Pabst, W.; Hostaša, J. A closed-form expression approximating the mie solution for the real-in-line transmission of ceramics with spherical inclusions or pores. *Ceram. - Silikaty* **2013**, *57*, 151–161.
47. Lakshmanan, A. *Sintering of ceramics– New Emerging Techniques*; InTech, 2012; ISBN 9789535100171.
48. Nassajpour-Esfahani, A.H.; Emadi, R.; Alhaji, A.; Bahrami, A.; Haftbaradaran-Esfahani, M.R. Towards high strength MgAl₂O₄/Si₃N₄ transparent nanocomposite, using spark plasma sintering. *J. Alloys Compd.* **2020**, *830*, 154588, doi:10.1016/j.jallcom.2020.154588.
49. Huang, C.B.; Lu, T.C.; Lin, L. Bin; Lei, M.Y.; Huang, C.X. A Study on Toughening and Strengthening of Mg-Al Spinel Transparent Ceramics. *Key Eng. Mater.* **2007**, *336–338*, 1207–1210, doi:10.4028/www.scientific.net/kem.336-338.1207.
50. Awaji, H.; Choi, S.M.; Yagi, E. Mechanisms of toughening and strengthening in ceramic-based nanocomposites. *Mech. Mater.* **2002**, *34*, 411–422, doi:10.1016/S0167-6636(02)00129-1.
51. Sheikh, H.; Loghman-Estarki, M.R.; Sharifi, E.M.; Alhaji, A.; Shakeri, J. Toughening of MgAl₂O₄ spinel/ Si₃N₄ nanocomposite fabricated by spark plasma sintering. *Ceram. Int.* **2018**, *44*, 18235–18242, doi:10.1016/j.ceramint.2018.07.033.
52. Mizuta, H.; Oda, K.; Shibasaki, Y.; Maeda, M.; Machida, M.; Ohshima, K. Preparation of High-Strength and Translucent Alumina by Hot Isostatic Pressing. *J. Am. Ceram. Soc.* **1992**, *75*, 469–473, doi:10.1111/j.1151-2916.1992.tb08203.x.
53. Apetz, R.; Van Bruggen, M.P.B. Transparent alumina: A light-scattering model. *J. Am. Ceram. Soc.* **2003**, *86*, 480–486, doi:10.1111/j.1151-2916.2003.tb03325.x.
54. Borrero-López, O.; Ortiz, A.L.; Gledhill, A.D.; Guiberteau, F.; Mroz, T.; Goldman, L.M.; Padture, N.P. Microstructural effects on the sliding wear of transparent magnesium-aluminate spinel. *J. Eur. Ceram. Soc.* **2012**, *32*, 3143–3149, doi:10.1016/j.jeurceramsoc.2012.04.002.
55. Grasso, S.; Hu, C.; Maizza, G.; Kim, B.-N.; Sakka, Y. Effects of Pressure Application Method on Transparency of Spark Plasma Sintered Alumina. **2011**, *1409*, 1405–1409, doi:10.1111/j.1551-2916.2010.04274.x.

56. Roussel, N.; Lallemand, L.; Durand, B.; Guillemet, S.; Ching, J.C.; Fantozzi, G.; Garnier, V.; Bonnefont, G. Effects of the nature of the doping salt and of the thermal pre-treatment and sintering temperature on Spark Plasma Sintering of transparent alumina. *Ceram. Int.* **2011**, *37*, 3565–3573, doi:10.1016/j.ceramint.2011.05.152.
57. Huang, Z.; Deng, J.; Wang, H.; Zhang, Y.; Duan, J.; Tang, Z.; Yang, Y.; He, D.; Qi, J.; Lu, T. A new method for the preparation of transparent Y₂O₃ nanocrystalline ceramic with an average grain size of 20 nm. *Scr. Mater.* **2020**, *182*, 57–61, doi:10.1016/j.scriptamat.2020.02.044.
58. Goldstein, A.; Krell, A.; Burshtein, Z. Transparent Ceramics Wikipedia. *Transparent Ceram.* **2020**, 1–16, doi:10.1002/9781119429524.
59. Bergmann, C.P.; Alegre, P. *Transparent Ceramics*; 2015; ISBN 9783319189550.
60. Esposito, L.; Piancastelli, A.; Miceli, P.; Martelli, S. A thermodynamic approach to obtaining transparent spinel (MgAl₂O₄) by hot pressing. *J. Eur. Ceram. Soc.* **2015**, *35*, 651–661, doi:10.1016/j.jeurceramsoc.2014.09.005.
61. Tanaka, S.; Itatani, K.; Uchida, H.; Aizawa, M. The effect of rare-earth oxide addition on the hot-pressing of magnesium silicon nitride. **2002**, *22*, 777–783.
62. A, Q.G.; Xikun, L.; Tai, Q.; Haitao, Z. Application of Rare Earths in Advanced Ceramic Materials. **2007**, *25*, 281–286.
63. Nishiyama, N.; Taniguchi, T.; Ohfuji, H.; Yoshida, K.; Wakai, F.; Kim, B.N.; Yoshida, H.; Higo, Y.; Holzheid, A.; Beermann, O.; et al. Transparent nanocrystalline bulk alumina obtained at 7.7 GPa and 800 ° C. *Scr. Mater.* **2013**, *69*, 362–365, doi:10.1016/j.scriptamat.2013.05.017.
64. Grasso, S.; Yoshida, H.; Porwal, H.; Sakka, Y.; Reece, M. Highly transparent alpha alumina obtained by low cost high pressure SPS. *Ceram. Int.* **2013**, *39*, 3243–3248, doi:10.1016/j.ceramint.2012.10.012.
65. Joshi, B.; Fu, Z.; Niihara, K.; Lee, S.W. Optical, mechanical and tribological properties of Y₂O₃, Er₂O₃ and Nd₂O₃ doped polycrystalline silicon nitride ceramics. *IOP Conf. Ser. Mater. Sci. Eng.* **2011**, *18*, 3–7, doi:10.1088/1757-899X/18/8/082020.
66. von Helden, S.; Malzbender, J.; Krüger, M. Mechanical properties, wear resistance and

- surface damage of glasses and MgAl₂O₄ spinel ceramic after abrasion and scratch exposure. *Ceram. Int.* **2019**, *45*, 10765–10775, doi:10.1016/j.ceramint.2019.02.150.
67. Grujicic, M.; Bell, W.C.; Pandurangan, B. Design and material selection guidelines and strategies for transparent armor systems. *Mater. Des.* **2012**, *34*, 808–819, doi:10.1016/j.matdes.2011.07.007.
 68. Mccauley, J.W.; Strassburger, E.; Patel, P.; Paliwal, B.; Ramesh, K.T. Experimental Observations on Dynamic Response of Selected Transparent Armor Materials. *Exp. Mech.* **2013**, *53*, 3–29, doi:10.1007/s11340-012-9658-5.
 69. Strassburger, E. Visualization of Impact Damage in Ceramics Using the Edge-On Impact Technique. *Int. J. Appl. Ceram. Technol.* **2004**, *1*, 35–42.
 70. Senf, H.; Strassburger, E.; Rothenhausler, H. Stress wave induced damage and fracture in impacted glasses. *Le J. Phys. IV* **1994**, *4*, 741.
 71. Strassburger, E.; Patel, P.; Mccauley, J.W.; Templeton, D.W. HIGH-SPEED PHOTOGRAPHIC STUDY OF WAVE AND IMPACT DAMAGE IN FUSED SILICA AND USING EDGE-ON IMPACT (EOI) METHOD. **2006**, 1503–1506.
 72. Lyberis, A.; Patriarche, G.; Gredin, P.; Vivien, D.; Mortier, M. Origin of light scattering in ytterbium doped calcium fluoride transparent ceramic for high power lasers. *J. Eur. Ceram. Soc.* **2011**, *31*, 1619–1630, doi:10.1016/J.JEURCERAMSOC.2011.02.038.
 73. Sharma, S.K.; Kumar, B.V.M.; Kim, Y.W. Tribological behavior of silicon carbide ceramics - A review. *J. Korean Ceram. Soc.* **2016**, *53*, 581–596, doi:10.4191/kcers.2016.53.6.581.
 74. Jung, W.K.; Ma, H.J.; Kim, H.N.; Kim, D.K. Transparent ceramics for visible/IR windows: Processing, materials and characterization. *Korean J. Mater. Res.* **2018**, *28*, 551–563, doi:10.3740/MRSK.2018.28.10.551.
 75. Drdlik, D.; Drdlikova, K.; Hadraba, H.; Maca, K. Optical, mechanical and fractographic response of transparent alumina ceramics on erbium doping. *J. Eur. Ceram. Soc.* **2017**, *37*, 4265–4270, doi:10.1016/j.jeurceramsoc.2017.02.043.
 76. Pietruszka, R.; Witkowski, B.S.; Zimowski, S.; Stapinski, T.; Godlewski, M. Tribological study of hafnium dioxide and aluminium oxide films grown by atomic layer deposition on

- glass substrate. *Thin Solid Films* **2020**, *709*, 138191, doi:10.1016/j.tsf.2020.138191.
77. Goldman, L.M.; Twedt, R.; Balasubramanian, S.; Sastri, S. ALON Optical Ceramic Transparencies for Window , Dome and Transparent Armor Applications. *Wind. Dome Technol. Mater.* **2011**, *8016*, 1–14, doi:10.1117/12.886122.
 78. Guzik, M.; Pejchal, J.; Yoshikawa, A.; Ito, A.; Goto, T.; Siczek, M.; Lis, T.; Boulon, G. Structural investigations of Lu₂O₃ as single crystal and polycrystalline transparent ceramic. *Cryst. Growth Des.* **2014**, *14*, 3327–3334, doi:10.1021/cg500225v.
 79. Lu, O.; Mcmillen, C.; Thompson, D.; Tritt, T.; Kolis, J. Hydrothermal Single-Crystal Growth of Lu₂O₃ and Lanthanide-Doped Lu₂O₃. **2011**, 4386–4391.
 80. Taniguchi, T.; Yamaoka, S. Spontaneous nucleation of cubic boron nitride single crystal by temperature gradient method under high pressure. **2001**, *222*, 549–557.
 81. Fukabori, A.; Yanagida, T.; Pejchal, J.; Maeo, S.; Yokota, Y.; Yoshikawa, A.; Ikegami, T.; Moretti, F.; Kamada, K. Optical and scintillation characteristics of Y₂O₃ transparent ceramic. *J. Appl. Phys.* **2010**, *107*, doi:10.1063/1.3330407.
 82. Hou, X.; Zhou, S.; Jia, T.; Lin, H.; Teng, H. Investigation of up-conversion luminescence properties of RE/Yb co-doped Y₂O₃ transparent ceramic (RE=Er, Ho, Pr, and Tm). *Phys. B Condens. Matter* **2011**, *406*, 3931–3937, doi:10.1016/j.physb.2010.10.090.
 83. Nishiyama, N.; Ishikawa, R.; Ohfuji, H.; Marquardt, H.; Kurnosov, A.; Taniguchi, T.; Kim, B.N.; Yoshida, H.; Masuno, A.; Bednarcik, J.; et al. Transparent polycrystalline cubic silicon nitride. *Sci. Rep.* **2017**, *7*, 1–8, doi:10.1038/srep44755.
 84. Mandal, H.; Bressiani, A.H.; Mandal, H. New developments in alpha-SiAlON ceramics. *J. Eur. Ceram. Soc.* **1999**, *19*, 2349–2357.
 85. Su, X.; Wang, P.; Chen, W.; Cheng, Y.; Yan, D. Infrared transmission of hot-pressed Y- and Dy- α -sialon ceramics. *Mater. Lett.* **2004**, *58*, 1985–1988, doi:10.1016/j.matlet.2003.12.020.
 86. Xiong, Y.; Fu, Z.; Wang, H.; Wang, W.; Zhang, J.; Zhang, Q.; Lee, S.W.; Niihara, K. Translucent Mg- α -sialon ceramics prepared by spark plasma sintering. *J. Am. Ceram. Soc.* **2007**, *90*, 1647–1649, doi:10.1111/j.1551-2916.2007.01615.x.
 87. Goldman, L.M.; Hartnett, T.M.; Wahi, J.M.; Ondercin, R.J.; Olson, K. Recent advances in

- Aluminium Oxynitride (ALON) optical ceramic. *Wind. Dome Technol. Mater.* **2001**, 4375, 71–78.
88. Mroz, T.; Goldman, L.M.; Gledhill, A.D.; Li, D.; Padture, N.P. Nanostructured , Infrared-Transparent Magnesium- Aluminate Spinel with Superior Mechanical Properties. *Int. J. Appl. Ceram. Technol.* **2012**, 9, 83–90, doi:10.1111/j.1744-7402.2011.02629.x.
89. Saikko, V.; Keränen, J. Wear simulation of alumina-on-alumina prosthetic hip joints using a multidirectional motion pin-on-disk device. *J. Am. Ceram. Soc.* **2002**, 85, 2785–2791, doi:10.1111/j.1151-2916.2002.tb00529.x.
90. Sung, R.J.; Kim, S.H.; Kusunose, T.; Nakayama, T.; Sekino, T. Mechanical and Wear Properties of Silicon Nitride added with AlN. *Mater. Sci. Forum Trans Tech Publ. Ltd* **2005**, 487, 209–212, doi:10.4028/www.scientific.net/MSF.486-487.209.
91. Kim, J.H.; Venkata Manoj Kumar, B.; Hong, S.H.; Kim, H.D. Fabrication of silicon nitride nanoceramics and their tribological properties. *J. Am. Ceram. Soc.* **2010**, 93, 1461–1466, doi:10.1111/j.1551-2916.2010.03614.x.
92. Li, X.; Xu, Y.; Mao, X.; Zhu, Q.; Xie, J.; Feng, M.; Jiang, B.; Zhang, L. Investigation of optical, mechanical, and thermal properties of ZrO₂-doped Y₂O₃ transparent ceramics fabricated by HIP. *Ceram. Int.* **2017**, 44, 1362–1369, doi:10.1016/j.ceramint.2017.08.204.
93. Zhu, L.; Park, Y.; Gan, L.; Go, S.; Kim, H.; Kim, J.; Ko, J. Fabrication and characterization of highly transparent Er:Y₂O₃ ceramics with ZrO₂ and La₂O₃ additives. *Ceram. Int.* **2017**, 43, 13127–13132, doi:10.1016/j.ceramint.2017.07.004.
94. Korkmaz, E.; Sahin, F. Fabrication of Transparent Yttria Ceramics by Spark Plasma Sintering Fabrication of Transparent Yttria Ceramics by Spark Plasma Sintering. *ACTA Phys. Pol. A* **2020**, 8–11, doi:10.12693/APhysPolA.131.460.
95. Liu, L.; Morita, K.; Suzuki, T.S.; Kim, B.-N. Effect of the Heating Rate on the Spark-Plasma-Sintering (SPS) of Transparent Y₂O₃ Ceramics: Microstructural Evolution, Mechanical and Optical Properties. *Ceramics* **2021**, 4, 56–69, doi:10.3390/ceramics4010006.
96. Composition, A.; Al, M.; Sutorik, A.C.; Gilde, G.; Swab, J.J.; Cooper, C.; Gamble, R.; Shanholtz, E. Transparent Solid Solution Magnesium Aluminate Spinel Polycrystalline Ceramic with the Alumina-Rich Composition MgO·1.2Al₂O₃. *J. Am. Ceram. Soc.* **2012**,

- 643, 636–643, doi:10.1111/j.1551-2916.2011.04798.x.
97. Dericioglu, A.F.; Boccaccini, A.R.; Dlouhy, I.; Kagawa, Y. Effect of Chemical Composition on the Optical Properties and Fracture Toughness of Transparent Magnesium Aluminate Spinel Ceramics. *Mater. Trans.* **2005**, *46*, 996–1003.
 98. Ramisetty, M.; Sastri, S.; Kashalikar, U.; Goldman, L.M.; Nag, N. Transparent polycrystalline cubic spinels protect and defend. *Am. Ceram. Soc. Bull.* **2013**, *92*.
 99. Yang, W.; Hojo, J.; Enomoto, N.; Tanaka, Y.; Inada, M. Influence of Sintering Aid on the Translucency of Spark Plasma-Sintered Silicon Nitride Ceramics. *J. Am. Ceram. Soc.* **2013**, *96*, 2556–2561, doi:10.1111/jace.12370.
 100. Joshi, B.; Fu, Z.; Niihara, K. Fabrication of Translucent Boron Nitride Dispersed Polycrystalline Silicon Nitride Ceramics. **2011**, *20*, doi:10.1088/1757-899X/20/1/012014.
 101. Su, X.; Wang, P.; Chen, W.; Zhu, B.; Cheng, Y.; Yan, D. Translucent alpha-Sialon Ceramics by Hot Pressing. *J. Am. Ceram. Soc.* **2010**, *32*, 730–732.
 102. Kaminskii, A.A.; Akchurin, M.S.; Becker, P.; Ueda, K.; Bohat, L. Mechanical and optical properties of Lu₂O₃ host-ceramics for Ln³⁺ lasants. *Laser Phys. Lett.* **2008**, *5*, 300–303, doi:10.1002/lapl.200710128.
 103. Munro, R.G. Elastic moduli data for polycrystalline ceramics. *NISTIR, Gaithersburg, Maryl.* **2002**, *20899*, 6853.
 104. Speyer, R.F.; Sayir, A. *Sintering, thermal conductivity, optical and lasing properties of doped-Lu₂O₃ fibrous transparent ceramics*; 2014;
 105. Pavlik, A.; Ushakov, S. V.; Navrotsky, A.; Benmore, C.J.; Weber, R.J.K. Structure and thermal expansion of Lu₂O₃ and Yb₂O₃ to the melting temperatures. *J. Nucl. Mater.* **2017**, *495*, 1–25.
 106. Liang, A.; Liu, Y.; Shi, L.; Lei, L.; Zhang, F.; Hu, Q.; He, D. Melting temperature of diamond and cubic boron nitride at 15 gigapascals. *Phys. Rev. Res.* **2019**, *1*, 033090, doi:10.1103/PHYSREXRESEARCH.1.033090/FIGURES/17/MEDIUM.
 107. Soltani, A.; Talbi, A.; Mortetb, V.; Benmoussa, A.; Zhang, W.J.; Gerbedoen, J.C.; De Jaeger, J.C.; Gokarna, A.; Haenen, K.; Wagner, P. Diamond and cubic boron nitride: Properties, growth and applications. *AIP Conf. Proc.* **2010**, *1292*, 191–196,

doi:10.1063/1.3518293.

108. Akaishi, M.; Satoh, T.; Ishii, M.; Taniguchi, T. Synthesis of translucent sintered cubic boron nitride. *J. Mater. Sci. Lett.* **1993**, *12*, 1883–1885.
109. Tian, Y.; Xu, B.; Yu, D.; Ma, Y.; Wang, Y.; Jiang, Y.; Hu, W.; Tang, C.; Gao, Y. Ultrahard nanotwinned cubic boron nitride. *Nature* **2013**, *493*, 385–388, doi:10.1038/nature11728.
110. Sei, H. Effect of small amounts of hydrochloric acid on the synthesis of translucent sintered cubic BN. *Diam. Relat. Mater.* **1993**, *2*, 1160–1163.
111. Ghanizadeh, S.; Grasso, S.; Ramanujam, P.; Vaidhyanathan, B.; Binner, J.; Brown, P.; Goldwasser, J. Improved transparency and hardness in α -alumina ceramics fabricated by high-pressure SPS of nanopowders. *Ceram. Int.* **2017**, *43*, 275–281, doi:10.1016/j.ceramint.2016.09.150.
112. Chen, D.; Jordan, H.; Gell, M. Pressureless sintering of translucent MgO ceramics. *Scr. Mater.* **2008**, *59*, 757–759, doi:10.1016/j.scriptamat.2008.06.007.
113. Liu, L.; Morita, K.; Suzuki, T.S. Effect of the Heating Rate on the Spark-Plasma-Sintering (SPS) of Transparent Y₂O₃ Ceramics : Microstructural Evolution, Mechanical and Optical Properties. *Ceramics* **2021**, 56–69.
114. Fleischman, Z.D.; Blair, V.L.; Ku, N.; Merkle, L.D. Dual-phase Er:Y₂O₃/MgO nanocomposites for mid-Infrared solid state lasers. <https://doi.org/10.1117/12.2311470> **2018**, *10637*, 116–126, doi:10.1117/12.2311470.
115. Wang, S.F.; Zhang, J.; Luo, D.W.; Gu, F.; Tang, D.Y.; Dong, Z.L.; Tan, G.E.B.; Que, W.X.; Zhang, T.S.; Li, S.; et al. Transparent ceramics: Processing, materials and applications. *Prog. Solid State Chem.* 2013.
116. Goldstein, A.; Goldenberg, A.; Hefetz, M. Influence of powder type on the densification of transparent MgAl₂O₄ spinel. *Ceram. Mater. Components Energy Environ. Appl.* **2009**, 579–84.
117. Merac, M.R. du; Kleebe, H.-J.; Muller, M.M.; Reimanis, I.E. Fifty Years of Research and Development Coming to Fruition: Unraveling the Complex Interactions during Processing of Transparent Magnesium Aluminate (MgAl₂O₄) Spinel. *J. Am. Ceram. Soc.* **2013**, *96*, 3341–3365, doi:10.1111/jace.12637.

118. Balabanov, S.S.; Yavetskiy, R.P.; Belyaev, A. V; Gavrishchuk, E.M.; Drobotenko, V. V Fabrication of transparent MgAl₂O₄ ceramics by hot-pressing of sol-gel-derived nanopowders. *Ceram. Int.* **2015**, *41*, 13366–13371, doi:10.1016/j.ceramint.2015.07.123.
119. Esposito, L.; Piancastelli, A.; Martelli, S. Production and characterization of transparent MgAl₂O₄ prepared by hot pressing. *J. Eur. Ceram. Soc.* **2013**, *33*, 737–747, doi:10.1016/j.jeurceramsoc.2012.10.013.
120. Hostaša, J.; Esposito, L.; Alderighi, D.; Pirri, A. Preparation and characterization of Yb-doped YAG ceramics. *Opt. Mater. (Amst)*. **2013**, *35*, 798–803, doi:10.1016/j.optmat.2012.05.028.
121. Hostaša, J.; Biasini, V.; Piancastelli, A.; Vannini, M.; Toci, G. Layered Yb:YAG ceramics produced by two different methods: processing, characterization, and comparison. *Opt. Eng.* **2016**, *55*, 087104, doi:10.1117/1.oe.55.8.087104.
122. Trunec, M.; Kastyl, J.; Stastny, P.; Hildebrandt, S. Processing of large and complex-shaped fine-grained alumina bodies with high transparency. *J. Eur. Ceram. Soc.* **2021**, *41*, 2016–2022, doi:10.1016/j.jeurceramsoc.2020.10.065.
123. Feng, Z.; Qi, J.; Lu, T. Highly-transparent AlON ceramic fabricated by tape-casting and pressureless sintering method. *J. Eur. Ceram. Soc.* **2020**, *40*, 1168–1173, doi:10.1016/j.jeurceramsoc.2019.11.065.
124. Boulesteix, R.; Goldstein, A.; Perrière, C.; Maître, A.; Katz, M.; Coureau, C.; Sallé, C. Transparent ceramics green-microstructure optimization by pressure slip-casting: Cases of YAG and MgAl₂O₄. *J. Eur. Ceram. Soc.* **2021**, *41*, 2085–2095, doi:10.1016/j.jeurceramsoc.2020.11.003.
125. Hostaša, J.; Schwentenwein, M.; Toci, G.; Esposito, L.; Brouczek, D.; Piancastelli, A.; Pirri, A.; Patrizi, B.; Vannini, M.; Biasini, V. Transparent laser ceramics by stereolithography. *Scr. Mater.* **2020**, *187*, 194–196, doi:10.1016/j.scriptamat.2020.06.006.
126. Li, H.; Song, L.; Sun, J.; Ma, J.; Shen, Z. Asynchronous densification of zirconia ceramics formed by stereolithographic additive manufacturing. *J. Eur. Ceram. Soc.* **2021**, *41*, 4666–4670, doi:10.1016/j.jeurceramsoc.2021.02.052.
127. Zhu, L.L.; Park, Y.J.; Gan, L.; Go, S. Il; Kim, H.N.; Kim, J.M.; Ko, J.W. Fabrication of transparent MgAl₂O₄ from commercial nanopowders by hot-pressing without sintering

- additive. *Mater. Lett.* **2018**, *219*, 8–11, doi:10.1016/j.matlet.2018.02.010.
128. Gan, L.; Park, Y.J.; Zhu, L.L.; Kim, H.N.; Ko, J.W.; Kim, H.D. Optical and thermo-mechanical properties of fine-grained transparent yttria ceramics fabricated by hot-press sintering for infrared window applications. *J. Eur. Ceram. Soc.* **2018**, *38*, 4064–4069, doi:10.1016/j.jeurceramsoc.2018.04.056.
129. Zhang, R.; Wang, H.; Tian, M.; Liu, M.; Wang, H. Pressureless reaction sintering and hot isostatic strength of transparent MgAlON ceramic with high strength Rongshi. *Ceram. Int.* **2018**, doi:10.1016/j.ceramint.2018.06.203.
130. Zhang, H.; Wang, H.; Gu, H.; Zong, X.; Tu, B.; Xu, P.; Wang, B.; Wang, W.; Liu, S.; Fu, Z. Preparation of transparent MgO.1.8Al₂O₃ spinel ceramics by aqueous gelcasting, presintering and hot isostatic pressing. *J. Eur. Ceram. Soc.* **2018**, *38*, 4057–4063, doi:10.1016/j.jeurceramsoc.2018.04.057.
131. Carloni, D.; Zhang, G.; Wu, Y. Transparent alumina ceramics fabricated by 3D printing and vacuum sintering. *J. Eur. Ceram. Soc.* **2021**, *41*, 781–791, doi:10.1016/j.jeurceramsoc.2020.07.051.
132. Safronova, N.A.; Kryzhanovska, O.S.; Dobrotvorska, M. V.; Balabanov, A.E.; Tolmachev, V. V.; Yavetskiy, R.P.; Parkhomenko, S. V.; Brodskii, R.Y.; Baumer, V.N.; Kosyanov, D.Y.; et al. Influence of sintering temperature on structural and optical properties of Y₂O₃–MgO composite SPS ceramics. *Ceram. Int.* **2020**, *46*, 6537–6543, doi:10.1016/j.ceramint.2019.11.137.
133. Shahbazi, H.; Shokrollahi, H.; Tataei, M. Gel-Casting of transparent magnesium aluminate spinel ceramics fabricated by spark plasma sintering (SPS). *Ceram. Int.* **2017**, doi:10.1016/j.ceramint.2017.12.088.
134. Kerbart, G.; Harnois, C.; Bilot, C.; Marinel, S. Pressure-assisted microwave sintering: A rapid process to sinter submicron sized grained MgAl₂O₄ transparent ceramics. *J. Eur. Ceram. Soc.* **2019**, *39*, 2946–2951, doi:10.1016/j.jeurceramsoc.2019.03.046.
135. Han, Y.; Feng, J.; Zhou, J.; Li, F.; Huang, X.; Wang, L.; Liu, G.; Cheng, J. Heating parameter optimization and optical properties of Nd:YAG transparent ceramics prepared by microwave sintering. *Ceram. Int.* **2020**, *46*, 20847–20855, doi:10.1016/j.ceramint.2020.05.117.

136. Godec, Y. Le; Courac, A.; Solozhenko, V.; Godec, Y. Le; Courac, A.; Solozhenko, V.; Godec, Y. Le; Courac, A.; Solozhenko, V.L. High-pressure synthesis of superhard and ultrahard materials To cite this version : HAL Id : hal-02331183 High-pressure synthesis of superhard and ultrahard materials. *J. Appl. Phys.* **2019**, *126*, 151102.
137. Salke, N.P.; Xia, K.; Fu, S.; Zhang, Y.; Greenberg, E.; Prakapenka, V.B.; Liu, J.; Sun, J.; Lin, J. Tungsten Hexanitride with Single-Bonded Armchairlike Hexazine Structure at High Pressure HPSTAR. *Phys. Rev. Lett.* **2021**, *126*, 65702, doi:10.1103/PhysRevLett.126.065702.
138. Krell, A.; Klimke, J.; Hutzler, T. Transparent compact ceramics: Inherent physical issues. *Opt. Mater. (Amst)*. **2009**, *31*, 1144–1150, doi:10.1016/j.optmat.2008.12.009.
139. Sikalidis, C. *Advances in ceramics- Characterization, raw materials, processing, properties, degradation and healing*; 2001; ISBN 9789533075044.
140. Pappas, J.M.; Dong, X. Direct 3D printing of silica doped transparent magnesium aluminate spinel ceramics. *Materials (Basel)*. **2020**, *13*, 1–22, doi:10.3390/ma13214810.
141. Gledhill, A.D.; Li, D.; Mroz, T.; Goldman, L.M.; Padture, N.P. Strengthening of transparent spinel/Si₃N₄ nanocomposites. *Acta Mater.* **2012**, *60*, 1570–1575, doi:10.1016/j.actamat.2011.11.053.
142. van de Hulst, H.C. *Light Scattering by Small Particles*; John Wiley and Sons: New York, 1957;
143. Basu, B.; Kalin, M.; Kumar, B. *Friction and wear of ceramics: Principles and Case Studies*; 2020; ISBN 9781119538387.
144. Basu, B.; Kalin, M. *Tribology of Ceramics and Composites*; 2011; ISBN 9780470522639.
145. Lines, M.E.; Glass, A.M. *Principles and Applications of Tribology*; 1977; Vol. 10; ISBN 3527305521.
146. Ganesh, I. A review on magnesium aluminate (MgAl₂O₄) spinel : synthesis , processing and applications. *Int. Mater. Rev.* **2013**, *58*, 63–112, doi:10.1179/1743280412Y.0000000001.
147. Wollmershauser, J.A.; Feigelson, B.N.; Gorzkowski, E.P.; Ellis, C.T.; Goswami, R.; Qadri, S.B.; Tischler, J.G.; Kub, F.J.; Everett, R.K. An extended hardness limit in bulk

- nanoceramics. *Acta Mater.* **2014**, *69*, 9–16, doi:10.1016/j.actamat.2014.01.030.
148. Reimanis, I.; Kleebe, H.J. A review on the sintering and microstructure development of transparent spinel (MgAl₂O₄). *J. Am. Ceram. Soc.* **2009**, *92*, 1472–1480, doi:10.1111/j.1551-2916.2009.03108.x.
 149. Kim, B.N.; Morita, K.; Lim, J.H.; Hiraga, K.; Yoshida, H. Effects of preheating of powder before spark plasma sintering of transparent MgAl₂O₄ spinel. *J. Am. Ceram. Soc.* **2010**, *93*, 2158–2160, doi:10.1111/j.1551-2916.2010.03699.x.
 150. Zou, Y.; He, D.; Wei, X.; Yu, R.; Lu, T.; Chang, X.; Wang, S.; Lei, L. Nanosintering mechanism of MgAl₂O₄ transparent ceramics under high pressure. *Mater. Chem. Phys.* **2010**, *123*, 529–533, doi:10.1016/J.MATCHEMPHYS.2010.05.009.
 151. Sokol, M.; Kalabukhov, S.; Dariel, M.P.; Frage, N. High-pressure spark plasma sintering (SPS) of transparent polycrystalline magnesium aluminate spinel (PMAS). *J. Eur. Ceram. Soc.* **2014**, *34*, 4305–4310, doi:10.1016/J.JEURCERAMSOC.2014.07.022.
 152. Morita, K.; Kim, B.N.; Hiraga, K.; Yoshida, H. Fabrication of transparent MgAl₂O₄ spinel polycrystal by spark plasma sintering processing. *Scr. Mater.* **2008**, *58*, 1114–1117, doi:10.1016/J.SCRIPTAMAT.2008.02.008.
 153. Villalobos, G.R.; Sanghera, J.S.; Aggarwal, I.D. Degradation of magnesium aluminum spinel by lithium fluoride sintering aid. *J. Am. Ceram. Soc.* **2005**, *88*, 1321–1322, doi:10.1111/j.1551-2916.2005.00209.x.
 154. Tsukuma, K.; Mgal, O. Transparent MgAl₂O₄ spinel ceramics produced by HIP post sintering. *J. Ceram. Soc. Japan* **2006**, *806*, 802–806.
 155. Jan Hostasa, Francesco Picelli, Sona Hříbalova, V.N. Sintering aids , their role and behaviour in the production of transparent ceramics. *Open Ceram.* **2021**, *7*, doi:10.1016/j.oceram.2021.100137.
 156. Bratton, R.J. Translucent Sintered MgAl₂O₄. *J. Am. Ceram. Soc.* **1974**, *57*, 283–286.
 157. Maca, K.; Trunec, M.; Chmelik, R. PROCESSING AND PROPERTIES OF FINE-GRAINED TRANSPARENT MgAl₂O₄ CERAMICS. **2007**, *51*, 94–97.
 158. Nečina, V.; Pabst, W. Comparison of the effect of different alkali halides on the preparation of transparent MgAl₂O₄ spinel ceramics via spark plasma sintering (SPS). *J. Eur. Ceram.*

- Soc.* **2020**, *40*, 6043–6052, doi:10.1016/j.jeurceramsoc.2020.06.056.
159. Nečina, V.; Pabst, W. Grain growth of MgAl₂O₄ ceramics with LiF and NaF addition. *Open Ceram.* **2021**, *5*, 1–6, doi:10.1016/j.oceram.2021.100078.
 160. Harris, D.C. *Materials for Infrared Windows and Domes*; 1999; ISBN 0819434825.
 161. Steinbrech, R.W. R-Curve Behavior of Ceramics. *Fract. Mech. Ceram.* **1992**, *9*, 187–208, doi:10.1007/978-1-4615-3350-4_14.
 162. Shi, Z.; Zhao, Q.; Guo, B.; Ji, T.; Wang, H. A review on processing polycrystalline magnesium aluminate spinel (MgAl₂O₄): Sintering techniques, material properties and machinability. *Mater. Des.* **2020**, *193*, 108858, doi:10.1016/j.matdes.2020.108858.
 163. PAULING, L.; HENDRICK, S.B. Crystal structure of Hematite and Corundum. **1925**, *346*.
 164. Krell, A.; Baur, G.; Dahne, C. Transparent sintered sub-micro meter Al₂O₃ with IR transmissivity equal to sapphire. *Wind. Dome Technol.* **2003**, *5078*, 199–207.
 165. Trunec, M.; Maca, K.; Chmelik, R. Polycrystalline alumina ceramics doped with nanoparticles for increased transparency. *J. Eur. Ceram. Soc.* **2015**, *35*, 1001–1009, doi:10.1016/j.jeurceramsoc.2014.09.041.
 166. Stuer, M.; Zhao, Z.; Aschauer, U.; Bowen, P. Transparent polycrystalline alumina using spark plasma sintering : Effect of Mg , Y and La doping. *J. Eur. Ceram. Soc.* **2010**, *30*, 1335–1343, doi:10.1016/j.jeurceramsoc.2009.12.001.
 167. Ferna, A.; Mene, J.L.; Torrecillas, R.; Sua, M. Grain growth control and transparency in spark plasma sintered self-doped alumina materials. *Scr. Mater.* **2009**, *61*, 931–934, doi:10.1016/j.scriptamat.2009.07.026.
 168. Mccauley, J.W.; Patel, P.; Chen, M.; Gilde, G.; Strassburger, E.; Paliwal, B.; Ramesh, K.T.; Dandekar, D.P. AlON : A brief history of its emergence and evolution. *J. Eur. Ceram. Soc.* **2009**, *29*, 223–236, doi:10.1016/j.jeurceramsoc.2008.03.046.
 169. Ish-Shalom, M. Formation of aluminium oxynitride by carbothermal reduction of aluminium oxide in nitrogen. *J. Mater. Sci. Lett.* **1982**, *1*, 147–149.
 170. Hartnett, T.M.; Bernstein, S.D.; Maguire, E.A.; Tustison, R.W. Optical properties of ALON (aluminum oxynitride). *Wind. Dome Technol. Mater.* **1997**, *3060*, 284–295,

doi:10.1117/12.277053.

171. Su, M.; Zhou, Y.; Wang, K.; Yang, Z.; Cao, Y.; Hong, M. Highly transparent AlON sintered from powder synthesized by direct nitridation. *J. Eur. Ceram. Soc.* **2015**, *35*, 1173–1178, doi:10.1016/j.jeurceramsoc.2014.10.036.
172. Suh, M.S.; Chae, Y.H.; Kim, S.S. Friction and wear behavior of structural ceramics sliding against zirconia. *Wear* **2008**, *264*, 800–806, doi:10.1016/j.wear.2006.12.079.
173. Bull, S.J.; Kingswell, R.; Scott, K.T. The sliding wear of plasma sprayed alumina. *Surf. Coatings Technol.* **1996**, *82*, 218–225, doi:10.1016/0257-8972(95)02641-X.
174. Zhao, X.J.; Guo, L.; Cai, Z.Y.; Xiao, L.R.; Zhao, Z.W.; Li, G.; Han, J.; Ru, H.Q.; Zhang, N.; Chen, D.L. *SiC and ZrN nano-particulate reinforced AlON composites: Preparation, mechanical properties and toughening mechanisms*; 2016; Vol. 42; ISBN 0731888774.
175. Liu, X.; Wang, H.; Tu, B.; Wang, W.; Fu, Z. Highly transparent Mg_{0.27}Al_{2.58}O_{3.73}N_{0.27} ceramic prepared by pressureless sintering. *J. Am. Ceram. Soc.* **2014**, *97*, 63–66, doi:10.1111/jace.12711.
176. Ma, B.; Wang, Y.; Zhang, W.; Chen, Q. Pressureless sintering and fabrication of highly transparent MgAlON ceramic from the carbothermal powder. *J. Alloys Compd.* **2018**, *745*, 617–623, doi:10.1016/j.jallcom.2018.02.254.
177. Zhang, R.; Wang, Y.; Tian, M.; Wang, H. Highly transparent LiAlON ceramic prepared by reaction sintering and post hot isostatic pressing. *J. Eur. Ceram. Soc.* **2018**, *38*, 5252–5256, doi:10.1016/j.jeurceramsoc.2018.07.053.
178. Clay, D.; Poslusny, D.; Flinders, M.; Jacobs, S.D.; Cutler, R.A. Effect of LiAl₅O₈ additions on the sintering and optical transparency of LiAlON. *J. Eur. Ceram. Soc.* **2006**, *26*, 1351–1362, doi:10.1016/j.jeurceramsoc.2005.01.056.
179. Maguire, E.A.; Hartnett, T.M.; Gentilman, R.L. Method of producing aluminum oxynitride having improved optical characteristics 1987.
180. Hartnett, T.M.; Gentilman, R.L.; Maguire, E.A. Aluminum Oxynitride Having Improved Optical Characteristics and Method of Manufacture 1984.
181. Gentilman, R.L.; Maguire, E.A.; Dolhert, L.E. Transparent Aluminum Oxynitride and Method of Manufacture 1984.

182. Yang, P.; Gai, S.; Liu, Y.; Wang, W.; Li, C.; Lin, J. Uniform Hollow Lu₂O₃ : Ln (Ln =Eu³⁺, Tb³⁺) Spheres : Facile Synthesis and Luminescent Properties. *Am. Chem. Soc.* **2011**, 2182–2190.
183. Loiko, P.A.; Yumashev, K. V.; Schödel, R.; Peltz, M.; Liebald, C.; Mateos, X.; Deppe, B.; Kränkel, C. Thermo-optic properties of Yb:Lu₂O₃ single crystals. *Appl. Phys. B Lasers Opt.* **2015**, *120*, 601–607, doi:10.1007/s00340-015-6171-4.
184. Li, C.; Zhang, F.; Wang, X.; Rao, X. Repeated nanoscratch and double nanoscratch tests of Lu₂O₃ transparent ceramics: Material removal and deformation mechanism, and theoretical model of penetration depth. *J. Eur. Ceram. Soc.* **2018**, *38*, 705–718, doi:10.1016/j.jeurceramsoc.2017.09.028.
185. Lawn, B. Fracture of brittle solids. *Cambridge Solid State Sci. Ser.* **2010**.
186. An, L.; Ito, A.; Goto, T. Fabrication of transparent lutetium oxide by spark plasma sintering. *J. Am. Ceram. Soc.* **2011**, *94*, 695–698, doi:10.1111/j.1551-2916.2010.04145.x.
187. Kijko, V.S.; Maksimov, R.N.; Shitov, V.A.; Demakov, S.L.; Yurovskikh, A.S. Sintering of transparent Yb-doped Lu₂O₃ ceramics using nanopowder produced by laser ablation method. *J. Alloys Compd.* **2015**, *643*, 207–211, doi:10.1016/j.jallcom.2015.04.127.
188. Pirri, A.; Toci, G.; Patrizi, B.; Vannini, M. An Overview on Yb-Doped Transparent Polycrystalline Sesquioxide Laser Ceramics. *IEEE J. Sel. Top. Quantum Electron.* **2018**, *24*, 1–8, doi:10.1109/JSTQE.2018.2799003.
189. Search, H.; Journals, C.; Contact, A.; Iopscience, M.; Address, I.P. Measurement of the Optical Constants of Yttrium Oxide. *Japenese J. Appl. Phys.* **1968**, *7*, 404–408.
190. Id, O.; Id, O.; Furuse, H.; Nakasawa, S.; Yoshida, H.; Morita, K.; Suzuki, T.S.; Kim, B.; Sakka, Y.; Hiraga, K.; et al. Transparent ultrafine Yb³⁺:Y₂O₃ laser ceramics fabricated by spark plasma sintering. *Am. Ceram. Soc.* **2018**, 0–2, doi:10.1111/ijlh.12426.
191. Marder, R.; Chaim, R.; Estournès, C. Grain growth stagnation in fully dense nanocrystalline Y₂O₃ by spark plasma sintering. **2010**, *527*, 1577–1585, doi:10.1016/j.msea.2009.11.009.
192. Maksimov, R.N.; Esposito, L.; Hostaša, J.; Shitov, V.A.; Belov, P.A. Densification and phase transition of Yb-doped Lu₂O₃ nanoparticles synthesized by laser ablation. *Mater. Lett.* **2016**, *185*, 396–398, doi:10.1016/j.matlet.2016.09.038.

193. Ikegami, T.; Li, J.G.; Mori, T.; Moriyoshi, Y. Fabrication of transparent yttria ceramics by the low-temperature synthesis of yttrium hydroxide. *J. Am. Ceram. Soc.* **2002**, *85*, 1725–1729, doi:10.1111/j.1151-2916.2002.tb00342.x.
194. Jin, L.; Zhou, G.; Shimai, S.; Zhang, J.; Wang, S. ZrO₂-doped Y₂O₃ transparent ceramics via slip casting and vacuum sintering. *J. Eur. Ceram. Soc.* **2010**, *30*, 2139–2143, doi:10.1016/j.jeurceramsoc.2010.04.004.
195. Zhang, J.; An, L.; Liu, M.; Shimai, S.; Wang, S. Sintering of Yb³⁺:Y₂O₃ transparent ceramics in hydrogen atmosphere. *J. Eur. Ceram. Soc.* **2009**, *29*, 305–309, doi:10.1016/j.jeurceramsoc.2008.03.006.
196. RHODES, W.H. Controlled Transient Solid Second-Phase Sintering of Yttria. *J. Am. Ceram. Soc.* **1981**, *64*, 13–19, doi:10.1111/j.1151-2916.1981.tb09551.x.
197. Eilers, H. Fabrication, optical transmittance, and hardness of IR-transparent ceramics made from nanophase yttria. *J. Eur. Ceram. Soc.* **2007**, *27*, 4711–4717, doi:10.1016/j.jeurceramsoc.2007.04.006.
198. BLAIR, V.L.; FLEISCHMAN, Z.D.; MERKLE, L.D.; KU, N.; MOOREHEAD, C.A. Co-precipitation of rare-earth-doped Y₂O₃ MgO nanocomposites for mid-infrared solid-state lasers. *Appl. Opt.* **2017**, *56*, 154–158, doi:10.7868/s0002337x14090048.
199. Safronova, N.A.; Yavetskiy, R.P.; Kryzhanovska, O.S.; Dobrotvorska, M. V.; Balabanov, A.E.; Vorona, I.O.; Tolmachev, V.; Baumer, V.N.; Matolínová, I.; Kosyanov, D.Y.; et al. A novel IR-transparent Ho³⁺:Y₂O₃–MgO nanocomposite ceramics for potential laser applications. *Ceram. Int.* **2021**, *47*, 1399–1406, doi:10.1016/j.ceramint.2020.08.263.
200. Ahmadi, B.; Razavi, S.; Ahsanzadeh-vadeqani, M.; Barekat, M. Mechanical and optical properties of spark plasma sintered transparent Y₂O₃ ceramics. *Ceram. Int.* **2016**, *42*, 17081–17088, doi:10.1016/j.ceramint.2016.07.218.
201. Serivalsatit, K.; Kokuoz, B.; Yazgan-Kokuoz, B.; Kennedy, M.; Ballato, J. Synthesis, processing, and properties of submicrometer-grained highly transparent yttria ceramics. *J. Am. Ceram. Soc.* **2010**, *93*, 1320–1325, doi:10.1111/j.1551-2916.2010.03601.x.
202. Solozhenko, V.L.; Kurakevych, O.O.; Godec, Y. Le Creation of Nanostructures by Extreme Conditions : High- Pressure Synthesis of Ultrahard Nanocrystalline Cubic Boron Nitride. *Adv. Mater.* **2012**, *24*, 1540–1544, doi:10.1002/adma.201104361.

203. Dubrovinskaia, N.; Dubrovinsky, L. Controversy about ultrahard nanotwinned cBN. *Nature* **2013**, *502*, E1–E2, doi:10.1038/nature12620.
204. Harris, T.K.; Brookes, E.J.; Taylor, C.J. The effect of temperature on the hardness of polycrystalline cubic boron nitride cutting tool materials. *Int. J. Refract. Metals Hard Mater.* **2004**, *22*, 105–110, doi:10.1016/j.ijrmhm.2004.01.004.
205. Taniguchi, T.; Akaishi, M.; Yamaoka, S. Sintering of cubic boron nitride without additives at 7.7 GPa and above 2000 C. *J. Mater. Res.* **2000**, *14*, 162–169.
206. Hooper, R.M.; Shakib, J.I.; Brookes, C.A. Microstructure and wear of TiC-cubic BN tools. *Mater. Sci. Eng.* **1988**, *105–106*, 429–433, doi:10.1016/0025-5416(88)90727-6.
207. Hostas, J.; Silvestroni, L.; Piancastelli, A.; Sciti, D.; Esposito, L.; Martino, D. Di; Spa, M.I.; Km, V.T. Slip Casting of a Si₃N₄-Based System. *Int. J. Appl. Ceram. Technol.* **2012**, *9*, 246–258, doi:10.1111/j.1744-7402.2011.02718.x.
208. Ding, S.; Zeng, Y.; Jiang, D. Oxidation bonding of porous silicon nitride ceramics with high strength and low dielectric constant. *Mater. Lett.* **2007**, *61*, 2277–2280, doi:10.1016/j.matlet.2006.08.067.
209. Qi, G.; Zhang, C.; Hu, H. High strength three-dimensional silica fiber reinforced silicon nitride-based composites via polyhydridomethylsilazane pyrolysis. *Ceram. Int.* **2007**, *33*, 891–894, doi:10.1016/j.ceramint.2006.01.018.
210. Riley, F.L. Silicon Nitride and Related Materials. *J. Am. Ceram. Soc.* **2000**, *65*, 245–265.
211. A.Ziegler; C.Idrobo, J.; Cinibulk, M.K.; C.Kisielowski; Browning, N.D.; Ritchie, R.O. Interface Structure and Atomic Bonding Characteristics in Silicon Nitride Ceramics. *Science (80-)*. **2014**, *306*, 1768–70, doi:10.1126/science.1104173.
212. Pezzotti, G.; Okamoto, T.; Miyamoto, Y. Hot Isostatic Press Sintering and Properties of Silicon Nitride without Additives. *J. Am. Ceram. Soc.* **1989**, *60*, 1656–1660.
213. Dante, R.C.; Kajdas, C.K. A review and a fundamental theory of silicon nitride tribochemistry. *Wear* **2012**, *288*, 27–38, doi:10.1016/j.wear.2012.03.001.
214. Philipp, H.R. Optical Properties of Silicon Nitride. *J. Electrochem. Soc.* **1973**, *120*, 0–5.
215. Mao, X.; Shimai, S.; Dong, M.; Wang, S. Gelcasting and pressureless sintering of

- translucent alumina ceramics. *J. Am. Ceram. Soc.* **2008**, *91*, 1700–1702, doi:10.1111/j.1551-2916.2008.02328.x.
216. Mouzon, J.; Glowacki, E.; Odén, M. Comparison between slip-casting and uniaxial pressing for the fabrication of translucent yttria ceramics. *J. Mater. Sci.* **2008**, *43*, 2849–2856, doi:10.1007/s10853-007-2261-y.
217. Yang, Z.; Wang, H.; Min, X.; Wang, W.; Fu, Z.; Lee, S.W.; Niihara, K. Translucent Li- α -sialon ceramics prepared by spark plasma sintering. *J. Am. Ceram. Soc.* **2010**, *93*, 3549–3551, doi:10.1111/j.1551-2916.2010.04081.x.
218. Ye, F.; Liu, C.; Liu, L.; Zhou, Y. Optical properties of in situ toughened ScLu- α -SiAlON. *Scr. Mater.* **2009**, *61*, 982–984, doi:10.1016/j.scriptamat.2009.08.010.
219. Xue, J.; Liu, Q.; Fang, M.; Ma, L.; Xiu, T.; Gui, L. Effects of process on microstructure and properties of translucent Dy- α -SiAlON sintered at lower temperatures. *J. Ceram. Soc. Japan* **2008**, *116*, 822–824, doi:10.2109/jcersj2.116.822.
220. Pechenik, A.; Piermarini, G.J.; Danforth, S.C. Fabrication of Transparent Silicon Nitride from Nanosize Particles. *J. Am. Ceram. Soc.* **1992**, *75*, 3283–3288, doi:10.1111/j.1151-2916.1992.tb04422.x.
221. Singh, J.; Bansal, N.P.; Kriven, W.M. *Advances in Ceramic Matrix Composites X*; 2005; ISBN 6147945890.
222. Yang, W.W.; Inada, M.; Tanaka, Y.; Enomoto, N.; Hojo, J. Fabrication of translucent silicon nitride ceramics with various sintering aids. *Int. J. Nanotechnology* **2013**, *10*, 119–125.
223. Zhang, W. A review of tribological properties for boron carbide ceramics. *Prog. Mater. Sci.* **2020**, 100718, doi:10.1016/j.pmatsci.2020.100718.
224. Tokariev, O.; Schnetter, L.; Beck, T.; Malzbender, J. Grain size effect on the mechanical properties of transparent spinel ceramics. *J. Eur. Ceram. Soc.* **2013**, *33*, 749–757, doi:10.1016/j.jeurceramsoc.2012.09.024.
225. Marshall, D.B.; Lawn, B.R.; Evans, A.G. Elastic/Plastic Indentation Damage in Ceramics: The Lateral Crack System. *J. Am. Ceram. Soc.* **1981**, *65*, 6.
226. Lawn, B.R.; Padture, N.P.; Guiberteau, F.; Cai, H. A model for microcrack initiation and

- propagation beneath hertzian contacts in polycrystalline ceramics. *Acta Metall. Mater.* **1994**, *42*, 1683–1693, doi:10.1016/0956-7151(94)90378-6.
227. Tewari, A.; Basu, B.; Bordia, R.K. Model for fretting wear of brittle ceramics. *Acta Mater.* **2009**, *57*, 2080–2087, doi:10.1016/j.actamat.2009.01.013.
228. Hsu, S.M.; Shen, M. Wear prediction of ceramics. *Wear* **2004**, *256*, 867–878, doi:10.1016/J.WEAR.2003.11.002.
229. Lee, S.C.; Cheng, H.S. On the relation of load to average gap in the contact between surfaces with longitudinal roughness. *Tribol. Trans.* **1992**, *35*, 523–529, doi:10.1080/10402009208982151.
230. Archard, J.F. The temperature of rubbing surfaces. *Wear* **1959**, *2*, 438–455, doi:10.1016/0043-1648(59)90159-0.
231. GRESKOVICH, C. Preparation of High-Density Si₃N₄ by a Gas-Pressure Sintering Process 1981.
232. MUNIR, Z.A.; ANSELMINI-TAMBURINI, U. The effect of electric field and pressure on the synthesis and consolidation of materials: A review of the spark plasma sintering method. *J. Mater. Sci.* **2006**, *1*, 763–777, doi:10.1007/s10853-006-6555-2.
233. Quach, D. V; Avila-paredes, H.; Kim, S.; Martin, M.; Munir, Z.A. Pressure effects and grain growth kinetics in the consolidation of nanostructured fully stabilized zirconia by pulsed electric current sintering. *Acta Mater.* **2010**, *58*, 5022–5030, doi:10.1016/j.actamat.2010.05.038.
234. Bakshi, S.R.; Musaramthota, V.; Lahiri, D.; Singh, V.; Seal, S.; Agarwal, A. Spark plasma sintered tantalum carbide: Effect of pressure and nano-boron carbide addition on microstructure and mechanical properties. *Mater. Sci. Eng. A* **2011**, *528*, 1287–1295, doi:10.1016/j.msea.2010.10.009.
235. Kim, B.; Hiraga, K.; Grasso, S.; Morita, K.; Yoshida, H.; Zhang, H.; Sakka, Y. High-pressure spark plasma sintering of MgO-doped transparent alumina. **2012**, 116–118.
236. Grasso, S.; Hu, C.; Maizza, G.; Kim, B.-N.; Sakka, Y. Effects of Pressure Application Method on Transparency of Spark Plasma Sintered Alumina. *J. Am. Ceram. Soc.* **2011**, *1409*, 1405–1409, doi:10.1111/j.1551-2916.2010.04274.x.

237. Lu, T.C.; Chang, X.H.; Qi, J.Q.; Luo, X.J.; Wei, Q.M.; Zhu, S.; Sun, K.; Lian, J.; Wang, L.M.; Lu, T.C.; et al. Low-temperature high-pressure preparation of transparent nanocrystalline MgAl₂O₄ ceramics. *Appl. Phys. Lett.* **2006**, *88*, 1–3, doi:10.1063/1.2207571.
238. Perepezko, J.H.; Massalski, T.B. A NOTE ON THE NATURE OF MASSIVE TRANSFORMATION INTERFACES. *Scr. Metall.* **1972**, *6*, 743–752.
239. Meng, Y.; Xu, J.; Jin, Z.; Prakash, B.; Hu, Y. *A review of recent advances in tribology*; 2020; Vol. 8; ISBN 4054402003.
240. Rigney, D.A. Comments of metals on the sliding wear. *Tribol. Int.* **1997**, *30*, 361–367.
241. Hokkirigawa, K.; Kato, K. An experimental and theoretical investigation of ploughing, cutting and wedge formation during abrasive wear. *Tribol. Int.* **1988**, *21*, 51–57.
242. Kato, K. Abrasive wear of metals. *Tribol. Int.* **1997**, *30*, 333–338, doi:10.1016/S0301-679X(96)00063-1.
243. Yang, X.; Qiu, Z.; Wang, Y. Stress interaction and crack propagation behavior of glass ceramics under multi-scratches. *J. Non. Cryst. Solids* **2019**, *523*, 119600, doi:10.1016/j.jnoncrysol.2019.119600.
244. Li, C.; Zhang, F.; Meng, B.; Rao, X.; Zhou, Y. Research of material removal and deformation mechanism for single crystal GGG (Gd₃Ga₅O₁₂) based on varied-depth nanoscratch testing. *Mater. Des.* **2017**, *125*, 180–188, doi:10.1016/J.MATDES.2017.04.018.
245. Van Swygenhoven, H.; Derlet, P.M. Grain-boundary sliding in nanocrystalline fcc metals. *Phys. Rev. B - Condens. Matter Mater. Phys.* **2001**, *64*, 1–9, doi:10.1103/PhysRevB.64.224105.
246. Schiøtz, J.; Di Tolla, F.D.; Jacobsen, K.W. Softening of nanocrystalline metals at very small grain sizes. *Nature* **1998**, *391*, 561–563, doi:10.1038/35328.
247. Schiøtz, J.; Vegge, T.; Di Tolla, F.D.; Jacobsen, K.W. Atomic-scale simulations of the mechanical deformation of nanocrystalline metals. *Phys. Rev. B - Condens. Matter Mater. Phys.* **1999**, *60*, 11971–11983, doi:10.1103/PhysRevB.60.11971.

248. Shan, Z.; Stach, E.A.; Wiezorek, J.M.K.; Knapp, J.A.; Follstaedt, D.M.; Mao, S.X. Grain boundary-mediated plasticity in nanocrystalline nickel. *Science* (80-.). **2004**, *305*, 654–657, doi:10.1126/science.1098741.
249. Ke, M.; Hackney, S.A.; Milligan, W.W.; Aifantis, E.C. Observation and measurement of grain rotation and plastic strain in nanostructured metal thin films. *Nanostructured Mater.* **1995**, *5*, 689–697, doi:10.1016/0965-9773(95)00281-I.
250. Wang, L.; Teng, J.; Liu, P.; Hirata, A.; Ma, E.; Zhang, Z.; Chen, M.; Han, X. Grain rotation mediated by grain boundary dislocations in nanocrystalline platinum. *Nat. Commun.* **2014**, *5*, 1–7, doi:10.1038/ncomms5402.
251. Farkas, D.; Frøseth, A.; Van Swygenhoven, H. Grain boundary migration during room temperature deformation of nanocrystalline Ni. *Scr. Mater.* **2006**, *55*, 695–698, doi:10.1016/j.scriptamat.2006.06.032.
252. Kim, S.S.; Kato, K.; Hokkirigawa, K.; Abé, H. Wear mechanism of ceramic materials in dry rolling friction. *J. Tribol.* **1986**, *108*, 522–526, doi:10.1115/1.3261255.
253. Wang, Y.S.; Hsu, S.M.; Munro, R.G. Ceramics wear maps: alumina. *Lubr. Eng.* **1991**, *47*, 63–69.
254. Trabelsi, R.; Treheux, D.; Orange, G.; Fantozzi, G.; Homerin, P.; Thevenot, F. Relationship between mechanical properties and wear resistance of alumina-zirconia ceramic composites. *Tribol. Trans.* **1989**, *32*, 77–84, doi:10.1080/10402008908981865.